

## **INFORMATION TO USERS**

**This material was produced from a microfilm copy of the original document. While the most advanced technological means to photograph and reproduce this document have been used, the quality is heavily dependent upon the quality of the original submitted.**

**The following explanation of techniques is provided to help you understand markings or patterns which may appear on this reproduction.**

- 1. The sign or "target" for pages apparently lacking from the document photographed is "Missing Page(s)". If it was possible to obtain the missing page(s) or section, they are spliced into the film along with adjacent pages. This may have necessitated cutting thru an image and duplicating adjacent pages to insure you complete continuity.**
- 2. When an image on the film is obliterated with a large round black mark, it is an indication that the photographer suspected that the copy may have moved during exposure and thus cause a blurred image. You will find a good image of the page in the adjacent frame.**
- 3. When a map, drawing or chart, etc., was part of the material being photographed the photographer followed a definite method in "sectioning" the material. It is customary to begin photoing at the upper left hand corner of a large sheet and to continue photoing from left to right in equal sections with a small overlap. If necessary, sectioning is continued again — beginning below the first row and continuing on until complete.**
- 4. The majority of users indicate that the textual content is of greatest value, however, a somewhat higher quality reproduction could be made from "photographs" if essential to the understanding of the dissertation. Silver prints of "photographs" may be ordered at additional charge by writing the Order Department, giving the catalog number, title, author and specific pages you wish reproduced.**
- 5. PLEASE NOTE: Some pages may have indistinct print. Filmed as received.**

**Xerox University Microfilms**

300 North Zeeb Road  
Ann Arbor, Michigan 48106

76-1874

SRINIVASAN, Satyamangalam R., 1947-  
INITIAL OXIDATION AND SELF-DIFFUSION PHENOMENA  
ON METAL SURFACES.

Iowa State University, Ph.D., 1975  
Engineering, materials science

**Xerox University Microfilms**, Ann Arbor, Michigan 48106

THIS DISSERTATION HAS BEEN MICROFILMED EXACTLY AS RECEIVED.

**Initial oxidation and self-diffusion phenomena on metal surfaces**

**by**

**Satyamangalam R. Srinivasan**

**A Dissertation Submitted to the  
Graduate Faculty in Partial Fulfillment of  
The Requirements for the Degree of  
DOCTOR OF PHILOSOPHY**

**Department: Metallurgy  
Major: Metallurgy (Physical Metallurgy)**

**Approved:**

Signature was redacted for privacy.

**In Charge of Major Work**

Signature was redacted for privacy.

**For the Major Department**

Signature was redacted for privacy.

**For the Graduate College**

**Iowa State University  
Ames, Iowa**

**1975**

## TABLE OF CONTENTS

	<u>Page</u>
INTRODUCTION	1
INCIPIENT OXIDE FORMATION OF VANADIUM SURFACE	5
LEED Technique	5
Introduction	5
Diffraction principles	6
Nomenclature	9
Literature Review	15
LEED studies on the oxygen adsorption on vanadium	16
Oxygen adsorption studies on other B.C.C. metals	19
Nucleation and growth of initial oxide	25
Reconstruction of surface atoms	29
Experimental Procedure	31
LEED apparatus	31
Maintenance of LEED optics	36
Specimen preparation	39
Specimen mounting, heating and cleaning	40
Laser simulation	42
Results and Discussion	44
LEED pattern from V(100) surface	44
LEED patterns from V(100) surface in oxygen environment	47
Analysis of the diffraction pattern	49
Discussion	53

	<u>Page</u>
Recommendations for future investigations	58
SELF-DIFFUSION PHENOMENA ON METAL SURFACES	59
Introduction	59
Grain Boundary Groove Model	62
Earlier Theories on the Growth of Grain Boundary Grooves	69
Evaporation-condensation mechanism	69
Surface diffusion mechanism	73
Volume diffusion mechanisms	76
Combined transport mechanisms	78
Theory of Grain Boundary Grooving Under Simultaneous Action of Various Transport Mechanisms	82
Need for the present analysis	82
Theoretical model	88
Solution of differential equations	91
Numerical calculations	95
Discussion	97
Predictions of the present theory	98
Extension of the present analysis	106
Analysis of experimental data	108
CONCLUSIONS	118
REFERENCES	119

	Page
ACKNOWLEDGMENTS	122
APPENDIX	123
Evaluation of the Integral	
$I = \frac{2}{\pi} \int_0^{\infty} \frac{1}{k^2} [\exp(-k^4) - 1] \cos ku \, dk$	123
Evaluation of integral $I_1$	123
Evaluation of integral $A_2$	124
Evaluation of integral $A_3$	124

## INTRODUCTION

Oxidation is one of the problems most commonly encountered by the metallurgists. On the macroscopic scale oxidation causes deterioration of most metals, whereas on the microscopic scale a few angstroms thick oxide layers on metals cause problems in the techniques of epitaxial growth, thin film deposition, bonding of composites, etc. Most of the oxidation studies so far have concentrated on the measurements of macroscopic oxide thickness with time. However, a knowledge of the detailed mechanism of the chemical reaction leading to oxidation during the very initial stages is essential in order to prevent the formation of initial oxide layer and thus oxidation (1). Such an understanding could be obtained by studies of the reaction kinetics of initial oxide formation, the epitaxial relationship between the oxide and the substrate metal, and the detailed structure and composition of the macroscopic oxide layers. Since the formation of the thin incipient oxide layer may be related to that of the chemisorbed oxygen, a complete description of the oxidation of a metal must also include an investigation of the adsorption of oxygen on metal surfaces.

The present work is therefore concerned with the initial oxidation and self-diffusion phenomena on vanadium surfaces. Vanadium has been chosen because of its importance as a high temperature material. In general, the Group V metals, like Ta, Nb and V are potential high temperature materials. However their poor oxidation resistance poses a major problem which severely limits their application in oxidizing environments

at elevated temperatures. In this high temperature oxidation process, surface reactions play an important part and often control the rate of oxidation process. This can be seen from the fact that the oxygen flux impinging on the surface decreases with increasing temperature at fixed oxygen pressure ( $\text{flux} \propto T^{-1/2}$ ), whereas the rates of diffusion and chemical reactions increase exponentially with temperature.

For the precise understanding of the initial oxidation phenomena, studies of oxygen interaction with vanadium surfaces are needed. Such studies of the interaction of gaseous molecules with metal surfaces have become possible in the last decade due to the development of ultrahigh vacuum systems and the low energy electron diffraction (LEED) technique. Earlier LEED studies show that adsorbed oxygen atoms on the surfaces of refractory metals form various ordered arrangements which are characteristic of the orientation of the surface, temperature of the surface, and the oxygen pressure in the system. Vijai and Packman (2) found that at temperatures less than 900°C a (1x1) pattern (a pattern which represents a monolayer coverage) was present whereas at temperatures above 1100°C this structure of oxygen adsorbed surface transformed to a (2x2) pattern (a pattern which corresponds to a unit mesh in which the adsorption sites are situated on one corner of each of the substrate unit mesh). Similar adsorption patterns have also been observed in molybdenum and tungsten. However, in molybdenum, Hayek and Farnsworth (3) also observed several modes of adsorption which were intermediate between the (1x1) and the (2x2) structures.

In order to understand the interaction of oxygen with the refractory



metal surfaces, the low energy electron diffraction technique is used in the present work to determine ordered surface configurations that are exhibited by the adsorbed oxygen on the vanadium (100) surface. It is found that in the temperature range 900-1100°C and pressure range  $10^{-8}$ - $10^{-6}$  Torr, oxygen forms three distinct ordered arrangements on the surface which correspond to a monolayer, one-third monolayer, and a one-fourth monolayer coverage of oxygen on the surface. A detailed analysis of the diffraction patterns and the plausible atomic arrangement of surface atoms are discussed.

When a vanadium surface is exposed to oxygen environment at high temperatures for a prolonged period of time, macroscopic oxide formation can be seen on the surface. In order to quantitatively understand the kinetics of such oxide formation, a knowledge of the surface diffusion is required. Among the various methods of determining surface self diffusion coefficient of metals, the grain boundary grooving technique is most widely used. In this technique the growth of grooves, developed at grain boundaries, due to matter transport by the diffusional mechanisms is studied and the data on groove widths are analyzed to obtain surface self diffusion coefficients. However, in recent years, the interpretation of grain boundary groove data has been subjected to serious controversial views (4-6) due to the uncertainty in isolating the matter transport due to the surface diffusion mechanism only. This has necessitated the development of a rigorous theory of grain boundary grooving under the simultaneous action of surface and volume diffusion mechanisms. In this thesis such a theory is developed and a method of analyzing the groove

data is outlined which enables the simultaneous determination of both the surface as well as volume diffusion coefficients. The theory is then applied to the experimental data of Gjostein (7) on a copper (100) surface.

## INCIPIENT OXIDE FORMATION OF VANADIUM SURFACE

## LEED Technique

Introduction

It is well known that the periodic arrangement of atoms inside a crystal can scatter electromagnetic waves such as X-rays and produce diffraction patterns which can be analyzed to understand the atomic arrangement inside the crystal. In the same way, the phenomenon of diffraction can also be utilized to understand the periodic atomic arrangement on the surface of a crystal. To obtain diffraction from a crystal surface incident waves of wavelength shorter than the spacing between the most widely separated rows of atoms on the surface must be used. Also the waves should not penetrate deep inside the crystal, so that the diffraction pattern would be characteristic of the surface atomic arrangements only. The first requirement is met by several kinds of waves such as the electromagnetic waves like X-rays and the matter waves of electrons and neutrons. However, only the electron waves are the ones which meet both the requirements. X-rays penetrate many thousand layers of atoms and neutron rays penetrate even deeper. The ideal probe is a beam of slow electrons since its penetrating power can be adjusted by altering the energy, thereby allowing it to penetrate only the topmost atomic layer of a crystal.

The wave nature of electrons had been postulated by DeBroglie as early as 1924, and the actual experimental proof that the electrons do behave as waves and can be diffracted by atoms in a crystal was first shown

by C. J. Davisson and L. H. Germer of Bell Telephone Laboratories, and independently in Britain by Sir George Thompson in 1927. The electrons used by Thompson had energies of around 50 KeV and hence could penetrate about 100 atom layers. On the other hand the energy range of the electrons used by Davisson and Germer was between 5 and 550 eV so that these electrons could penetrate only the outer layers of the crystal and this gave a diffraction pattern which is characteristic of the surface structure. Since the experiments of Davisson and Germer, several developments have been made to obtain a well-focussed beam of monoenergetic electrons and to detect their diffracted components. With the advent of ultra high vacuum techniques and electronic instrumentation, commercial equipments are available today which can be used to perform the LEED experiments without too much difficulty.

### Diffraction principles

The probe in the LEED experiment is a collimated beam of monoenergetic electrons of low energy (1-500 eV) which is diffracted from the crystal surface being studied. This is different from X-ray diffraction in which the high energy electromagnetic waves (50 keV) penetrate the sample to a few millimeter depth and scan the three dimensional periodicity of the specimen. In contrast to the three dimensional case which gives rise to Bragg peaks, the intensity of the backscattered electrons (in the case of strictly two-dimensional diffraction) would be continuous and decrease monotonically with increasing electron energy. The LEED, being intermediate between the above, gives rise to a continuous spectrum with peaks some of which occur at Bragg angles. The peaks which do not correspond to Bragg angles are due

to multiple scattering which arises because of the large scattering cross section for low energy electrons.

As in the case of X-ray diffraction, the wave numbers,  $K^0$  and  $K'$ , of the incident and the diffracted electron beams in LEED obey the relationship

$$\vec{K}'_{||} = \vec{K}^0_{||} + \vec{G}_{||} \quad (1a)$$

where  $||$  sign indicates the components parallel to the surface and  $\vec{G}$  represents the reciprocal lattice vector. A similar relation between the perpendicular components will not be applicable for LEED because of the lack of periodicity in the perpendicular direction. However, the perpendicular components of the electron beams will be constrained by the elastic nature of diffraction. For elastic scattering, the incident and diffracted wave vectors have to satisfy the relationship

$$|\vec{K}'|^2 = |\vec{K}'_{||}|^2 + |\vec{K}'_{\perp}|^2 = |\vec{K}^0|^2 \quad (1b)$$

Thus, the constraint on the perpendicular components of the electron wave vectors can be obtained by eliminating  $\vec{K}'_{||}$  between Equations 1a and 1b, which gives

$$\vec{K}'_{\perp} = \pm \hat{z} (|\vec{K}^0|^2 - |\vec{G}_{||}|^2 - |\vec{K}^0_{||}|^2)^{1/2} \quad (1c)$$

The implications of the above diffraction conditions can be understood in terms of experimental parameters as follows. The magnitude of  $\vec{K}^0$  which is the deBroglie's wavelength of the incident electrons is dependent only

on the electron energy used in the diffraction experiment. The magnitudes of all the diffracted wave vectors are in turn dependent only on the electron energy as implied by Equation 1b. However, as seen from Equation 1a, the parallel component of the diffracted beam can differ from that of the incident beam by some reciprocal lattice vector. As for the perpendicular components of the diffracted beams, Equation 1c predicts wave vectors along both positive and negative  $\hat{z}$  directions and it also predicts real and imaginary components for the diffracted beam. Also the diffracted beams whose perpendicular components lie along the  $+\hat{z}$  direction will not be observed in the diffraction pattern since they do not contribute to backward diffraction.

At very low diffraction voltages and hence at very low magnitudes of  $\vec{k}^0$  vectors, the perpendicular components of diffracted beams would be imaginary, as can be seen from Equation 1c, except for the specularly diffracted beam for which the corresponding reciprocal vector is the null vector. Therefore at such low voltages, one can observe only the specular spot. However, as the diffraction voltage is increased, a stage would be reached when the magnitude of the incident wave vector becomes large enough to accommodate the smallest reciprocal lattice vector to give rise to diffraction beams with real perpendicular components. Thus, one observes the first order diffraction spots. Upon further increase in diffraction voltage, diffraction spots of different orders would appear at appropriate voltages.

These diffraction conditions given by Equations 1a, 1b and 1c are applicable for any two dimensional diffraction. For the case of LEED, there

are **additional** diffraction conditions which arise due to multiplicity of scattering. These are diffraction conditions, of the form of Equation 1a, between any two diffraction beams rather than between the incident beam and a diffracted beam. These conditions for multiple scattering can be written mathematically as follows:

$$\vec{k}_{||}'' = \vec{k}_{||}' + \vec{G}_{||} \quad (2a)$$

$$\vec{k}_{||}'' = \vec{k}_{||}' + \vec{G}_{\perp} \quad (2b)$$

The diffraction conditions discussed in this section should give the periodic nature of the surface lattice. However, a knowledge of the intensities of diffracted beams is required to uniquely interpret the type of scattering centers on the surface. Theoretical calculations so far have been able to predict the intensity of a given spot as a function of incident electron energy for a given periodic arrangement of atoms on the surface. However, no unique interpretation is yet possible to obtain precise atomic arrangements on the surface from the analysis of the experimental data on spot intensity.

#### Nomenclature

As mentioned above, the LEED intensities are not able to predict a unique atomic arrangement on the surface. Therefore the interpretation of LEED patterns is done mainly with the help of the observed symmetry of the pattern. Such interpretations do give, although not unambiguously, an

understanding of the surface structure. A classification of surface structures can be made by using symmetry properties of the two dimensional surface lattice. However, most surface studies require knowledge of surface atomic arrangement with respect to that of the substrate, a substrate structure being defined as the one which corresponds to an equivalent parallel plane in the bulk. Thus, indexing of patterns is done to give the relationship between the unit cells of the surface and the substrate atomic arrangements. Such a convention is given by Wood (8), and it will now be discussed with reference to Figure 1 which shows some simple diffraction patterns obtained from low index surfaces of F.C.C. metals.

A basic pattern is a (1x1) pattern which corresponds to a unit mesh of surface structure consisting of diffraction centers only at the corners of the unit mesh. The diffraction pattern corresponding to the (100) surface of a clean nonreconstructed surface of a F.C.C. metal would be an example of this pattern. It is shown in Figure 1a along with the real space lattice which gives rise to this pattern. Such a pattern is obtained for monolayer coverage in which adsorbing atoms occupy surface sites such that the vectors which define the unit cell of the adsorbed surface are identical to the vectors which define the unit cell of the substrate.

In general, a diffraction pattern is denoted by (mxn) pattern in which the two indices m and n indicate the order of spots in the two directions which are not crystallographically equivalent. Figure 1b shows a (2x1) pattern along with the corresponding real space lattice. It is seen that this pattern can be differentiated from the (1x1) pattern by the presence of extra spots appearing midway between the spots of the (1x1) pattern.



Figure 1. Diffraction pattern from low index F.C.C. surfaces. All figures are for (100) plane except Figure 1 (d) which is for (110) plane

- (a) (1x1) pattern
- (b) (2x1) pattern
- (c) (2x2) pattern
- (d) ( $\sqrt{3} \times \sqrt{3}$ ) - 30° pattern
- (e) C(2x2) pattern

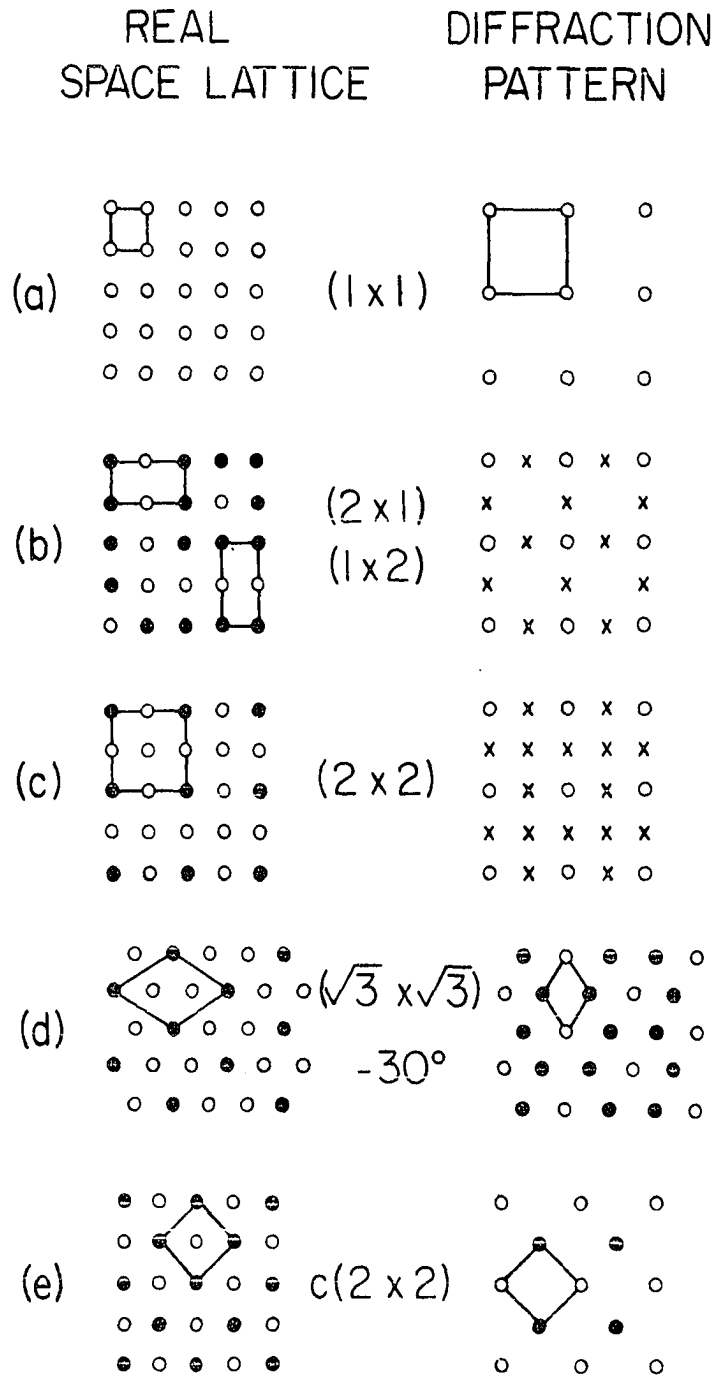


Figure 1. Diffraction pattern from low index F.C.C. surfaces. All figures are for (100) plane except Figure d which is for (110) plane  
 (a) (1x1) pattern; (b) (2x) pattern; (c)

These spots are referred to as the  $(\frac{1}{2}, 0)$  spots, where  $(\frac{1}{2}, 0)$  represents their position. Although these spots occur in two different directions (vertical and horizontal directions), the pattern should be characterized  $(2 \times 1)$  and not  $(2 \times 2)$  since these two directions are crystallographically equivalent. The origin of the  $\frac{1}{2}$  order spots can be explained from the real space lattice. Because of crystallographic equivalence, the real space lattice consists of two domains each at  $90^\circ$  to the other, as is shown in Figure 1b, and each of these domains contribute to extra spots in one of the two perpendicular directions. Hence a pattern consisting of extra spots in two perpendicular directions results. For the sake of clarity a  $(2 \times 2)$  pattern is given in Figure 1c. It is seen that the  $(2 \times 2)$  pattern consists of  $(\frac{1}{2}, \frac{1}{2})$  spots in addition to  $(\frac{1}{2}, 0)$  spots.

Figure 1d represents a  $(\sqrt{3} \times \sqrt{3})$  pattern in which the unit cell is rotated at  $30^\circ$  to the unit cell of the  $(1 \times 1)$  pattern. In such cases the rotation of unit cell is also indicated and the pattern is indexed as  $(\sqrt{3} \times \sqrt{3}) - 30^\circ$ .

In addition to the regular  $(m \times n)$  notation, the symbols P, C are sometimes indicated before  $(m \times n)$  to denote if the unit cell is primitive or centered. Thus the pattern in Figure 1e is indexed  $C(2 \times 2)$  where C indicates that it is a centered structure. Correspondingly the pattern of Figure 1c can be indexed as  $P(2 \times 2)$ , although the subscript P is often omitted.

When adsorbed atoms form a simple ordered structure, the  $(m \times n)$  notation can be used easily to represent the ordered arrangement. However, many adsorbed atoms arrange themselves in quite a complex ordered

arrangement that simple (mxn) representation is no longer possible. In these cases a matrix notation is employed.

The matrix notation is based on the fact that the LEED pattern represents the reciprocal of the surface structure. Thus to arrive at the surface structure, matrices which generate the diffraction pattern are first constructed and the inversion of these then give the matrices which correspond to the surface arrangement of atoms. For example, the C(2x2) pattern shown in Figure 1e can be generated by two vectors  $A^*$  and  $B^*$  where

$$A^* = \left( \frac{1}{\sqrt{2}} i + \frac{1}{\sqrt{2}} j \right)$$

and

$$B^* = \left( -\frac{1}{\sqrt{2}} i + \frac{1}{\sqrt{2}} j \right).$$

These two vectors can be represented as the matrix

$$\begin{array}{cc} \frac{1}{\sqrt{2}} & \frac{1}{\sqrt{2}} \\ -\frac{1}{\sqrt{2}} & \frac{1}{\sqrt{2}} \end{array}$$

The inversion of this matrix is

$$\begin{array}{cc} \frac{1}{\sqrt{2}} & -\frac{1}{\sqrt{2}} \\ \frac{1}{\sqrt{2}} & \frac{1}{\sqrt{2}} \end{array}$$

and it is seen that this matrix represents a real space lattice which can be constructed by the vectors A and B, where

$$A = \left( \frac{1}{\sqrt{2}} i - \frac{1}{\sqrt{2}} j \right)$$

and

$$B = \left( \frac{1}{\sqrt{2}} i + \frac{1}{\sqrt{2}} j \right).$$

These vectors can be shown to generate the real space lattice as shown in Figure 1e. In the above example, only one matrix is needed to describe the entire pattern. In many complex patterns, one may require two or more matrices to describe the entire pattern.

The adsorption patterns are dependent on the pressure of the gaseous environment. The exposure is usually denoted in units of "langmuir", which corresponds to  $1 \times 10^{-6}$  Torr-sec. This amount of exposure would approximately cause a monolayer coverage because the average number of gas molecules striking a unit area of the surface is about equal to the average number of atoms per unit surface area.

Assuming the surface to be a square mesh of  $3 \text{ \AA}$  size, the average number of atoms per unit area of surface is about  $10^{15}$ . Therefore, if the sticking coefficient is unity, a monolayer coverage can be caused by  $10^{15}$  gas atoms striking a unit area of surface for one sec. The partial pressure of gas required for such a flux can be calculated from the kinetic theory of gases which relates the flux of gas molecules, J, to the partial pressure, p, of gas by the expression

$$J = p/(2\pi mkT)^{\frac{1}{2}} \quad (3)$$

where

$m$  = weight of gas molecules

$k$  = Boltzmann constant

$T$  = absolute temperature.

For a typical gas like  $O_2$  whose molecular weight is 32 the above expression shows that, at a temperature of 1000°K and  $J = 10^{15}$  atoms/cm<sup>2</sup>sec., the partial pressure of oxygen is obtained as  $10^{-6}$  torr., or one Langmuir. Thus it is seen that an exposure of 1L will cause approximately a monolayer coverage when sticking coefficient is unity.

#### Literature Review

Since its development, the Low Energy Electron Diffraction technique has been widely used to investigate surface structures of metals and oxides. The investigations involved mainly the study of clean metal surfaces and the chemisorption of submonolayer amounts of adsorbate on these surfaces. One of the earliest studies was reported by L. H. Germer, R. M. Stern and A. U. MacRae (9) who observed the formation of NiO tetrahedra during the oxidation of Ni(111) surfaces. Among the class of body centered cubic metals (of which vanadium is a member) Cr, Mo, W, Ta and Nb have been studied to a considerable extent.

In this thesis the term "initial oxidation" will be used to include all reactions of oxygen with a pure metal. In general, these reactions comprise of (a) ordered adsorption patterns on the surface, (b) the formation of pseudo-oxides which are metastable and (c) the formation of stable

oxides. We shall review the oxidation work in three parts. First, adsorption studies on V will be discussed. Next these results will be compared with the results on other B.C.C. metals, and finally, observations regarding the nucleation and growth of microscopic oxide will be reviewed.

#### LEED studies on the oxygen adsorption on vanadium

Figure 2 shows the V-O phase diagram (10). It is seen that several oxides of V namely,  $V_4O$ ,  $V_2O$ , and VO are present in the V rich side of the phase diagram. In addition to the above oxides (oxygen < 50 a/o), several other oxides have been reported in the literature (11). Table 1 summarizes the various oxides of V along with their crystallographic data. The LEED studies carried out so far on V have been concerned with two main aspects: (1) studies on pure vanadium in which oxygen adsorption on clean (100) and (110) surfaces was investigated, and (2) studies on  $V_2O_5$  oxide in which oxygen loss at the (100) surface was investigated and it was found that  $V_2O_5$  reduced to  $V_{12}O_{26}$ . The formation of the several other oxides reported in literature have not been studied by LEED.

Vijai and Packman (2) studied the adsorption of oxygen on the V(100) surface. They observed two kinds of ordered arrangements for oxygen on the above surface. The first kind was a monolayer arrangement producing a (1x1) pattern (Figure 1a). This pattern, on heating, transformed into another structure in which oxygen atoms occupied 1/4 of the lattice sites (producing a (2x2) pattern, Figure 1c). Oxygen adsorption on the (110) plane of V was studied by Haas, Jackson and Hooker (12) who observed an ordered arrangement giving rise to a (1x1) pattern. They noted that the

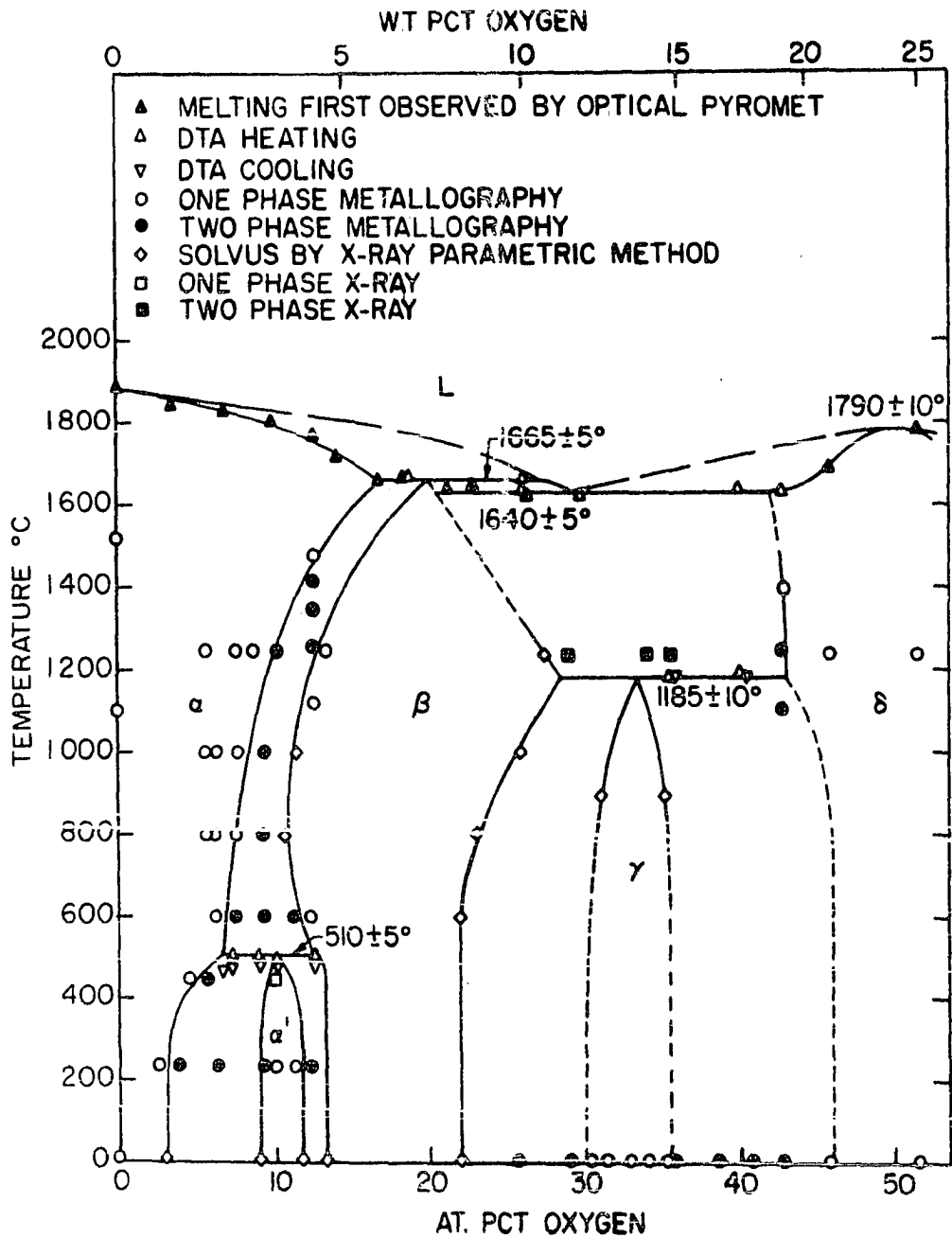


Figure 2. V-O phase diagram



Table 1. Crystallographic data on the oxides of vanadium

Oxide	$\frac{O}{V}$ ratio	Crystal System	lattice parameters			angles (in degree)		
			a	b	c			
$V_4O$	0.2	tetragonal	2.9		3.5			
$V_2O$	0.33	monoclinic	14.7	14.6	17.9	90.4		
$VO$	0.5	cubic	4.1					
$VO_{1.27}$	0.56	tetragonal	16.6		16.5			
$VO_{1.5}$	0.6	hexagonal	4.95		14.0			
$V_3O_5$	0.63	monoclinic	9.98	5.03	9.84	139		
$V_4O_7$	0.64	triclinic	5.5	7.0	12.9	96	95	109
$V_5O_9$	0.64	triclinic	5.47	6.99	8.72	97.5	112.4	109
$V_6O_{11}$	0.65	triclinic	5.44	6.99	23.66	98.5	120.9	108.9
$V_7O_{18}$	0.65	triclinic	5.43	7.00	15.16	98.9	125.5	108.9
$V_8O_{15}$	0.655	triclinic	5.43	6.99	37.08	99	128.5	109
$VO_{2.}$ (>340K)	0.667	tetragonal	4.54		2.85			
$VO_2$	0.667	monoclinic	5.743	4.517	5.375	122.6		
$V_6O_{13}$	0.7	monoclinic	11.9	3.671	10.122	100.9		
$V_2O_5$	0.71	orthorhombic	11.51	3.563	4.369			

patterns consisting of  $1/3$  order spots observed in the case of Ta and Nb, and which were characterized by the matrices  $\begin{pmatrix} 2 & -1 \\ 1 & 1 \end{pmatrix}$  and  $\begin{pmatrix} -2 & -1 \\ -1 & 1 \end{pmatrix}$ , could also be obtained for V. The atomic arrangement corresponding to this pattern is shown in Figure 3b.

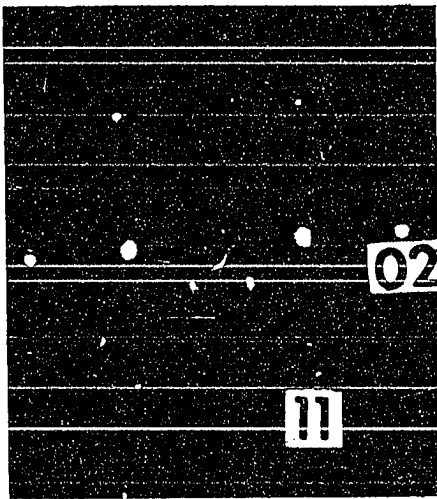
Fiermanns and Vennik (13) used the LEED technique to study a (100) surface cleaved from a single crystal of  $V_2O_5$  and obtained a rectangular pattern. The ratio of the sides of the rectangle corresponded to the ratio of the lattice parameters of the bulk which indicated that the surface atomic arrangement is an extension of the bulk. They observed that exposure at room temperature to oxygen, hydrogen, argon and  $CCl_4$  at pressures of  $10^{-6}$  torr did not change the pattern. The transformation  $V_2O_5 \rightarrow V_{12}O_{26}$ , due to oxygen loss, was indicated in the LEED pattern by the appearance of streaks followed by the disappearance of a parallelogram structure whose smaller unit mesh did not have a perfect coincidence with the rectangular pattern. The top layer of  $V_{12}O_{26}$  corresponds to the stretched  $V_2O_5$  top layer with slightly different dimensions and they could demonstrate that the parallelogram structure corresponded to the two dimensional unit mesh of the top layer of  $V_{12}O_{26}$ . They proposed that the appearance of streaks was due to the loss of oxygen from the V-O layer which disturbed the periodicity in the a-direction. After sufficient oxygen was lost,  $V_{12}O_{26}$  became the stable configuration and the diffusion from bulk restored the top layer oxygen concentration.

#### Oxygen adsorption studies on other B.C.C. metals

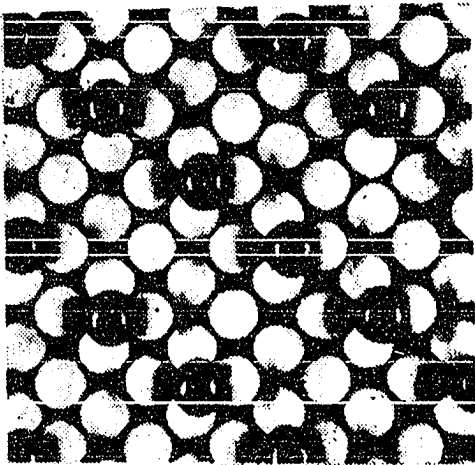
Since oxygen adsorption on V has been studied only to a limited extent, it is appropriate to review the work done on B.C.C. metals in general.

Figure 3. LEED patterns obtained by Haas, Jackson and Hooker

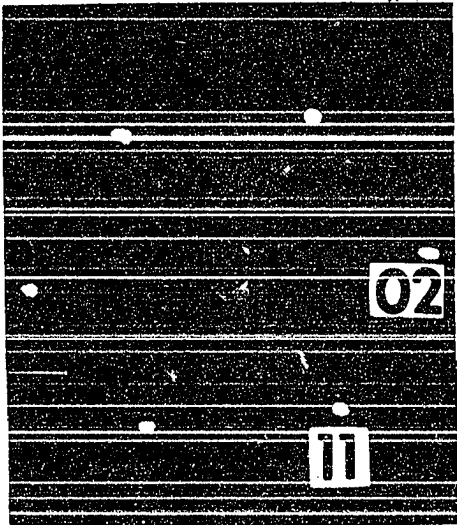
- (a) Pattern observed on (110) surfaces Ta, Nb and V
- (b) The proposed atomic structure corresponding to the above pattern
- (c) Pattern observed on (110) surfaces of Ta and Nb only
- (d) The proposed atomic structure corresponding to the above pattern



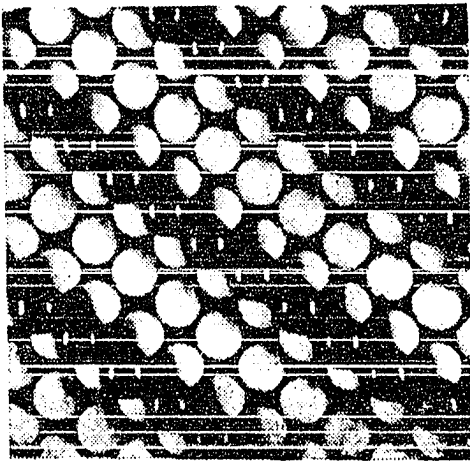
a.



b.



c.

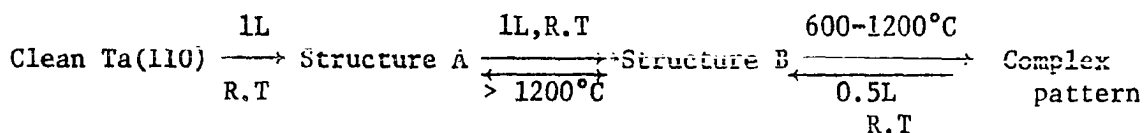


d.

Among the B.C.C. metals, W has been studied most extensively, though some studies on Mo, Ta and Nb have also been reported in the literature. Table 2 summarizes the LEED observations made on various B.C.C. metals. Work on Mo, Ta and Nb is reviewed below, because of their similarities with V.

Kann and Feuerstein (14) studied the interaction of oxygen with Mo (100) surfaces. In particular, they studied adsorption as a function of time while keeping reaction temperature and oxygen pressure constant at 750°C and  $1.6 \times 10^{-8}$  torr, respectively. They discovered various ordered arrangements corresponding to increasing oxygen coverages of 0.5, 0.67, 0.7, and 0.75, respectively. These were observed as C(2x2), (1x1), ( $\sqrt{5} \times \sqrt{5}$ ), P(2x2) patterns in the LEED. They could reverse the sequence by heating the crystal to increasingly higher temperatures, thereby removing oxygen from the surface by desorption or by diffusion into the bulk.

Oxygen adsorption and initial oxidation on Ta(110) surfaces has been studied by Haas, Jackson and Hooker (12) and by Roggio and Farnsworth (15), respectively. The observations of Haas, Jackson and Hooker (12) can be summarized as follows:



where R.T. stands for room temperature and L stands for langmuir.

Structure A was characterized by the matrices  $\begin{pmatrix} 2 & -1 \\ 1 & 1 \end{pmatrix}$  and  $\begin{pmatrix} -2 & -1 \\ -1 & 1 \end{pmatrix}$ ,

Table 2. LEED studies of oxygen adsorption on B.C.C. metals

Metal	Face	Surface Structures
W	(110)	(2x1), c(14x7), c(21x7), c(48x6) c(2x2), (2x2), (1x1)
	(111)	(211) facets
	(211)	(2x1), (4x3), (1x2) (1xn) n=1,2,3,4
	(100)	(4x1), (2x1)
Ta	(110)	(3x1), (3x2)R 18° 16'
	(112)	(3x1)
Nb	(110)	(3x1), (3x2)R 18° 16'
V	(100)	(1x1), (2x2)
	(110)	(3x1)
Mo	(110)	(2x2), (2x1), (1x1), c(2x2)
	(100)	Disordered c(2x2), (1x1), (1x1)R 26° 34' (2x2)

whereas Structure B was characterized by the matrices  $\begin{pmatrix} 2 & -1 \\ \frac{1}{2} & \frac{1}{2} \end{pmatrix}$  and  $\begin{pmatrix} -2 & -1 \\ -\frac{1}{2} & \frac{1}{2} \end{pmatrix}$ . The atomic arrangements corresponding to the above structures are given in Figures 3b and 3d, respectively. The complex pattern was presumed by Haas et al. to be the same structure as that designated Ta (110)5 by Boggio and Farnsworth (15) which is given in Figure 4. This Ta (110)5 structure was the starting point in the experiments of Boggio and Farnsworth (15) and they claimed that this structure was due to the presence of impurities on the surface.

Boggio and Farnsworth (15) reported that the growth of TaO on Ta obeys the epitaxial crystallographic relationships:

$$\begin{aligned} (111)_{\text{TaO}} &\parallel (110)_{\text{Ta}} \\ [11\bar{2}]_{\text{TaO}} &\parallel [\bar{1}10]_{\text{Ta}} \end{aligned}$$

This was evidenced by the fact that the TaO formed on Ta(110) surface at a room temperature exposure of  $1.8 \times 10^{-3}$  torr-minute produced the LEED pattern for a TaO(111) surface. The six fold symmetry of the LEED pattern indicated that the growth of TaO was in two orientations. By plotting oxygen exposure required for the incipient formation of oxide versus  $1/T$ , they estimated the formation energy for initial oxidation to be about  $0.24 \pm 0.04$  eV.

Oxygen adsorption on a Nb(110) surface was also studied by Haas, Jackson and Hooker (12) along with their study on Ta(110) surface. They observed identical patterns for both the surfaces. Based on their observations and those which had already been made on other B.C.C. metal surfaces they drew the following conclusions. The oxygen adsorption on Mo(110) and

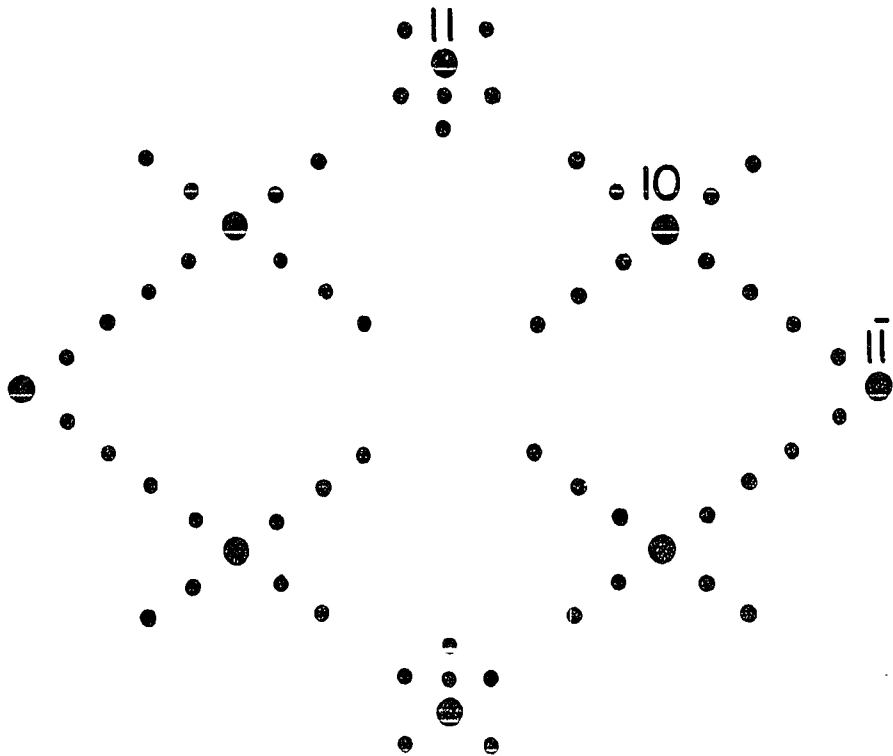


Figure 4. Ta(110)5 structure of Boggio and Farnsworth



W(110), which both belong to group VI(B) of the periodic chart, give rise to the same patterns. Similarly, Ta(110) and Nb(110) surfaces yield the same patterns, (which are different from those of Mo and W) and these metals both belong to group V(A). This suggests that the chemistry of the material, namely the covalent hybridized bond, is the factor that decides structures. The disparity among the atomic sizes of these metals seems to suggest that the size effect is not very pronounced.

#### Nucleation and growth of initial oxide

Many LEED observations of oxygen adsorption on metal surfaces have indicated that oxygen adsorption and oxide formation in the microscopic scale take place as isolated patches. Also epitaxial relationships between the metal substrate and oxide phase are normally observed.

An interesting work regarding initial oxidation on Ni(110) surface was reported by May and Germer (16). They found that the first adsorption pattern was characterized by an ordered arrangement (1x3) pattern, corresponding to  $1/3$  monolayer coverage at an exposure of 0.4 L. On further exposure at 300°C and at room temperature this pattern changed to (2x1) and (3x1) patterns, respectively. The transformation of (2x1) pattern to (3x1) pattern was reversible. The (3x1) pattern corresponded to  $1/2$  monolayer coverage. A half monolayer coverage, evidenced by the appearance of a C(2x2) pattern, was next observed at 0.8L and on further exposure the splitting of  $(k+1/2)$  apots occurred which subsequently gave rise to a (3x1) pattern at about 3L. This (3x1) pattern, which corresponded to a  $2/3$  monolayer coverage, did not change with further exposure to 5L. It was

found that the ratio,  $F$ , of the split distance to the unit mesh in the  $k$  direction obeyed the relation

$$F = \frac{0.5 R}{1 + 1.5 R} \quad (4)$$

where  $R$  is the relative number of the two sequences corresponding to the  $2/3$  and  $1/3$  monolayers.

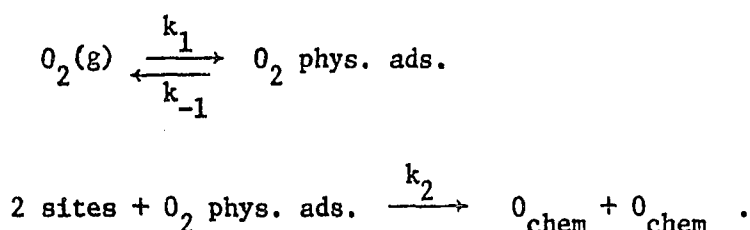
Further oxidation was characterized by the appearance at 10L of a new diffraction feature,  $P(9 \times 4)$ , which was very diffuse and corresponded to a new surface mesh. At an exposure of 20L the new spot features reached their maximum intensity and sharpness and the spots due to the  $2/3$  monolayer pattern were completely absent. They attributed the new features to the formation of a pseudo oxide which was formed by the reconstruction of the  $2/3$  monolayer and lay directly on the Ni substrate. Further exposure to 50L and a short heat treatment produced diffraction features due to NiO with its cube face parallel to the (110) Ni surface and with the [011] of NiO parallel to the [011] of Ni. No features due to the Ni substrate could be seen which indicated that the NiO was so thick that the metallic Ni was not contributing to diffraction.

Initial oxidation kinetics were studied on the most densely packed plane (110) and the more open (112) plane of W by Tracy and Blakely (17). They used the LEED technique in combination with work function measurements. Their observations on W(110) and W(112) planes indicated that, on both the surfaces, oxygen is first physically adsorbed in the precursor state as a molecule but then dissociates to monoatomic oxygen. Upon dissociation, the oxygen apparently migrates freely over the surface until it becomes

chemically adsorbed at the edges of growing islands of previously chemisorbed oxygen atoms.

Although Tracy and Blakely (17) found the basic mechanisms to be identical for both the surfaces W(110) and W(112), the controlling steps were found to be different for the two planes as indicated by their work function measurements. In their experiments the oxygen adsorption gave rise to a  $P(2 \times 1)$  pattern. In the case of adsorption on (112) plane the observed LEED intensities matched well with intensity distributions calculated for diffraction from an island model. Thus the above finding established an island growth model for the adsorption mechanism. In the case of (110) plane, although no quantitative calculation was made, the observation of sharp spots at very low coverage with no appreciable background indicated an island growth mechanism for this plane too. Because of the occurrence of island growth of chemisorbed oxygen, they could study the adsorption kinetics by measuring the work function of adsorbed surface as a function of exposure, the work function changes could be directly related to coverage. Their kinetic measurements demonstrated that the sticking probability was a constant value of 0.8 up to a 0.35 coverage in the case of (112) surface and was proportional to the square root of coverage up to a coverage of 0.2 in the case of (110). Based on an analysis by Orr of island growth, they concluded that, in the case of (110) plane, only those oxygen molecules which physisorb within a characteristic migration distance of an island eventually become chemisorbed. This is in contrast to the case of (112) plane where all of the physisorbed molecules become chemisorbed. Therefore chemisorption rate is impingement limited

on the (112) plane. They also provided indirect evidence, by measuring the intensity of half order spots as a function of exposure at various temperatures which gave a linear relationship with temperature independent slopes. This indicated that the sticking coefficient was independent of temperature for (112) plane as predicted by Orr's analysis. This conclusion can also be obtained from the analysis presented by Ehrlich (18). Ehrlich's model for the kinetics and mechanisms of chemisorption on metals assumes that impinging molecules are physisorbed on the metal surface initially and that chemisorption subsequently proceeds from a reservoir of the physisorbed molecules. The reactions can be represented as



By going through a rigorous calculation he showed that the linear oxidation rate, which has been found in Nb and Ta below the oxygen pressure of  $10^{-3}$  torr, can be given by

$$k = k_1 P_{\text{O}_2} \frac{k_2 (1-\theta)^2}{k_{-1} + k_2 (1-\theta)^2}$$

where  $\theta$  represents the fraction of chemisorption sites occupied by chemisorbed oxygen. Further elaborations of the theory led to the conclusion that a plot of  $\log(r)$  vs  $1/T$  should be a straight line where  $r$  is the sticking coefficient of the impinging molecules. This linear behavior has

been verified on Nb and Ta at high temperature (1200-1600°C) and low pressure ( $10^{-4}$  torr).

#### Reconstruction of surface atoms

During chemisorption the adsorbing atoms can, in certain cases, displace the adsorbent atoms. In such cases the adsorbent atoms will also be present on the top most layer and hence contribute significantly to diffraction. At the present state of knowledge regarding the intensities of LEED beams it is not possible to quantitatively predict spot intensities sufficiently accurately to distinguish whether reconstruction at the surface has taken place or not. However, qualitative arguments along these lines have been proposed to support reconstruction in several instances. For example among the B.C.C. metals reconstruction was proposed on the W(110) surface, by Germer and May (19), during oxygen adsorption. They suggested that the P(2x1) pattern which they observed was due to a W(110) plane in which alternate close packed rows of W were replaced by rows of oxygen. This proposition was put forward on the basis that the observed large intensity of the half order spots would not be possible otherwise due to the low scattering power of oxygen. However, this argument for surface reconstruction was refuted by Tracy and Blakely (17) who proposed that one oxygen atom per unit cell simply sits on top of the W surface in a site of maximum coordination with the substrate. Their arguments were based on calculations which showed that the W atoms cannot be transported to or from growing islands sufficiently rapidly by self-diffusion. Also the observation of Ptushinskii and Chuikov (20) that the flash desorption product of

a W(110) surface covered with less than half a monolayer of oxygen (presumably having islands of chemisorbed oxygen corresponding to the P(2x1) pattern) was oxygen and not tungsten oxide seems to support the view of Tracy and Blakely (17). Also it was observed that the desorption kinetics were first order for a surface on which oxygen had been adsorbed at high temperatures whereas second order kinetics prevail for a surface on which oxygen had been adsorbed at room temperature. The latter observation indicates that oxygen was adsorbed physically at room temperature and the oxide was very likely formed during the flash. This seems to undermine the arguments for reconstruction.

One can also approach the problem of reconstruction from basic bond energy calculations. If the bond energy of the substrate atoms is weak and the substrate-adsorbent bonds are strong, reconstruction would be favored and vice versa. Since W has a high melting point, and hence high bond energy, one would surmise reconstruction to be very unlikely. However, one would have to carry out complex calculations to determine the W-O bond energy (which is dependent on the site at which O atoms are adsorbed) in order to quantitatively decide whether or not reconstruction is a possibility. Also the mobility of substrate atoms on the exposed surfaces, about which very little is known, should bear significantly on the kinetics of reconstruction.

As seen from the above discussion of literature, most of the LEED observations of oxidation on B.C.C. metals have been carried out on the (110) surface which is the closest packed plane. It was mentioned that Haas, Jackson and Hooker (12) have observed a set of similar patterns on

the (110) surface of group V(A) metals, namely Ta, Nb and V and another set of similar patterns for group VI(B) metals namely Mo and W. From Table 3 which summarizes the observations on B.C.C. (100) planes, it is seen that Mo and V show certain similarities although many of the patterns observed for Mo are missing in V. This is in contrast to the results on (110) planes of Mo and V where oxygen adsorption gives similar patterns for both the metals. Therefore it would be desirable to undertake a study on V(100) surface to see if the missing patterns in V can be observed by varying the experimental parameters, and if not, to investigate the reasons for the difference in adsorption characteristics on (100) planes and not on (110) planes.

#### Experimental Procedure

##### LEED apparatus

The LEED system used in the present investigation was built by Perkin-Elmer and it consists of five main parts: (1) Ultra-high ( $10^{-10}$  Torr range) vacuum chamber 12" in diameter, (2) an electron gun to provide a well-focussed monoenergetic electron beam in the energy range 5-500 eV, (3) three-grid optics to monitor LEED patterns, (4) a specimen manipulator, which enables the specimen to be translated, rotated and tilted to some extent, and (5) an argon ion bombardment gun to remove contaminated surface layers. A schematic diagram of the LEED apparatus is shown in Figure 5.

The electron gun contains tungsten, in the form of a circular ring, is placed parallel to a disc shaped pusher grid and is coaxial to a cylindrical extractor grid. Since the filament is off-axial, the extractor

Table 3. LEED observations of oxygen adsorption on B.C.C. (100) planes

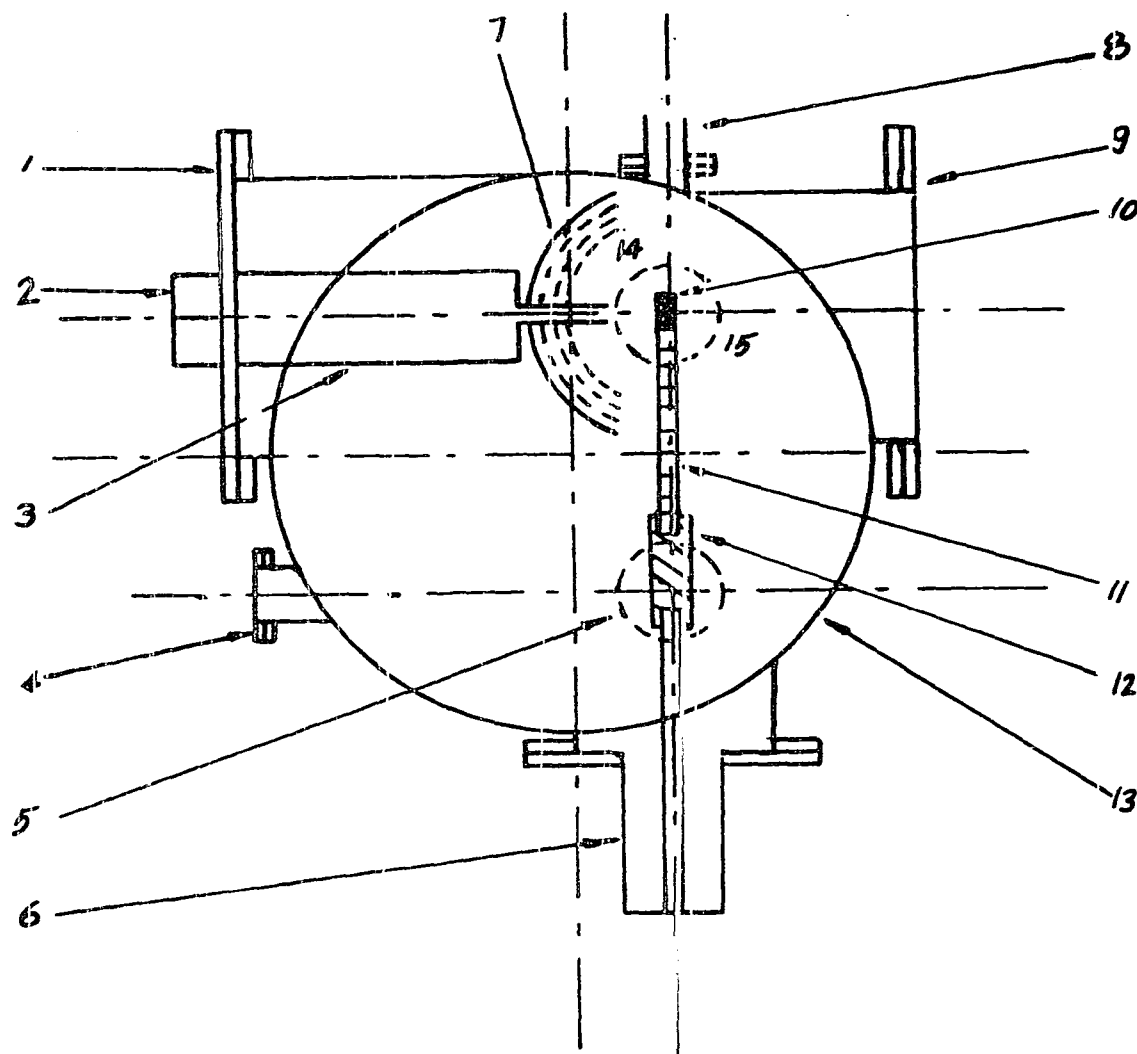
Coverage		0	0.25	0.33	0.5	-	0.6	0.75	1
Metal	$T/T_m$								
W		(1x1)	(4x1)		(2x1)				
Mo	0.35	(1x1)		1/3 order spots	C(2x2) 1.1L	(1x1) 2.3L	(5x5) 3.1L	P(2x2) 3.9L	(1x1) 5.5L
V	0.63	(1x1)						P(2x2)	(1x1) 300L
Cr	Room Temp.	(1x1)	(2x2) 3L						



grid brings the electrons to the center and these electrons are then accelerated towards the anode by the pusher grid.

In addition to the above two grids, the filament assembly also consists of a circular cathode shield which is kept concentric to both the filament and the pusher grid. The electron gun assembly incorporated accelerator anodes, decelerator anodes and focal lenses to obtain mono-energetic and well-focused beam of electrons. The electron optics is of the three grid type, and the diffraction patterns are displayed on a fluorescent screen. The "post acceleration technique" is employed to accelerate the elastic electrons which pass through the grid system towards the screen. The grids are hemispherical so that the undistorted reciprocal lattice could be seen when viewed from infinity.

The principle of the electron optics is as follows. The first grid is kept at ground potential, as is the specimen, so that the electrons travel a field-free path. The second grid is kept at a negative potential and the magnitude of this potential is the same as that of the incident electron energy. This grid repels most of the inelastic component of the backscattered electrons which have lost part of their energy in collision. The elastic component of the electrons which pass through the third grid (which is at ground potential) are accelerated towards the fluorescent screen by the application of a positive potential of 5000 V. When these electrons hit the screen, light is emitted due to radiative recombination after excitation by the electron beam. Thus, a diffraction pattern is displayed in which the light intensities of the spots are proportional to the number of electrons striking the screen per second.



- (1) LEED Optics
- (2) Connectors
- (3) Electron Gun
- (4) Feed Thru
- (5) Argon Gun
- (6) Specimen Manipulator
- (7) Fluorescent Screen
- (8) Mass Spectrometer
- (9) Viewing Window
- (10) Specimen
- (11) Specimen Holder
- (12) Ceramic Insulator
- (13) U.H.V. Chamber
- (14) Grids
- (15) Auger Gun

Figure 5. Schematic diagram of LEED apparatus

The diffraction chamber has a number of ports to provide electrical feedthroughs necessary for heating the specimen, argon ion bombardment for cleaning the specimen, specimen manipulator, etc. After a bakeout at 250°C for twelve hours, an ultrahigh vacuum of  $10^{-10}$  torr could be obtained in the chamber. The specimen manipulator shown in Figure 6 enables the specimens to be translated, rotated up to 350° and tilted by about 10°.

#### Maintenance of LEED optics

Burnt-out filaments in the electron gun were replaced by spot welding new ones to the filament holder in the filament assembly shown in Figure 7. Four tungsten filaments of 5 mil diameter are used in parallel at present. In order to prevent complete filament burn out, the minimum voltage required to give 2.5 A in each filament could be set on the regulated power supply.

The fluorescent screen is coated with phosphor, and the coating procedure is as follows. The fluorescent screen can be removed together with the three grids from the LEED optics assembly. The screen and the grids can then be separated. The grids can be cleaned by means of an ultrasonic cleaner with acetone as the fluid medium. Of the several methods of coating tried, the most successful procedure was as follows. The screen was spun slowly by mounting it on a motor and phosphor P-11 suspended in acetone was sprayed on to the screen by means of an atomizer operated at about 5 p.s.i. pressure. An inert gas-like argon was used to pressurize the atomizer which was kept at the center of curvature of the screen. The

- (1) Stainless steel bellow
- (2) Vacuum flange (1 I.D.)
- (3) Thermocouple Feedthrough (chromel-alumel)
- (4) Conductor feedthrough
- (5) Sample
- (6) Molybdenum foil
- (7) Ceramic insulator
- (8) Specimen holder
- (9) Ceramic insulator
- (10) Ta (50 mil) conductor
- (11) Filament (Thoriated Ir 10 mil)

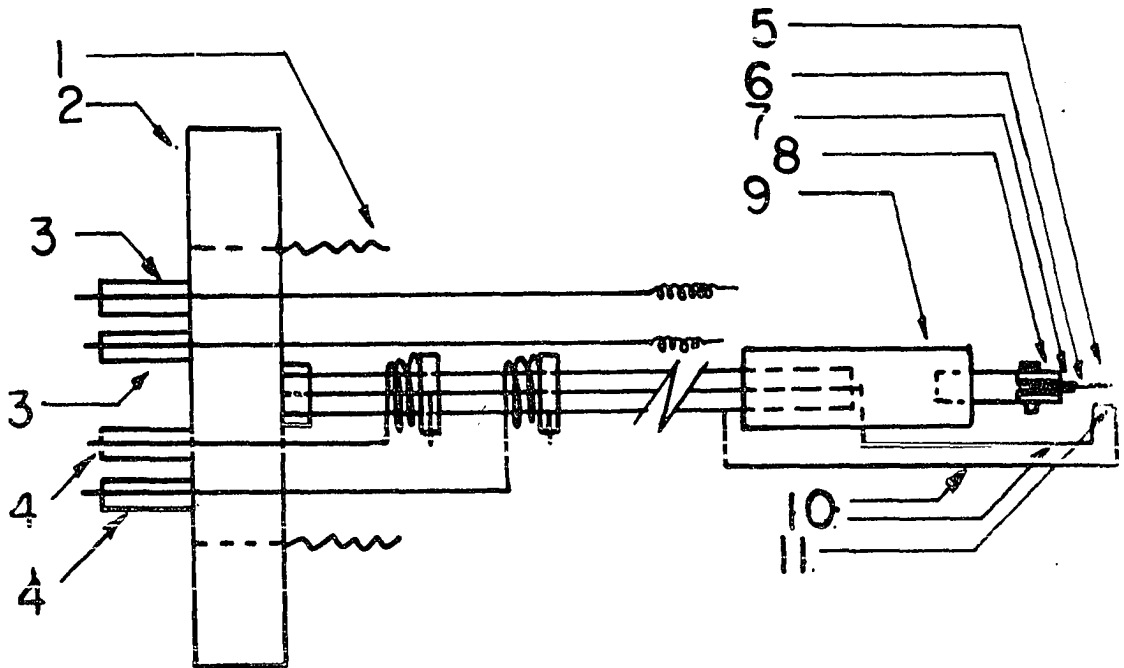
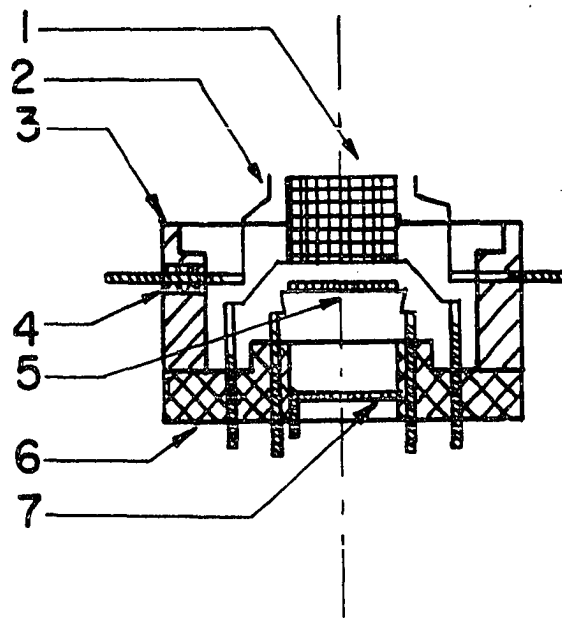


Figure 6. Modified specimen manipulator



- (1) Extractor grid (at 100V above cathode)
- (2) Filament holder (cathode)
- (3) Metallic mount
- (4) Ceramic insulator
- (5) Pusher Grid (at 0-200 V below cathode)
- (6) Ceramic disc
- (7) Cathode shield (at the same potential as the pusher grid)

Figure 7. Filament assembly

suspension was kept under agitation by means of a magnetic stirrer and a few drops of collodion added to the suspension to aid the flow. The phosphor concentration was adjusted to prevent the coating from being coarse.

#### Specimen preparation

Vanadium single crystal rods of high purity (99.98% V, 40 ppm oxygen) were obtained from F. A. Schmidt. Orientation of the single crystal was done by conventional Laue X-ray diffraction technique and (100) faces were cut. Etching the crystal with a solution of equal volumes of water and nitric acid was found to produce better Laue patterns due to the removal of the amorphous layer. Spark-cutting was employed to minimize damage to the surface, and specimens of about 6 mm. diameter and 0.75 mm. thickness were cut. Specimens of thinner cross-section, though preferable with regard to bulk impurity content, suffered a tendency to warp. The specimens were mounted in a cold mount, from which they could later be removed by dissolving the cold-mount resin in acetone. The mounted specimens were polished through 600 grit emery paper by means of a jig to avoid misorienting the face while grinding. A solution containing 25%  $\text{H}_2\text{SO}_4$  and 75% methyl alcohol was used to electropolish the crystals at 12 V (the voltage range was found to be narrow). The specimen orientations were rechecked to ensure that they were within  $1^\circ$  of the (100) plane. This was done by using a jig which was designed to hold the specimen face parallel to and at 3 cms. from the film in the Laue camera. The accuracy of this procedure was checked using a (100) cleavage plane of W bronze.

### Specimen mounting, heating and cleaning

The manipulator of the LEED system was modified to incorporate a chromel-alumel thermocouple feedthrough pair and electron bombardment heating. This heating procedure was preferred to the resistance heating due to the samples being rather thick. A new specimen holder was also designed for the same reason. Vanadium specimens which had been spot welded on to 10 mil tantalum foils were mounted in the holder. It has been reported (12) that no effects due to alloying would result.

Specimen heating was done by electron bombardment. Thoriated iridium filaments of 10 mil diameter were used as electron source. Iridium wires could be thoriated by electro-depositing thoria on the films from a suspension in ethyl alcohol (containing small quantities of thorium nitrate) at a potential of 100 volts relative to the graphite rod used as anode. The filaments were usually warmed after thoriating in order to improve the bond between the metal and the coating.

The samples were heated by applying a positive potential with respect to the filament. The filament current used was usually about 6 amperes, while the sample potential depended upon the desired specimen temperature. The crystal temperature was measured by a chromel-alumel thermocouple pair which was spot-welded on to the sample, calibrated against the power input to the crystal. Figure 8 shows a plot of the specimen temperature versus power input to the sample. It was found that the electron bombardment must be stopped momentarily while taking a temperature measurement. Otherwise the electron current striking the thermocouple leads interfered with the millivoltage measurement. The instrumentation shop designed an

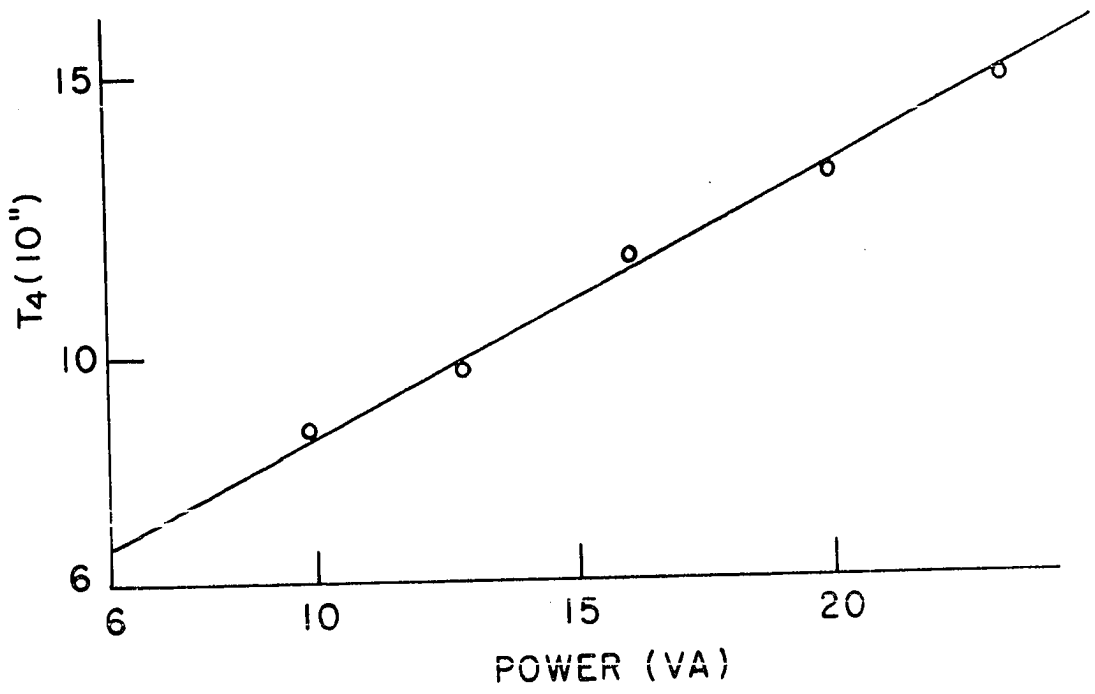


Figure 8. Temperature vs. power input calibration



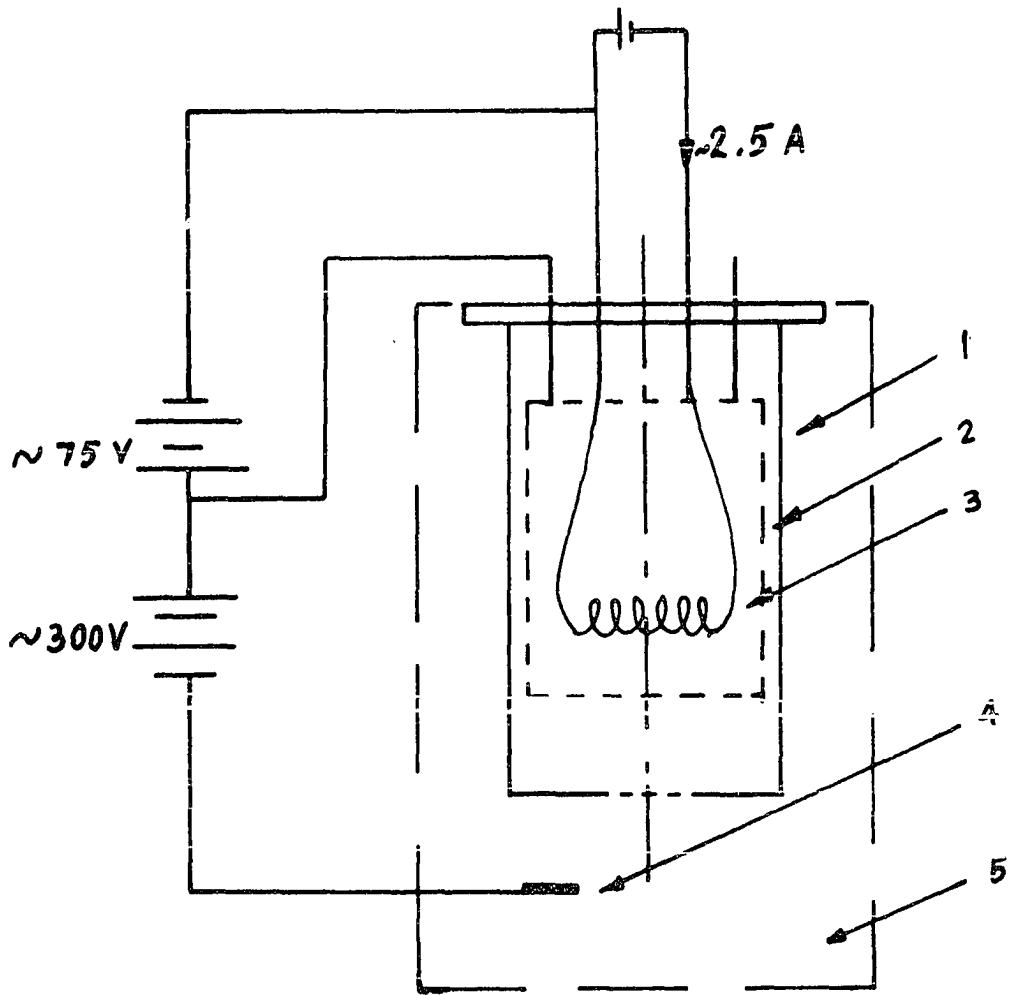
emission regulator to regulate the D.C. power supply in order to be able to heat the crystal at constant temperature.

The in situ cleaning of the crystal was done by alternate heating and argon bombardment. The argon ion gun was modified and improved. Argon ion currents of 10  $\mu\text{A}$  at a chamber pressure in the range of  $10^{-5}$  torr could be obtained by keeping the crystal at 300 V negative with respect to the grid of the argon ion gun. The electron emitter of the ion gun is a tungsten wire of 5 mil diameter and the filament current is about 2 amperes. Figure 9 shows the circuit for argon bombardment.

#### Laser simulation

The usefulness of low energy electrons, in the range 50-500 eV, in the study of surfaces arises because at very low electron energies the scattering cross sections of the atoms are very large. The incident beam does not penetrate very far since appreciable scattering in all directions occur. Unfortunately this leads to multiple scattering which makes the theoretical analysis of the diffraction pattern quite difficult. Thus, in order to interpret complex patterns, some simple method is warranted.

The laser simulation technique employed by Ellis and Campbell (21) was used for the interpretation of the diffraction patterns. Circles of different diameters were drawn on a 8"x8" size square to represent two types of scattering centers, namely the vanadium site and the oxygen adsorbed vanadium site. The patterns were reduced to 1/8" x 1/8" size so that at least 30 circles would lie within the laser beam whose diameter is about 1 mm. A He-Ne laser gun was used and the diffraction patterns



- (1) Shield
- (2) Grid
- (3) Filament (5 mil W)
- (4) Specimen
- (5) Vacuum chamber ( $10^{-5}$  torr A)

Figure 9. Modified argon ion gun

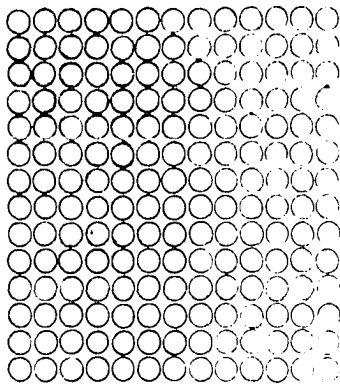
were photographed. Various adsorption patterns were simulated and then compared with the diffraction pattern obtained in the LEED. The atomic arrangement in a pure vanadium (100) is shown in Figure 10a and its laser diffraction pattern is shown in Figure 10b. The laser simulated diffraction pattern matches very well with the actual diffraction pattern obtained from the LEED as shown in the next section. The main problems with the laser simulation technique were the presence of background foggi-ness and interference of the incoherent components of the source which distorted the diffraction patterns slightly. However, the essential features of the LEED patterns are generally well reflected in these laser diffraction patterns.

## Results and Discussion

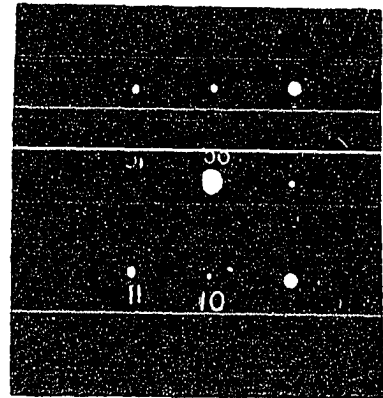
### LEED pattern from V(100) surface

A vanadium crystal with (100) orientation was mounted on the specimen holder in the LEED unit. The surface of the crystal was cleaned in situ by repeated heating and argon ion bombardment until a clear diffraction pattern which is characteristic of V(100) surface was obtained. The diffraction patterns were obtained at various voltages and the result obtained at 75 V is shown in Figure 11a. This voltage corresponds to the wavelength of electrons equal to  $1.4 \text{ \AA}$ . Use of still lower voltages, which increases the wavelength of the electron beam, resulted in second order spots going out of the screen.

The indexing of the first order spots observed in the LEED pattern is given in Figure 11b, which is a schematic representation of the LEED



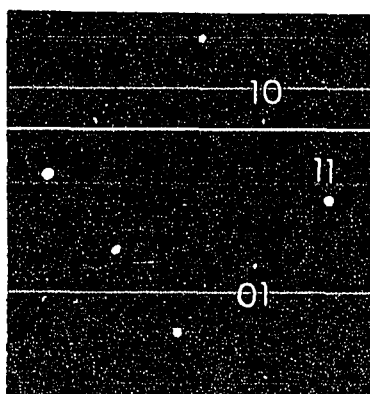
(a)



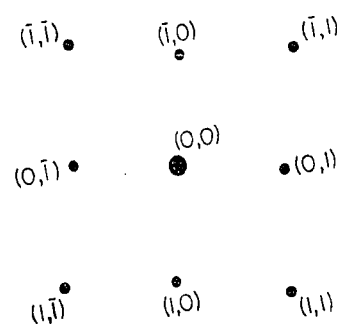
(b)

Figure 10a. Atomic arrangement of a clean V(100) surface

Figure 10b. Laser diffraction pattern of the above atomic arrangement



(a)



(b)

Figure 11a. LEED pattern of a clean V(100) surface

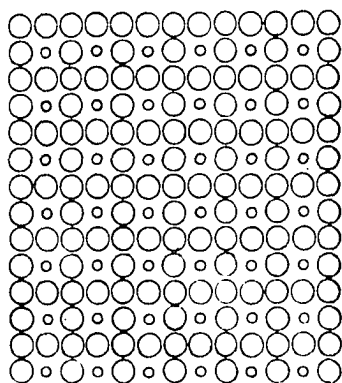
Figure 11b. Indexing of the first order spots observed in the pattern shown in Figure 11a

pattern. The two-dimensional atomic arrangement on the (100) surface of vanadium which corresponds to the diffraction pattern is shown in Figure 10a. The LEED pattern matches well with the simulated laser diffraction pattern shown in Figure 10a.

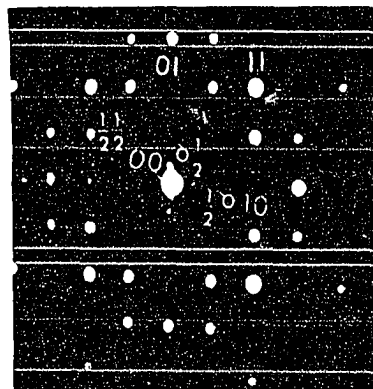
#### LEED patterns from V(100) surface in oxygen environment

Oxygen is now introduced directly into the system through leak valves and mass spectrographs were taken to analyze and check the ambient gases in the system. The specimen was heated to about 900°C and exposed for about 30 seconds at this temperature to oxygen pressure of  $10^{-8}$  torr. A (1x1) pattern, which corresponds to a monolayer coverage, was observed. Although a monolayer coverage gives the diffraction spots in identical positions as obtained in Figure 11a, the intensities of spots are altered. Such a (1x1) pattern for oxygen interaction on V(100) surface was obtained earlier by Vijai and Packman (2), who also observed a (2x2) diffraction pattern at 1100°C. The (2x2) pattern indicates that the unit cell of the adsorbed surface is twice the size of the unit cell of the pure vanadium (100) surface (2). The atomic arrangement, and the corresponding laser diffraction pattern for the (2x2) pattern are shown in Figure 12, and it is observed that the oxygen coverage on the surface corresponds to a one-fourth of the monolayer. For simplicity, vanadium atoms below oxygen atoms are not shown in Figure 12a.

Although only two adsorption patterns for oxygen interaction with V(100) surface were reported in literature, a similar study on Mo(100) surface showed the existence of several other adsorption patterns besides



a



b

Figure 12a. Atomic arrangement of oxygen adsorbed V(100) surface giving rise to a (2x2)-O pattern.  
Bigger circles represent V atoms

Figure 12b. Laser diffraction pattern for the above atomic arrangement

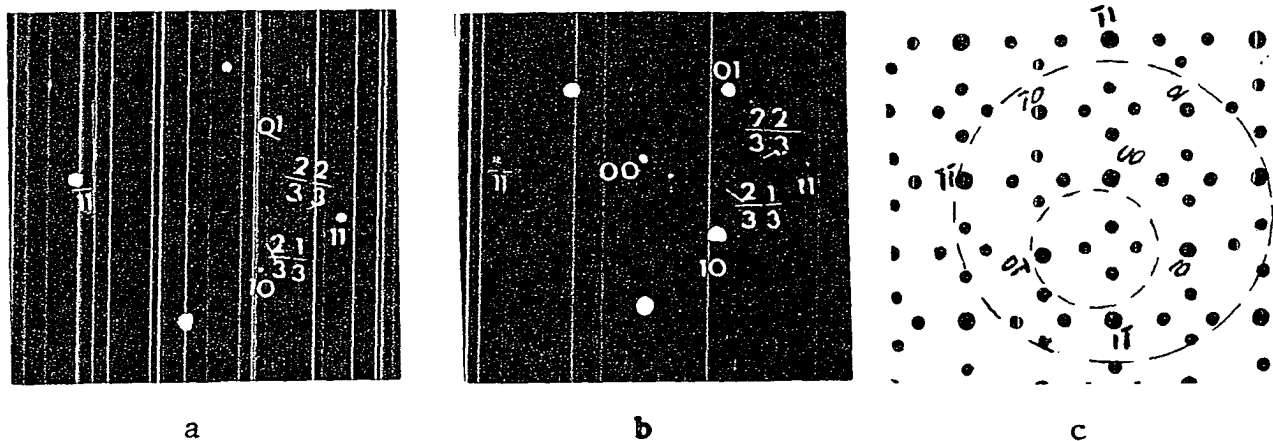
the (1x1) and (2x2) patterns (3). This is in contrast to the studies on (110) surfaces in which case identical oxygen adsorption patterns are observed for both V and Mo (4). Thus, to investigate the possibility of other ordered arrangements on V(100) surface, several exposures in the range  $10^{-8}$  to  $10^{-6}$  torr were carried out at about 900°C. At  $10^{-8}$  torr, no change in the (1x1) diffraction pattern was observed after 100 sec except that the background was found to increase. However, when the vanadium surface was exposed to  $10^{-6}$  torr oxygen pressure at 900°C for 5 minutes and then held at 900°C for 15 minutes without any oxygen input in the system, a distinctly different diffraction pattern was obtained, as shown in Figure 13a. Further heating for less than 15 minutes was found to make the pattern appear sharper although these extra spots completely disappeared on prolonged heating.

Although the diffraction spots in Figure 13a are not well defined, a comparison with the diffraction pattern of pure vanadium clearly shows the presence of extra spots due to oxygen adsorption. Figures 13a and 13b show that these spots are  $(\frac{2}{3} \frac{2}{3})$ ,  $(\frac{2}{3} \frac{1}{3})$ ,  $(\frac{1}{3} \frac{2}{3})$  and  $(\frac{1}{3} \frac{1}{3})$ . In Figure 13b the diffraction pattern is taken with the (00) beam off-centered so that the presence of  $(\frac{1}{3} \frac{1}{3})$  spots is clearly seen. For clarity, this pattern is sketched in Figure 13c, between the two dotted circles, and using symmetry properties it is extended to show the nature of the diffraction pattern.

#### Analysis of the diffraction pattern

The diffraction pattern observed in Figure 11a and 11b can now be analyzed by using the procedure given by Park and Madden (22). The extended





- Figure 13a. LEED pattern of V(100) surface after oxygen adsorption at normal angle of incidence
- Figure 13b. The above pattern with the (00) beam off centered so as to reveal the  $(1/3, 1/3)$  spots clearly
- Figure 13c. A schematic sketch of the above pattern

sketch of the diffraction pattern, shown in Figure 13c, can be considered as a superimposition of two patterns shown in Figures 14a and 14b. It is seen that the patterns of 14a and 14b are mirror images of each other and the diffraction spots due to the original substrate lattice correspond to the lattice sites which are common to both 14a and 14b. The mirror symmetry is due to the presence of two domains at  $90^\circ$  to each other.

The lattice points of Figure 14a can be generated by repeating the primitive cell  $A^*$  which can be represented by the vectors  $\vec{A}_1^* = (\frac{1}{3}\hat{i} - \frac{1}{3}\hat{j})$  and  $\vec{A}_2^* = (\frac{2}{3}\hat{i} + \frac{1}{3}\hat{j})$ . Similarly the lattice points of Figure 14b can be generated by the vectors  $\vec{B}_1^* = (\frac{1}{3}\hat{i} + \frac{1}{3}\hat{j})$  and  $\vec{B}_2^* = (\frac{1}{3}\hat{i} - \frac{2}{3}\hat{j})$ . Since the lattice of Figure 12c can be obtained by a superimposition of the lattices of Figure 14a and 14b, the lattice of Figure 13c can be generated by the sets of vectors  $A_1^*$ ,  $A_2^*$ ,  $B_1^*$  and  $B_2^*$ . In matrix notation one can write the above vectors as the matrices

$$\underline{A}^* = \begin{pmatrix} \frac{1}{3} & -\frac{1}{3} \\ \frac{2}{3} & \frac{1}{3} \end{pmatrix} \text{ and } \underline{B}^* = \begin{pmatrix} \frac{1}{3} & \frac{1}{3} \\ \frac{1}{3} & -\frac{2}{3} \end{pmatrix}$$

where the matrix elements ( $A_{ij}^*$  and  $B_{ij}^*$ ) are related to the vectors as  $\vec{A}_n^* = (A_{n1}^*\hat{i} + A_{n2}^*\hat{j})$ ;  $n = 1, 2$  and similarly for the  $B^*$  matrix.

Following the procedure of Park and Madden (22), the real space lattice can be now obtained from the inverse of the above matrices. Thus the vectors of the matrices

$$\underline{A} = \begin{pmatrix} 1 & 1 \\ -2 & 1 \end{pmatrix} \text{ and } \underline{B} = \begin{pmatrix} -2 & -1 \\ -1 & 1 \end{pmatrix}$$

will generate the real space lattice. The real space lattices generated by

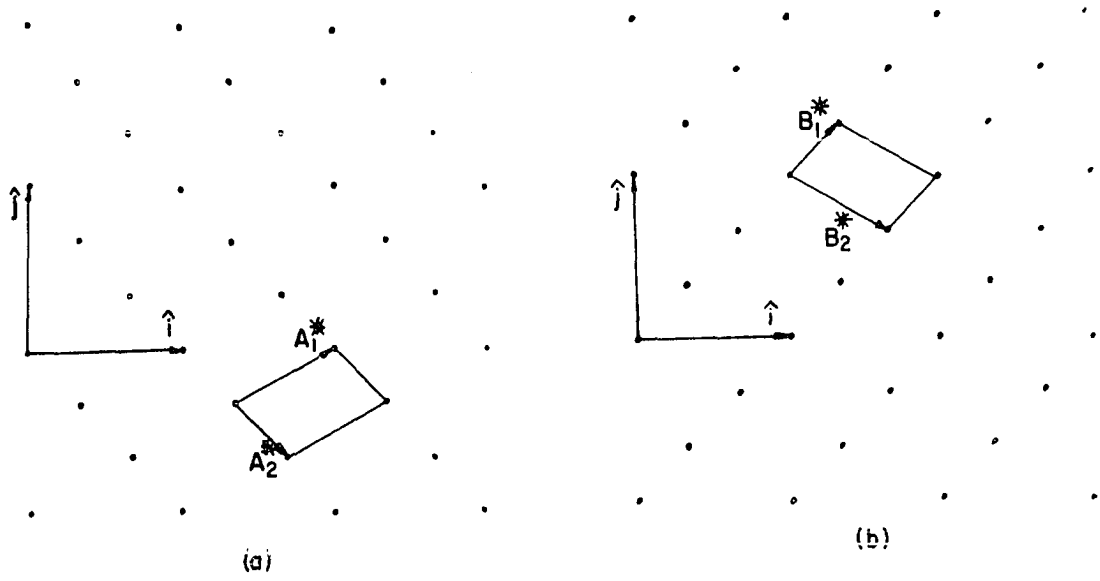


Figure 14. Two diffraction patterns which would give the pattern shown in Figure 13c when superimposed

the matrices A and B are shown in Figures 15a and 15b, respectively. It is seen that these two are domains which are mirror images of each other. Since the B.C.C. (100) plane possesses four fold symmetry, there would be two more domains which are mirror images of the above two. These additional domains, although present, could not be revealed in the analysis of the diffraction pattern since they give rise to diffraction spots coincident with those due to the lattices corresponding to the matrices A and B. An atomic arrangement corresponding to a surface having all the four domains is shown in Figure 16a. One must note, however, that this atomic arrangement is not unique. Several arrangements can possibly be proposed for the same lattice. For example, it is noted that the same pattern can be produced by altering the sites of vanadium atoms and the sites of adsorbed oxygen atoms. In order to determine the exact configuration, one needs to determine the ratios of the two species on the surface. Having one row of oxygen adsorbed sites alternating with two rows of pure vanadium atoms would give a ratio of impurity 1:2 whereas the other arrangement would give a ratio 2:1 for the impurity concentration. The laser simulation of the diffraction pattern for the atomic arrangement of an oxygen adsorbed surface is given in Figure 16b, which compares well with the extended sketch of the diffraction pattern (Figure 13c). The one third order spots which characterize the diffraction pattern are seen in the laser simulated pattern.

### Discussion

Earlier LEED studies of oxygen adsorption on vanadium by Vijai and Packman (2) showed the presence of a (1x1) pattern which transforms to a

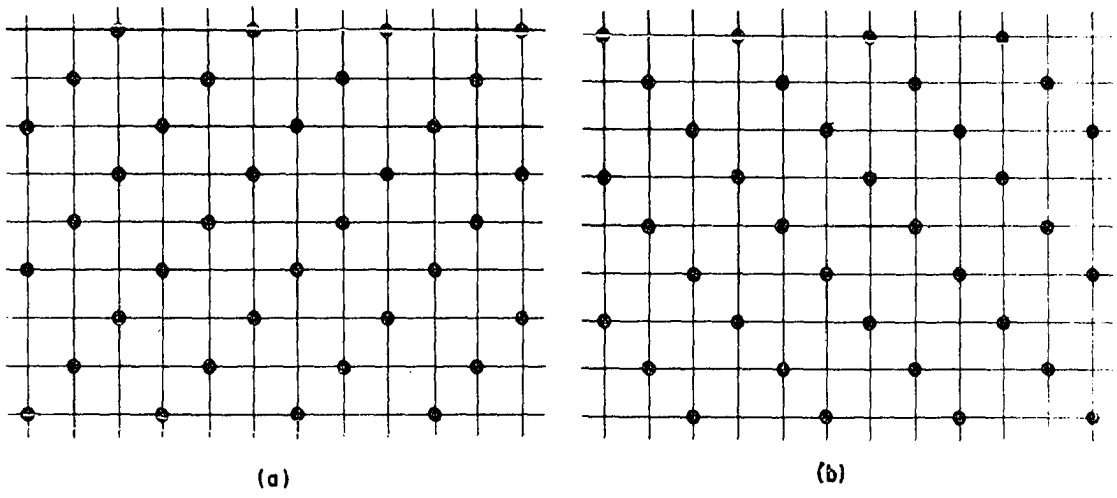
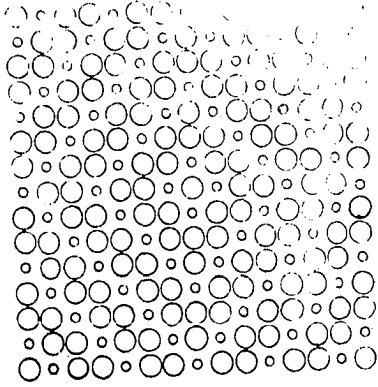
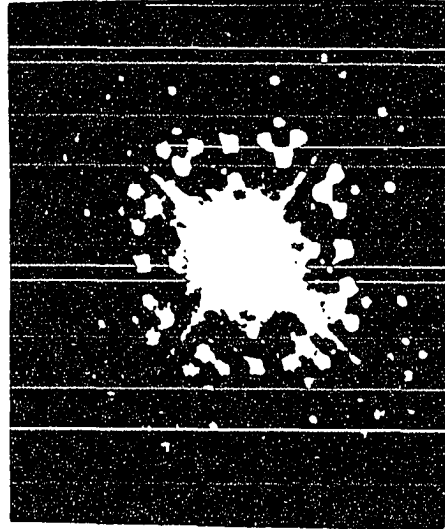


Figure 15. The real space lattices which correspond to diffraction patterns shown in Figures 14a and 14b



(a)



(b)

Figure 16a. A proposed model for the atomic arrangement of adsorbed oxygen atoms

Figure 16b. A laser diffraction pattern of the atomic arrangement

(2x2) pattern upon heating. The  $(1/2 \ 1/2)$  spots of the (2x2) pattern, shown in Figure 12b, were found to be stable and could not be removed either by heating or by argon ion bombardment or by a combination of both. The diffraction pattern, observed in the present work (Figure 13a), is intermediate between the (1x1) and (2x2) patterns since the ratio of oxygen atoms to vanadium atoms on the surface is intermediate between those in the (1x1) and (2x2) structures.

A similar intermediate pattern for the adsorption of oxygen on a (100) surface has been reported on molybdenum by Hayek and Farnsworth (3). They observed that the adsorption of oxygen on molybdenum was disordered if the specimen had not been heated after adsorption. Heating the specimen after adsorption produced a C(2x2) pattern which on further heating decomposed to a structure in which clean molybdenum sites alternated with two oxygen adsorbed sites, and they concluded that some oxygen was desorbed during the heat treatment of the C(2x2) structure, since the  $(1/3 \ 1/3)$  spots appeared after the disappearance of  $(1/2 \ 1/2)$  spots. They also mentioned that the alternate arrangements of two rows of oxygen alternating with one row of molybdenum atoms would suggest the possibility of the displaced molybdenum atoms positioned above the oxygen atoms in a superlattice arrangement. Kahn and Feuerstein (14) also studied the kinetics of oxygen adsorption on the molybdenum surface. They observed that the exposure of oxygen on a C(2x2) structure at a temperature of 750°C caused the  $(1/2 \ 1/2)$  spots to become initially streaky and then unobservable on continuous exposure to oxygen. Further exposure resulted in another intermediate structure and then to a (2x2) structure. Still

further exposure resulted in the disappearance of the extra spots and the formation of a diffuse diffraction pattern. They could produce all of the above structures in the reverse order by heating the oxygen adsorbed specimen at various temperatures thereby desorbing various amounts of oxygen out of the specimen.

The above discussion shows that the adsorbed oxygen atoms on a (100) surface of B.C.C. vanadium form ordered arrangements which correspond to (1x1) and (2x2) patterns. Also, in between these two structures, an intermediate transient ordered arrangement is observed which is similar to the one observed for oxygen adsorption on the molybdenum (100) surface. This intermediate pattern, upon heating, either disappears, as in the case of a vanadium surface or it transforms to another ordered arrangement as in the case of the molybdenum surface. Such a change upon heating occurs either due to the removal of adsorbed oxygen atoms from the surface by diffusion into the bulk or by desorption of these atoms from the surface.

In the present work the sample was heated for 15 minutes at 900°C without any exposure to oxygen. During this period, oxygen atoms from the surface can diffuse to the bulk, and thus lower the surface coverage from a monolayer to a one-third monolayer. The plausibility of such a diffusion process can be seen by considering diffusion of oxygen atoms in vanadium. Using the diffusion data of Powers and Doyle (23), the diffusion coefficient of oxygen in vanadium at 900°C is  $5.028 \times 10^{-8} \text{ cm}^2/\text{sec}$ . Thus, in 15 minutes, the oxygen atoms could migrate to an average distance of 0.014 cm., which is of the order of the thickness of the vanadium sample used.



### Recommendations for future investigations

It is seen from the literature that LEED studies of oxygen adsorption on metal surfaces are not very systematic. Also it is seen that the adsorption structures obtained by certain investigators were not observed by others for the same surface under identical conditions. A very systematic study of adsorption should be undertaken in which the surface structures are observed as a function of exposure at constant temperature and as a function of temperature at constant exposure. The atomic arrangement inferred from the LEED patterns should be correlated with the arrangement of the metal and oxygen atoms in the various oxides. Such correlations have been very rare in the literature. With regard to vanadium, adsorption of oxygen on planes other than (100) should be studied. Studies on Ta and Nb have been carried out extensively on the (110) plane. Studies on the (100) plane of the above metals should be carried out to get a better comparison of the oxygen adsorption behavior of the Group V metals. Tracy and Blakely (17) have demonstrated that the kinetics of oxygen adsorption on W(110) and (112) planes (closest packed and more open planes) were markedly different. By repeating those experiments on V one would be able to understand the differences in adsorption behavior due to crystallographic anisotropy. At present LEED intensities are not well understood to uniquely interpret the LEED patterns. Data on the surface self diffusion coefficient of V as well as the diffusion coefficient of O on and near V surfaces, along with the observed LEED patterns, would aid in the study of oxygen interactions on V surface.

## SELF-DIFFUSION PHENOMENA ON METAL SURFACES

## Introduction

The migration of atoms over crystal surfaces was largely studied, until the last two decades, by the use of field emission microscopy, sintering technique and tracer diffusion technique. In the field-emission microscopy technique the field emitter tip is made of the material whose surface diffusion coefficient ( $D_s$ ) is of interest, and the smoothing of this tip due to surface diffusion is studied to obtain  $D_s$ . The two ways of studying the smoothing process are "ring rate method" and "protrusion decay." In the "ring rate" method the surface smoothing caused by surface diffusion is followed by measuring the time taken for the dissolution of one atomic layer which is indicated by the disappearance of a "ring" which is an image of that atomic layer. In the "protrusion decay" method the smoothing of the tip surface which has been made protruded by the application of a high electric field is followed by measuring the time taken for the decay of protrusions. This decay is indicated by the disappearance of bright spots due to the disappearance of the protrusions. Since the exact topography of the protrusion is not known it is not possible to obtain the absolute magnitude of  $D_s$ , although one can study the temperature dependence of  $D_s$  and obtain the activation energy for surface diffusion. However, one can approximate the protruded surface as a periodic profile and obtain absolute magnitudes of  $D_s$  within a factor of about 3. One must note that the above two methods are not useful to study materials whose field emission cannot be obtained due to their higher work

function and lower melting point. Also since the field emitter tip is hemispherical and covers a large range of crystallographic planes, the field emission technique cannot be used to obtain diffusion coefficients on specific crystallographic planes, and in specific crystallographic directions.

In the sintering technique one studies the rate at which a spherical shape of the material sinters to a plane surface of the same material. The rate of sintering is followed by measuring the radius of the neck formed between the sphere and the plane surface during sintering. One can obtain  $D_s$  values from such measurements since the rate of sintering is governed by matter transport due to surface diffusion. However, matter is also transported by other transport mechanisms, one of which is bulk diffusion. The exact interpretation of experimental data on neck growth to obtain  $D_s$  is quite difficult because of the complex geometry near the neck region. Also one cannot obtain  $D_s$  for specific crystallographic planes for the same reasons as mentioned above.

Other techniques which were used to study the surface self-diffusion coefficients include radioactive tracer diffusion techniques. The earlier theoretical tracer work was inadequate in that the loss of tracer into the crystal interior due to lattice diffusion was not taken into account. However, a recent analysis by Shewmon (24) of surface diffusion from a point source does take bulk diffusion into account. This was essentially the state of art until the late 1950's. In 1957, Mullins (25-27) gave a new dimension to the field of surface self-diffusion when he published a series of articles dealing with changes in surface morphologies caused by

matter transport, surface diffusion being one of the prominent transport mechanisms.

The mass transfer processes studied by Mullins include the growth of a grain boundary groove and the flattening of corrugated surfaces. Mullins' solution to these problems permitted the determination of surface self diffusion coefficients from experimental measurements on the rate of change of groove width for the grain boundary grooving experiments or from measurements on the change in amplitude of corrugated surfaces. Among the various experimental methods developed as a result of Mullins' work to determine surface self-diffusion coefficients, grain boundary grooving technique has been one of the most widely used techniques, although recently multiple scratch decay technique is being preferred because of the possibility of in situ measurements by the use of laser diffraction.

Various experimental investigations of surface diffusion have been made by using the grain boundary grooving technique. The surface self-diffusion coefficients of copper in a hydrogen atmosphere have been measured by Mullins and Shewmon (M-s) (28) and Gjostein (7) for the (100) orientation, and by Choi and Shewmon (29) for various low and high index orientations. This grain boundary grooving technique was also used by Collins and Shewmon (30) to obtain surface diffusion coefficients of copper in  $H_2S$  doped  $H_2$ , and by Robertson (31) to measure volume diffusion coefficients of copper in liquid lead. Besides Cu, the diffusion coefficients of W (32,33), Mo (34,35), Au (36,37), Ag (38,39) and Fe (40) have been studied using the grain boundary grooving technique. All the available experimental data on grain boundary groove growth are summarized

in Table 4.

In this thesis we shall be concerned with the theory of grain boundary groove growth. We shall first discuss the reasons for the existence of a grain boundary groove, and then study various transport mechanisms by which such a groove deepens and widens with time.

#### Grain Boundary Groove Model

Consider a grain boundary which intersects an initially flat surface. At the intersection, the requirement of equilibrium between the surface and grain boundary energies will cause a small rearrangement of atoms and produce a groove as shown in Figure 17. For a stationary grain boundary, local equilibrium is established at the root of such a groove, and the equilibrium condition is derived by Herring (41) in terms of the interfacial energies,  $\gamma_i$ , and the torque terms  $\tau_i$ s. If  $t_i$  and  $n_i$  are unit vectors in the directions of tangent and normal to an interface, then the equilibrium condition is given as

$$\sum_{i=1}^3 (\gamma_i t_i + \tau_i n_i) = 0 \quad (5)$$

If torque terms are negligible, and if the grain boundary is normal to the surface, the above condition simplifies to

$$\sin \theta = \gamma_b / 2\gamma_s \quad (6)$$

In the above expression  $\gamma_b$  and  $\gamma_s$  are the respective interfacial energies of the grain boundary and the free surfaces, and  $\theta$  is their intersection

Table 4. The zero ( $x_0$ ), width ( $w$ ) and geometrical factor ( $g$ ) of a grain boundary groove developed under the combined action of surface and volume diffusion mechanisms.  $p = 0$  corresponds to pure surface diffusion.  $p = \infty$  corresponds to pure volume diffusion

$p$	$q$	$x_0/(Bt)^{1/4}$	$W/(Bt)^{1/4}$	$\frac{g}{m}(x \cdot 10^{-2})$
0.000	$\infty$	1.145	4.600	3.582
0.300	3.979	1.280	5.028	3.661
0.600	1.976	1.398	5.414	3.705
1.000	1.000	1.535	5.874	3.738
1.500	0.582	1.683	6.381	3.758
2.000	0.397	1.811	6.830	3.768
2.500	0.295	1.925	7.232	3.774
3.000	0.231	2.027	7.599	3.777
3.344	0.2	2.093	7.835	3.776 <sup>a,b</sup>
3.500	0.188	2.121	7.936	3.779
4.149	0.15	2.471	8.337	3.779 <sup>a</sup>
$\infty$	0	$\infty$	$\infty$	3.780 <sup>a</sup>

<sup>a</sup>The numerical values were evaluated proceeding from Equation 56b.

<sup>b</sup>Discrepancy in this is due to round off errors in numerical evaluation.

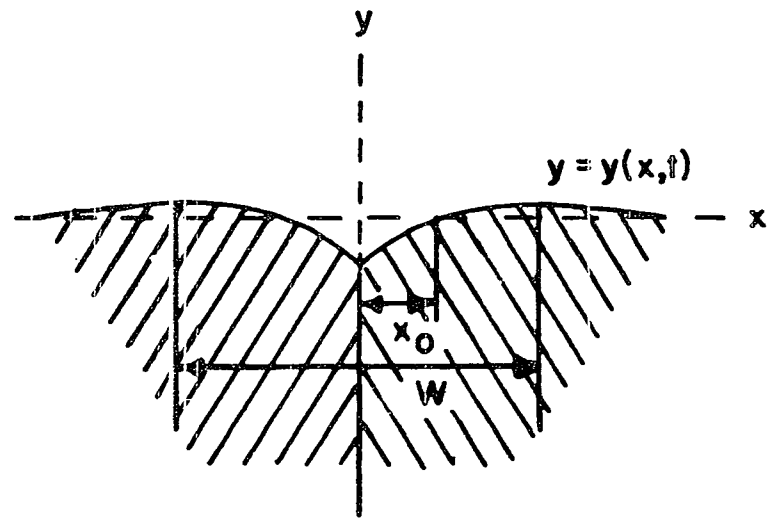


Figure 17. A schematic diagram of a grain boundary groove

angle. This equilibrium condition leads to a curvature of the surface profile near the grain boundary intersection as shown in Figure 17. The curvature of the groove profile varies from point to point and sets up a chemical potential gradient along the surface which drives atoms from regions of higher chemical potential (near the groove root) to those of lower chemical potential (far away from the groove root) so that the groove deepens with time. The matter transport necessary for the groove growth occurs by the mechanisms (1) evaporation-condensation, (2) volume diffusion, and (3) surface diffusion. Mullins (25,26) developed theories to explain groove growth when only one of the above mechanisms is present. He showed that the groove develops with a time independent shape and its linear dimensions are proportional to  $t^{1/2}$ ,  $t^{1/3}$  and  $t^{1/4}$ , respectively, for the above three mechanisms of matter transport.

In order to develop a simple mathematical treatment of the grain boundary grooving problem, certain simplifying assumptions are made. These assumptions are that

- (1) the surface properties are independent of crystallographic orientation
- (2) the absolute magnitudes of all slopes assumed by the surface is small compared to unity
- (3) macroscopic concepts such as surface free energy and surface curvature are valid
- (4) there is negligible flow of matter out of the grain boundary proper
- (5) the groove is symmetrical so that only one side of the groove



needs to be considered for the theoretical analysis.

We shall first examine the general assumptions stated above which are applicable to all cases of matter transport.

(1) Surface properties are assumed to be independent of crystallographic orientation. The grain boundary groove is made up of crystallographic planes which are of orientations slightly different from the simple plane of the free surface. The surface energy as well as the diffusion coefficients on these surfaces are different. However, in order to be able to treat the problem mathematically, one has to assume these properties to be constant. The available information on surface energy and diffusion coefficient values show that the change in these properties with surface orientation is negligible. McLean and Gale (42) who have obtained values of surface energy as a function of orientation have found that, for pure Cu annealed in dry hydrogen at 1030°C, the ratio of the maximum value of surface energy to that of the (111) plane (which should have the least value of surface energy in the case of F.C.C. metals) is 1.021. After going through Mullins' analysis one can see that the error introduced in the diffusion coefficient values, obtained by the grain boundary grooving technique, due to using a constant value for surface energy would be about 2%. This is much less than the experimental error involved in measuring the width of the groove, namely 5%. Also in actual experiments the grain boundary groove surface does not deviate to a great extent from the original surface which is usually a simple plane. For a groove developed by surface diffusion mechanism, Figure 18 shows the values of slope, curvature and flux of atoms at various points on the groove surface. The

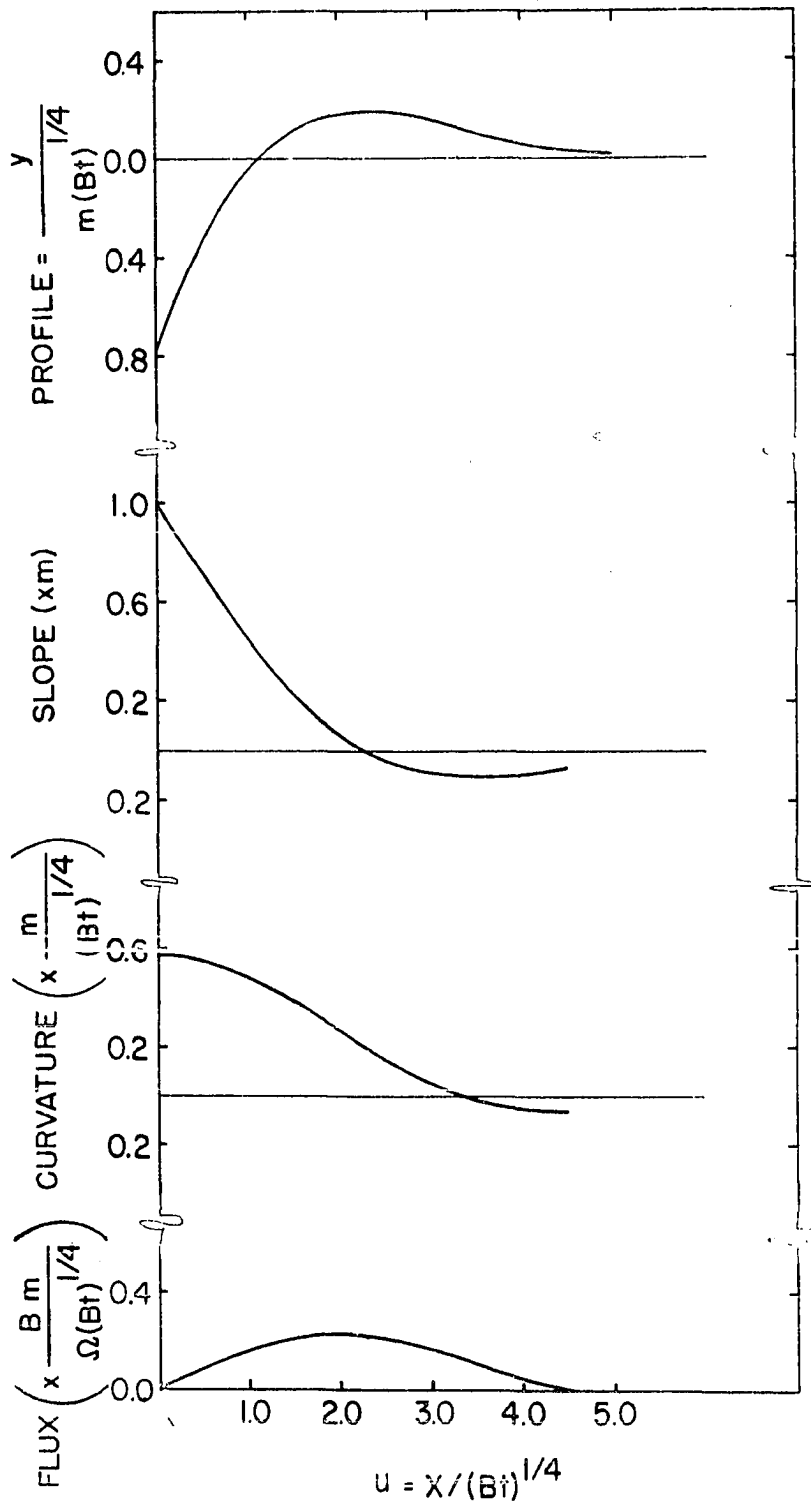


Figure 18. A grain boundary groove profile and the variation of slope, curvature and flux along the profile

parameter  $B$  is equal to  $D_s \gamma \Omega^2 v / RT$ , where  $\Omega$  is the atomic volume and  $v$  the surface density of atoms. From Figure 18b one can see that it is at the groove root where the surface orientation is the most deviated from the original surface. The above deviation, which is independent of time and which is solely determined by the relative values of  $\gamma_s$  and  $\gamma_b$ , is equal to  $\sin^{-1}(\gamma_b / 2\gamma_s)$  and has been reported to be about  $9^\circ$  for Cu (43).

(2) The absolute magnitudes of all slopes assumed by the profile of the groove surface are assumed to be small compared to unity. This restriction of small slope seems to be reasonably satisfied for most of the grain boundary grooves observed in vacuum or inert atmospheres (44). However, in the case of grooves formed in the presence of surface active environments the value of  $m$  can be much greater than unity.

Robertson (44) has obtained groove profiles on relaxing the above assumption, and has numerically solved the differential equation of Mullins which does not assume small slopes. His solutions have shown that the groove width is essentially independent of slope value,  $m$ , for  $0 < m < 4$  although the groove depth decreases considerably with increasing values of slope (about 10% error in depth for  $0 < m < 0.7$ ). Since all surface diffusion results are obtained from the analysis of the width data, the small slope approximation is well justified. The small slope approximation simplifies mathematical treatment since under this condition the curvature of the profile is given by the negative of the second derivative and the rate of normal motion is equal to the rate of change of the  $y$  coordinate of the profile.

(3) It is assumed that macroscopic concepts as surface curvature and

surface energy can adequately describe the process of grooving. Although the atomistic nature of crystals is important during the initial stages of grooving when the groove depth is a few atomic diameters, this assumption should be valid during the later development of the groove.

(4) The volume of grain boundary material that disappears is completely negligible compared to the volume of material transported to form the groove. Therefore, the current of atoms out of the grain boundary is assumed to be zero. One can quantitatively compare the flux at groove root to the maximum flux, as follows, in order to see the validity of the above assumption.

Assuming a grain boundary thickness of  $\delta$ , the volume of grain boundary material per unit length of groove,  $V_{x=0}$ , is equal to  $-0.78 m(Bt)^{1/4} \delta/2$  where  $m$  is the slope at the groove root and  $B$  and  $t$  are explained in later sections. Thus the surface flux at the groove root,  $J_{x=0}$ , is

$$J_{x=0} = \frac{\delta}{\delta t} \left( - \frac{0.78 m (Bt)^{1/4} \delta}{2 \Omega} \right). \quad (7a)$$

where  $\Omega$  is the atomic volume  $\approx 0.1 \frac{\delta}{\Omega} \frac{mB}{(Bt)^{3/4}}$ . The maximum flux can be calculated and has the value

$$J_{\max} \approx 2 \frac{Bm}{\Omega (Bt)^{1/2}} \quad (7b)$$

$$\approx \frac{2}{4.6} \frac{BmW}{\Omega (Bt)^{3/4}} \quad (7c)$$

where  $W$  is the width of the groove. Thus one obtains

$$\frac{J_{x=0}}{J_{\max}} \approx 0.2 \frac{\delta}{W} . \quad (7d)$$

Thus assuming the boundary thickness to be about  $5 \text{ \AA}$ , the flux at groove root is only  $4 \times 10^{-6}$  of the maximum flux for a groove of  $25\mu$  width.

This assumption of equating the flux at groove root to zero value implies that  $\partial^3 y / \partial x^3$  at groove root is quite negligible. This enables us to treat the diffusion problem for  $x > 0$  only with the boundary condition of zero normal flux at the symmetry plane ( $x = 0$ ).

#### Earlier Theories on the Growth of Grain Boundary Grooves

The theoretical analysis of grain boundary groove by surface diffusion, volume diffusion or evaporation condensation mechanism has been developed in detail by Mullins (25,26). An approximate analysis is also given by Mullins and Shewmon (28) for the case when more than one transport mechanism is present. We shall now briefly discuss these theories and point out the inadequacies in the Mullins-Shewmon theory.

#### Evaporation-condensation mechanism

Although evaporation-condensation is one of the mechanisms of matter transport, its contribution to groove development is not significant except for metals which have high vapor pressure at the experimental temperatures. In the case of grain boundary grooving the effect of this mechanism is to increase the groove width. Also one must note that this mechanism when acting alone would not produce humps in the groove as shown in Figure 17 due to the fact that matter would not be conserved. Hence the study of

grooves produced by this mechanism acting alone is not of great value although one can obtain surface energy values by measuring the groove depth.

In addition to the various assumptions discussed before, Mullins assumed a closed system in which the metal vapor is in quasi-equilibrium with the metal phase. In the case of an open system, like in the case of a vacuum chamber where the ambient gases are constantly being pumped out, one cannot obtain equilibrium partial pressure of metal vapor and this treatment will not be applicable.

The growth of the grain boundary groove due to evaporation-condensation can be explained as follows. The curvature of the bicrystal surface, once the groove has been formed, will vary along the surface. The partial pressure of metal vapor in equilibrium with a surface segment of higher curvature (taken with the proper sign) will be higher than that at other segments of lower curvature. Since the number of atoms emitted per square centimeter area of a surface segment is proportional to the metal vapor pressure in equilibrium with it, segments of higher curvature will be losing atoms at a faster rate than segments of lower curvature. However, as can be seen from Mullins' (25) arguments, the flux of metal atoms impinging on the surface will have a constant value. Thus there will be a net loss of matter from segments having finite curvatures. Since surface segments near the groove root have higher curvature, material there will be lost constantly at a faster rate, thereby causing the groove to deepen.

In order to arrive at a differential equation for the profile, Mullins related the flux of atoms to the rate of change of profile. The normal

motion of the profile,  $\partial n/\partial t$ , is related to the rate of accumulation of atoms which is equal to the negative divergence of the flux,  $\partial J/\partial x$ .

Thus, we obtain

$$\frac{\partial n}{\partial t} = -\Omega \frac{\partial J}{\partial x} \quad (8a)$$

where  $\Omega$  is the atomic volume and  $dn$  is the normal distance moved by the given element of the interface. Under small slope approximations the above equation can be simplified since

$$\frac{\partial n}{\partial t} = \frac{1}{\cos\theta} \frac{\partial y}{\partial t} \approx \frac{\partial y}{\partial t} \quad (8b)$$

where  $\theta$  is the angle between the surface normal and y-axis which is very small.

Equating 8a and 8b we have

$$\frac{\partial y}{\partial t} = -\Omega \frac{\partial J}{\partial x} \quad (8c)$$

In order to calculate flux, consider the rate of emission of atoms by a surface segment which, from the kinetic theory of gases, is proportional to the vapor pressure,  $p$ , in equilibrium with the segment. The vapor pressure at various points of the curved surface can be obtained, using Gibbs-Thompson equation, as

$$\ln\left(\frac{p}{p_0}\right) = K \frac{\gamma\Omega}{kT} \quad (8d)$$

where  $p_0$  = vapor pressure in equilibrium with a plane surface

$K$  = curvature

$\gamma$  = surface energy

$k$  = Boltzmann constant

$T$  = absolute temperature

Mullins (25) obtained the following expression for the flux,  $\theta$ , of atoms emitted by a curved surface segment

$$\theta - \theta_o = \Delta\theta = K \frac{p_o \gamma \Omega}{(2\pi M)^{1/2} (kT)^{3/2}} \quad (8e)$$

where  $M$  is the molecular weight of the metal and  $\theta_o$  is the flux emitted by a plane surface. Mullins argued that the flux impinging on the surface will be  $\theta_o$  all along the profile, and hence  $\Delta\theta$  represents the net loss of atoms. Having obtained the flux of atoms in terms of curvature, a differential equation for profile can be obtained by using Equations 8d and 8e, which gives

$$\frac{\partial y}{\partial t} = A \frac{\partial^2 y}{\partial x^2}, \quad (9)$$

where

$$A = \frac{p_o \gamma \Omega^2}{(2\pi M)^{1/2} (kT)^{3/2}}.$$

The initial and boundary conditions are as follows. Since the surface was flat initially,

$$y(x, 0) = 0. \quad (10a)$$

Also the interfacial energies of the free surface and grain boundary



maintain a constant equilibrium angle,  $\tan^{-1} m$ , at groove root

$$\frac{\partial y}{\partial x}(0, t) = m. \quad (10b)$$

As shown earlier, the flux of atoms, which is proportional to  $\partial^3 y / \partial x^3$ , is equal to zero at the groove root

$$\frac{\partial^3 y}{\partial x^3}(0, t) = 0. \quad (10c)$$

The surface profile is flat far away from the groove

$$y(x, t), y'(x, t), y''(x, t), y^n(x, t) \rightarrow 0 \text{ as } x \rightarrow \infty, \quad (10d)$$

where prime (or superscript) denotes differentiation w.r.t.x. Mullins solved the differential Equation 9 subject to the above boundary conditions and showed that the groove profile due to evaporation-condensation can be represented by the equation

$$y(x, t) = -2m(At)^{1/2} \text{ierfc} \left[ \frac{x}{2(At)^{1/2}} \right] \quad (11)$$

where  $\text{ierfc}$  is the integral error function. The important conclusion from the above result is that all linear dimensions of the groove profile are proportional to  $t^{1/2}$ .

#### Surface diffusion mechanism

Mullins (25) derived a theory to predict the groove profile when surface diffusion is the only mechanism of matter transport. The differential equation was derived by using the Nernst-Einstein relation to calculate the surface flux in contrast to the previous case where kinetic theory of

gases was used to calculate the evaporation flux. Using the Nernst-Einstein relation the surface flux of atoms,  $J$ , can be related to the chemical potential gradient,  $\nabla\mu$ , as

$$J = - \frac{D_s v}{kT} \nabla\mu \quad (12a)$$

where  $D_s$  the surface self-diffusion coefficient. Assuming local equilibrium at the surface the chemical potential,  $\mu$ , along the surface can be obtained from the Gibbs-Thompson relation as

$$\mu = \mu_0 + \gamma\Omega K \quad (12b)$$

where  $\mu_0$  is the chemical potential of an atom on a flat surface, and  $K$  the curvature of the surface. From Equations 9a and 9b, the surface flux can be written as

$$J = - \frac{D_s \gamma\Omega v}{kT} \frac{\partial K}{\partial s} \quad (12c)$$

where  $v$  is the number of atoms per unit area and the coordinate  $s$  is along the surface. As before the flux can be related to the normal motion and hence to the rate of change of profile as

$$\frac{\partial y}{\partial t} = -B \frac{\partial}{\partial x} [(1+y'^2)^{-1/2}] \frac{\partial}{\partial x} \left( \frac{y''}{(1+y'^2)^{3/2}} \right) \quad (13a)$$

where

$$B = \frac{D_s \gamma\Omega^2 v}{kT} .$$

Since the slope of the profile has been assumed to be small,  $y'^2$  can be neglected compared to unity, which gives

$$\frac{\partial y}{\partial t} = -By'''' \quad (13b)$$

Mullins (25) solved the above differential equation subject to the initial and boundary conditions given by Equations 10a, 10b, 10c and 10d. The result was represented in a series form as follows:

$$y(x,t) = m(Bt)^{1/4} \sum_{n=0}^{\infty} a_n \left[ \frac{x}{(Bt)^{1/4}} \right]^n \quad (14a)$$

where the coefficients  $a_n$  are given by the recursion relation

$$a_{n+4} = a_n \frac{n-1}{4(n+1)(n+2)(n+3)(n+4)} \quad (14b)$$

and the values of the first four coefficients were,

$$a_0 = -\frac{1}{2^{1/2}\Gamma(5/4)}, \quad a_1 = 1, \quad a_2 = -\frac{1}{2^{3/2}\Gamma(3/4)}, \quad a_3 = 0 \quad (14c)$$

The above result shows that the groove develops with a time independent shape whereas its linear dimensions are proportional to  $t^{1/4}$ . Also the theory predicted the formation of humps in the profile, as shown in Figure 17, due to the build-up of matter removed from the groove. By numerically evaluating the profile shape, Mullins showed that the width of a grain boundary groove,  $W_s$ , under the action of surface diffusion mechanism can be given by

$$W_s = 4.6 (Bt)^{1/4} \quad (15)$$

This relationship shows that the value of B can be obtained from the

intercept of a log-log plot of groove width versus time. The intercept,  $(\ln 4.6 + 1/4 \ln B)$  gives the value of  $B$  from which  $D_s$  value can be calculated.

### Volume diffusion mechanisms

The diffusion path in the case of volume diffusion is not well defined as in the case of surface diffusion where matter is transported along the surface. However, the matter flux,  $J$ , can be calculated using Fick's law of diffusion, namely

$$J = -DVC \quad (16)$$

where  $D$  is the diffusion coefficient of the diffusing species and  $VC$  is the concentration gradient of the diffusing species. In the case of volume diffusion, the diffusing species are vacancies and one has to know the concentration field of vacancies,  $C(x,y,t)$ , in order to use Fick's law. Mullins (26) assumed that, for any given profile  $y(x,t)$  at time  $t$ , there will be a steady state concentration field of vacancies,  $C(x,y,t)$ , which will satisfy the Laplace's equation in the matrix and the boundary condition along the profile surface given by Gibbs-Thompson's equation. The assumption of steady state concentration field of vacancies can be justified by calculating how fast the vacancies migrate as compared to the change of groove profile. The highest rate of groove profile change which occurs at the root is about  $10^{-5}$  cm/sec for a groove formed in 1 hour and drops down to about  $10^{-6}$  cm/sec in a week. Whereas, the vacancies travel about  $10^{-2}$  cm in a sec, assuming a jump distance of  $3 \text{ \AA}$  and a jump frequency of  $10^{11}$  jumps/sec. Thus we may write

$$\nabla^2 C = 0 \quad (17a)$$

$$C(x,0,t) = C_0 - \frac{\gamma \Omega}{kT} K(x,t) + C_0 \quad (17b)$$

A solution to the above differential equation which satisfies the boundary condition can be written as

$$C(x,y,t) = C_0 - C_0 \frac{\gamma \Omega}{kT} \int_0^\infty d\omega \cos(\omega x) \exp(-\omega y) \int_0^\infty K(x,t) \cos(\omega x) dx \quad (17c)$$

The flux of vacancies can be obtained from the equation (Fick's law) which can be related to the rate of motion of an element of surface as follows:

$$\frac{\partial y}{\partial t} = D_{\text{vac}} \Omega \frac{\partial C}{\partial y} \text{ along the profile.} \quad (17d)$$

Under small slope approximations the values of concentration and its derivatives assume on the surface and on the plane  $y = 0$  can be identified. Using this approximation and substituting for  $\partial C / \partial y$  from Equation 17c and differentiating twice with respect to time, one can obtain an integrodifferential equation for the curvature of the grain boundary groove as

$$-\frac{\partial K}{\partial t} = A' \frac{2}{\pi} \int_0^\infty d\omega \omega^3 \cos(\omega x) \int_0^\infty K(x,t) \cos(\omega x) dx \quad (17e)$$

$$\text{where } A' = \frac{D_v \gamma \Omega}{kT}.$$

$D_v$  is the volume diffusion coefficient  $= D_{\text{vac}} \Omega C_0$ . Mullins (26)

solved the above integrodifferential equation, Equation 17e, subject to the initial and boundary conditions given by Equations 10a, 10b, 10c and 10d and obtained the grain boundary groove profile, due to volume diffusion, as follows:

$$y(x,t) = m(A't)^{1/3} \sum_{n=0}^{\infty} a_n \left[ \frac{x}{(A't)^{1/3}} \right]^{2n} \quad (18a)$$

where the  $a_n$  are given by

$$a_1 = 1 \quad (18b)$$

$$a_n = \frac{(-1)^n}{(2n)!} \Gamma\left(\frac{2n-1}{3}\right); n \text{ even} \quad (18c)$$

$$a_n = 0; n \text{ odd except for } n = 1. \quad (18d)$$

This result shows that the linear dimensions of a grain boundary groove under the action of volume diffusion are proportional to  $t^{1/3}$  as compared to the case of surface diffusion in which the linear dimensions are proportional to  $t^{1/4}$ . By numerically evaluating the profile shape given by Equation 18a, Mullins (26) obtained the width of a grain boundary groove, due to volume diffusion, as

$$W_v = 5.0(A't)^{1/3}. \quad (19)$$

#### Combined transport mechanisms

Mullins' (25,26) theories of grain boundary grooving outlined above cannot be used directly to analyze the experimental data on grooving. This

is due to the fact that, under ordinary experimental conditions, grain boundary grooving proceeds with all three mechanisms of matter transport (evaporation-condensation, volume diffusion, and surface diffusion) taking place simultaneously. However the relative importance of each depends upon the vapor pressure, the magnitude of the diffusion coefficients involved and the diffusion distance. Thus, in terms of experimental conditions, the relative importance is determined by the annealing temperature and time. In the initial stages of grooving, when the groove width is small, surface diffusion dominates, whereas at later times volume diffusion and evaporation-condensation become increasingly important. This is because the diffusion distance for surface diffusion, namely  $(Bt)^{1/4}$ , is larger than it is for volume diffusion, namely  $(A't)^{1/3}$ , during the initial stages and is reversed at later stages.

The effect of matter transport due to volume diffusion on the profile of a grain boundary groove, formed predominantly by surface diffusion mechanism, was first theoretically studied by Mullins and Shewmon (M-S) (28). In addition to the approximations mentioned earlier, they made further approximations as given below.

(1) The curvature,  $K(x)$ , of the groove was approximated as a Gaussian expression of the form

$$K(x) \approx h \exp(-bx^2) . \quad (20a)$$

(2) The parameters  $h$  and  $b$  were chosen so that the above expression would give the same value of curvature at the origin and point of inflexion of curvature as obtained for the case of pure surface diffusion. This approximation implies that the volume diffusion contribution for the

development of groove profile is small compared to the surface diffusion contribution.

(3) The volume of matter transported per unit length of the groove formed was assumed to be 0.042 times the product of slope and square of the width. It should be noted that the above value is not in between those for the cases of pure surface and volume diffusion (0.0358 and 0.0378) as it should be. Also this value should depend on the extent of volume diffusion mechanism rather than being constant.

For the assumed form curvature, M-S calculated the flux of material due to volume diffusion,  $J_v(x)$ , as outlined in the previous section. Knowing the volume diffusion flux they calculated the rate of removal of atoms by volume diffusion,  $r_v$ , which is

$$r_v = \int_{-x_0}^{x_0} J_v(s) dx \quad (20b)$$

where  $\pm x_0$  represent the zeroes of the flux. They also calculated the rate of removal of atoms by surface diffusion,  $r_s$ , from the shape of the groove profile for the case of pure surface diffusion. Thus they obtained

$$r_v = \frac{1}{W} \left( \frac{3.7D_v \gamma m}{kT} \right) \quad (20c)$$

$$r_s = \frac{1}{W^2} \left( \frac{9.0D_s \gamma \Omega v m}{kT} \right) \quad (20d)$$

where  $W$  is the experimental groove width. They obtained a differential equation for  $W(t)$  by equating the sum of the rates of matter removed to the



derivative of the volume of matter removed divided by  $\Omega$

$$(r_s + r_v) = \frac{1}{\Omega} \frac{dV}{dt} = \frac{1}{\Omega} \frac{d}{dt} (0.042 \text{ mW}^2) \quad (20e)$$

where  $r_x$  and  $r_v$  are functions of  $W$ . By solving the above differential equation they obtained a relationship between the experimental width,  $W$ , and the width that would be observed if surface diffusion were the only transport mechanism present,  $W_s$ . The relationship is

$$\alpha W - (\alpha W)^2/2 + (\alpha W)^3/3 - \ln(1 + \alpha W) = (\alpha W_s)^4/4 \quad (21)$$

$$\text{where } \alpha = \frac{D_v}{2.4 D_s \Omega^{1/3}} .$$

Substituting the values of  $\alpha$  and  $W_s$  (from Equation 15) in Equation 21 one obtains a transcendental equation for  $D_s$ . This equation can be solved by an iterative procedure to yield a value of  $D_s$  under the condition that the values of  $\gamma$  and  $D_v$  are known. An iterative procedure along these lines was developed by Gjostein (7), and in fact the experimental workers mentioned above have used the iterative procedure. Such a procedure is quite simple if the surface diffusion mechanism predominates. However, when volume diffusion is important, a large number of iterations are required to obtain the surface diffusion coefficient (29,30). This is a serious drawback of M-S treatment. Also, the use of M-S theory in determining surface diffusion coefficients requires a prior knowledge of volume diffusion coefficient values. However, recent studies (45,46) show that the volume diffusion data in the vicinity of the surface may be

significantly different from those in the bulk. Thus the use of the bulk volume diffusion coefficient data would give erroneous results for the surface diffusion coefficient values.

### Theory of Grain Boundary Grooving Under Simultaneous Action of Various Transport Mechanisms

#### Need for the present analysis

In the last couple of years, the use of grain boundary grooving technique to determine surface diffusion coefficients has been questioned by McAlister and Cutler (M-C) (4,5). They argued that a finite groove width possibly present at the start of diffusion anneal will give erroneous results if the experimental groove widths are analyzed using a log-log plot of width vs time, as is conventionally done. They suggested that the groove width must be plotted against  $t^{1/n}$  (n being equal to 3 or 4 depending upon whether the dominant transport mechanism in groove formation was volume diffusion or surface diffusion). When they analyzed the data of Gjostein (7) on Cu at 1020°C using the above procedure, they found that the analysis indicated a negative initial width if surface diffusion mechanism had been assumed for the groove growth, a positive initial width was indicated. Therefore M-C concluded that volume diffusion was the transport mechanism in the experiments of Gjostein (7) and analyzed the groove width data to obtain volume diffusion coefficient values of Cu. These values of volume diffusion coefficient of Cu obtained by M-C are in much agreement with the values determined by Kuper et al. (47) from a tracer diffusion technique.

Gjostein (6) put forward the following arguments to refute the claim

of M-C that the groove growth during Gjostein's (7) experiments took place by volume diffusion mechanism. He demonstrated that one could obtain zero initial width if the experimental groove widths are analyzed using the same procedure of M-C after they are corrected for volume diffusion contribution using M-S (28) theory. He explained that the curvatures in the plots of raw experimental data versus  $t^{1/3}$  and  $t^{1/4}$  were responsible for the positive and negative initial widths obtained by M-C using a least square straight line analysis, as illustrated in Figure 19. Gjostein (6) also pointed out that the surface diffusion coefficient values he obtained were much in agreement with those obtained by Bonzel and Gjostein (48) using other techniques like sinusoidal profile decay.

Figure 20 shows the experimental data points of Gjostein for Cu at 1020°C along with calculated widths of grain boundary grooves formed by either of the diffusion mechanisms acting independently. Diffusion coefficient values of Gjostein (7) and Kuper et al. (47) were used in the calculations. It is seen that the experimental data points fall in between the two curves. Volume and surface diffusion coefficient values can now be obtained by matching the experimental data points to the theoretical widths predicted by Mullins (25,26). This is very similar to how M-C interpreted the experimental data. Unlike M-C's method, the initial width was forced to be zero. From Figure 21 which shows the matching of experimental data, it is seen that either of the diffusion mechanisms can equally well be supposed for grooving. Also the values of diffusion coefficients obtained, namely

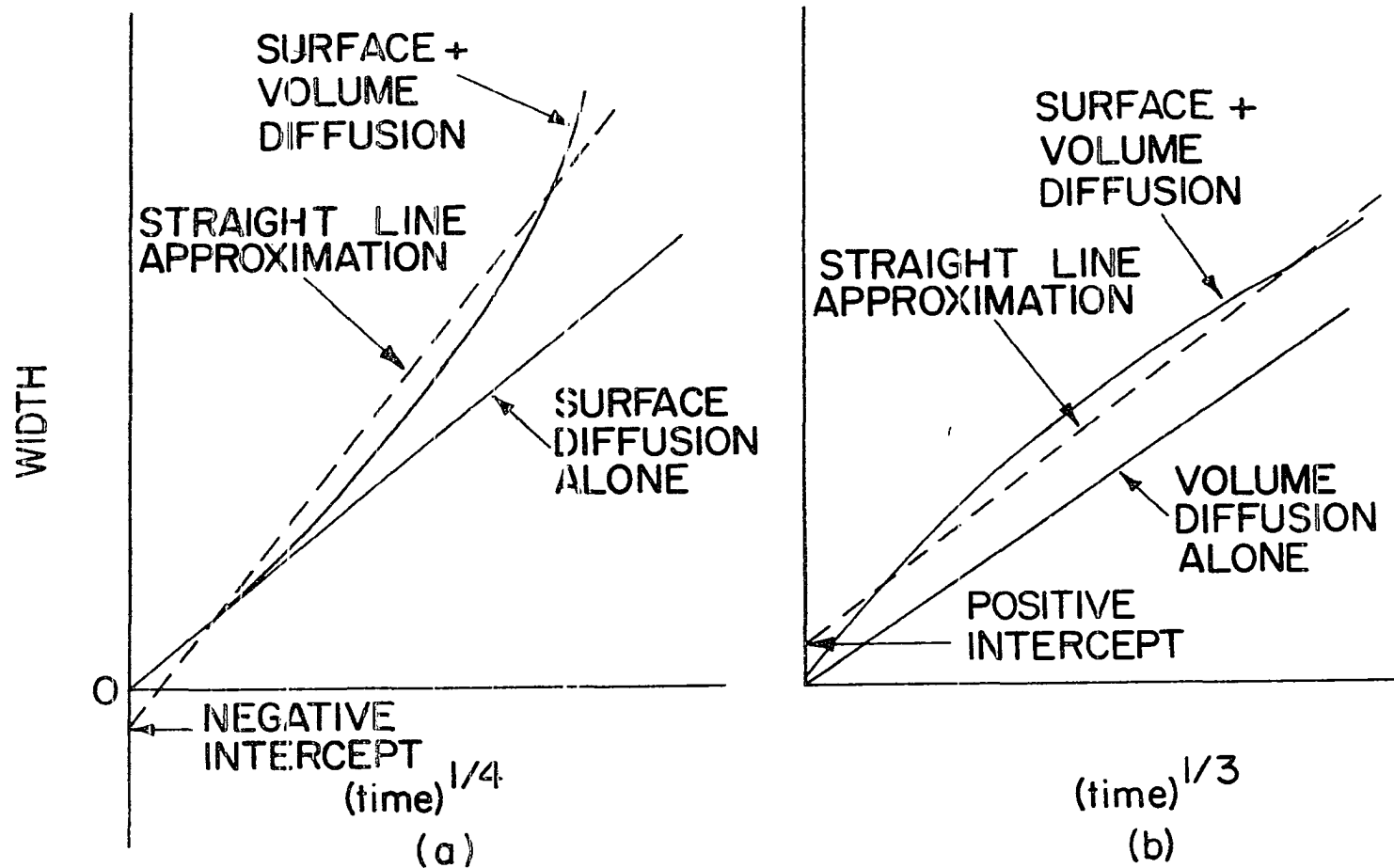


Figure 19. Plot of grain boundary groove width versus time when surface diffusion or volume diffusion mechanism is present and when both mechanisms are contributing to the matter transport

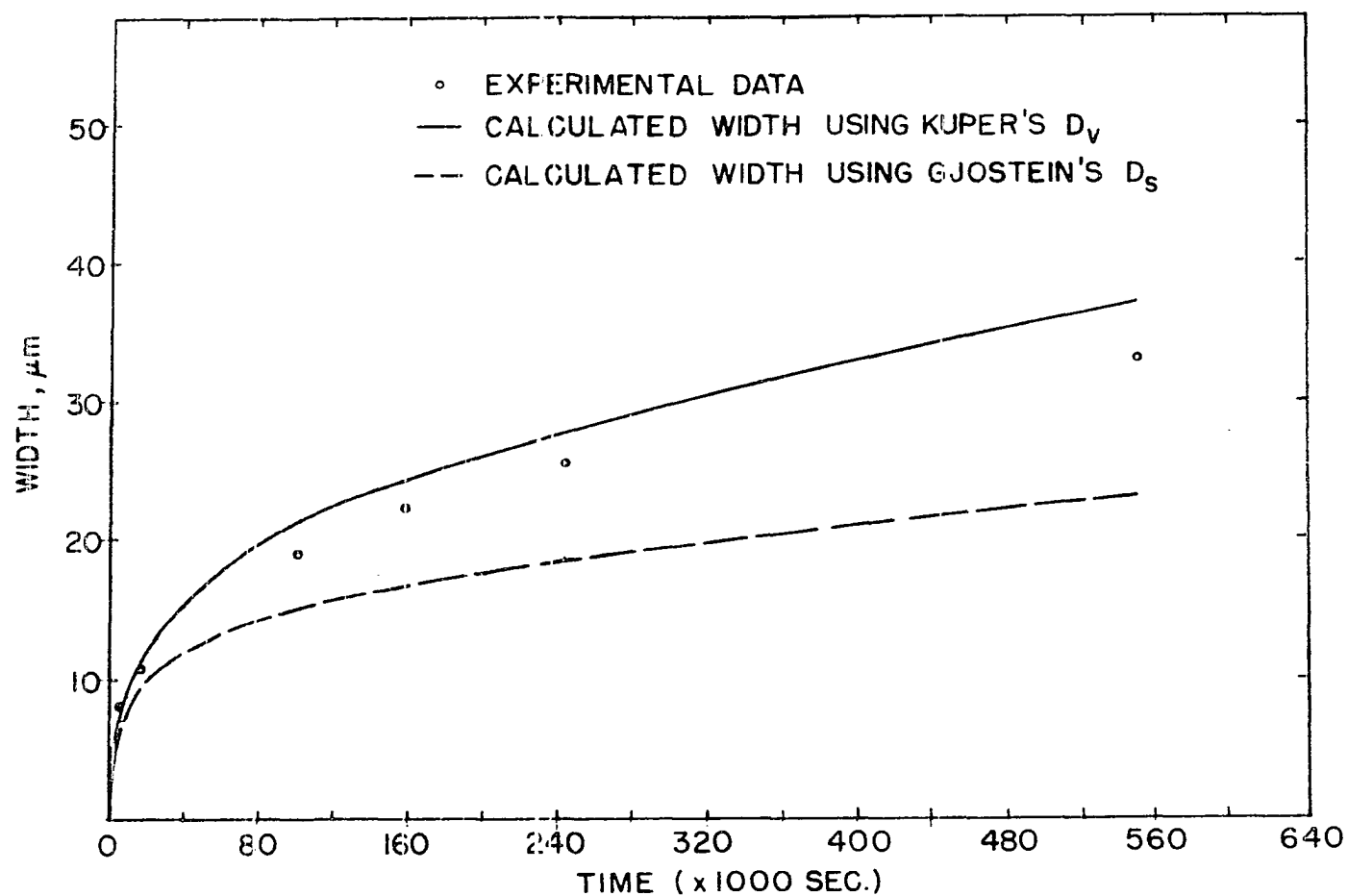


Figure 20. Experimental data on width versus time for copper. The lines represent theoretical calculations when only surface diffusion (dotted line) and only volume diffusion (solid line) mechanisms are contributing to the matters transport

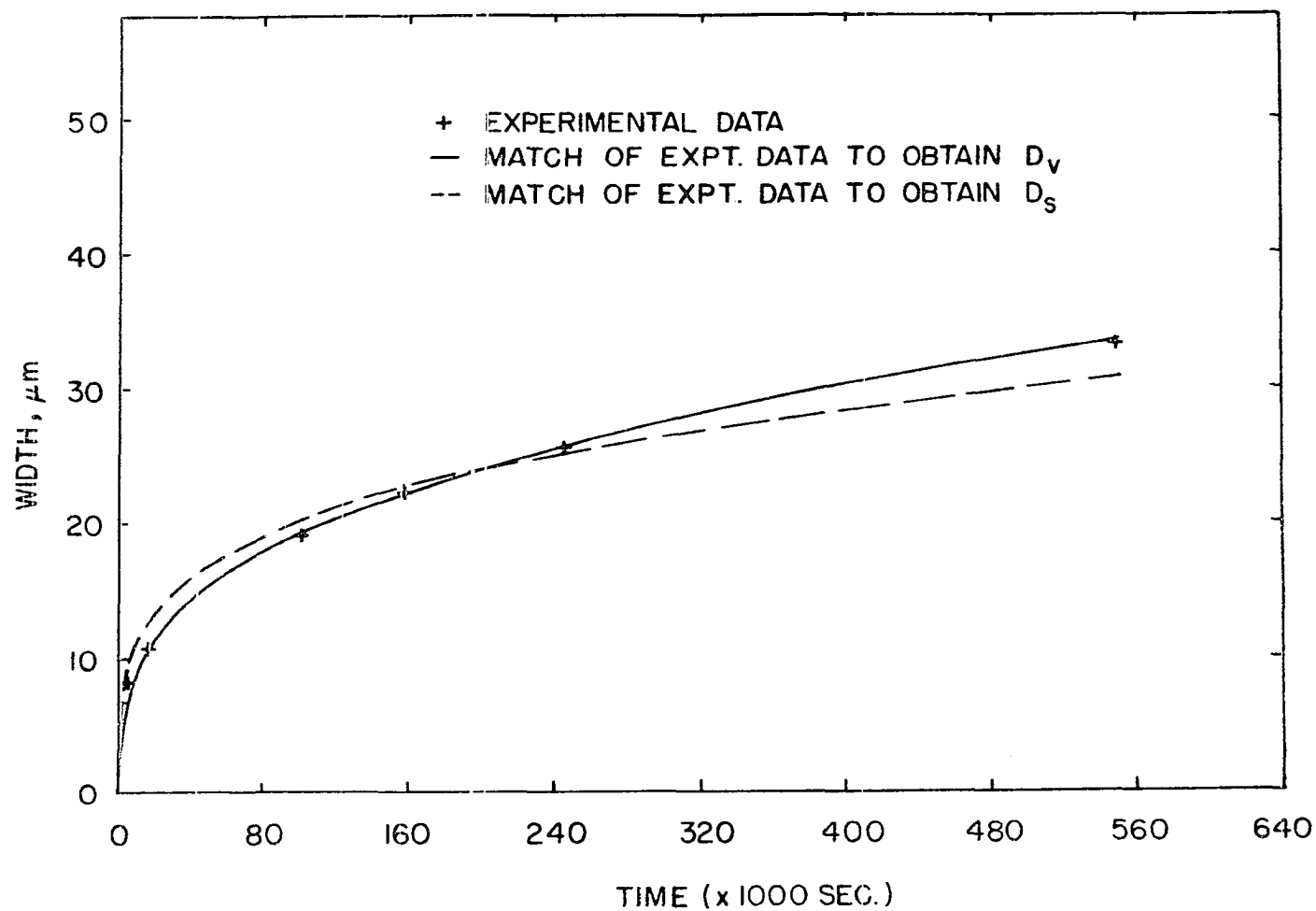


Figure 21. Calculations of  $D_v$  and  $D_s$  by matching theory with experimental results. Only one mechanism was assumed to be important for these calculations

$$D_s = 14.8 \times 10^{-5} \text{ cm}^2/\text{sec} \quad (22a)$$

$$D_v = 0.5 \times 10^{-8} \text{ cm}^2/\text{sec} \quad (22b)$$

are in agreement with those obtained by Gjostein (7)

$$(D_s = 4.5 \times 10^{-5} \text{ cm}^2/\text{sec})$$

and Kuper et al. (47)

$$(D_v = 2.2 \times 10^{-8} \text{ cm}^2/\text{sec}).$$

It is also seen that the volume diffusion coefficient value is underestimated and surface diffusion coefficient value is overestimated, if the experimental data are interpreted assuming either one of the mechanisms to be solely responsible. This indicates that both the diffusion mechanisms should be taken into consideration while analyzing grain boundary groove data.

Thus we see that one can assume either of the diffusion mechanisms (volume diffusion and surface diffusion) for the grain boundary groove growth and obtain the corresponding diffusion coefficient values reasonably well. A theory of grain boundary grooving which does not assume the dominant transport mechanism will be useful to settle the above controversy. Such an analysis has been given by Mullins and Shewmon (28), although it has serious drawbacks of which the predominance of surface diffusion mechanism over volume diffusion mechanism is the most severe one. It is clearly seen that a theory of grain boundary grooving under the combined action of surface and volume diffusion mechanisms is essential for successful interpretation of grain boundary groove data in obtaining diffusion

coefficient values and in assessing the importance of various transport mechanisms. Such an analysis is developed in the next section.

### Theoretical model

The theoretical analysis is carried out under the assumptions of an isotropic surface energy and a small slope of the groove profile. The groove profiles are obtained in terms of a dimensionless parameter,  $p$ , which measures the relative importance of the two transport mechanisms. A method to analyze the experimental data is given which eliminates the iterative procedure and determines simultaneously the surface diffusion coefficient as well as the volume diffusion coefficient near the surface. To demonstrate the application of the present theory to obtain surface diffusion coefficient from grain boundary grooving data, experimental groove widths of Gjostein (7) and Mullins and Shewmon (28) on a copper (100) surface are analyzed. Also the predictions of the theory enable one to determine the predominant transport mechanism during the groove growth.

Let  $y(x,t)$  be the grain boundary groove profile (Figure 17). A differential equation for  $y(x,t)$  can be obtained by considering the rate of change of the profile due to both of the diffusional mechanisms. From Equation 13b

$$\left. \frac{dy}{dt} \right|_{v \cdot d} = -B \frac{\partial^4 y}{\partial x^4} \quad (23)$$

From Equation 17e

$$\left. \frac{\partial y}{\partial t} \right|_{v \cdot d} = -A' \frac{2}{\pi} \int_0^{\infty} dw w^3 \cos(wx) \int_0^{\infty} y(x,t) \cos(wx) dx \quad (24)$$



We obtain the total rate of change of the profile by adding Equation 23 and Equation 24 as follows:

$$\frac{\partial y}{\partial t} = -B \frac{\partial^4 y}{\partial x^4} - A' \frac{2}{\pi} \int_0^{\infty} dw w^3 \cos(wx) \int_0^{\infty} y(x,t) \cos(wx) dx . \quad (25)$$

A solution to the above integrodifferential equation subject to the initial and boundary conditions, given by Equations 10a, 10b, 10c and 10d, namely

$$y(x,0) = 0$$

$$y'(0^+,t) = m$$

$$y''(0^+,t) = 0$$

$$y(x,t), y'(x,t), y''(x,t), y^n(x,t), \rightarrow 0 \text{ as } x \rightarrow \infty$$

would represent the profile of a grain boundary groove formed under the simultaneous actions of surface and volume diffusion mechanisms. In order to solve Equation 25 we seek a solution of the form

$$y = m(Bt)^{1/4} [Z_0(u) + \sum_{n=1}^{\infty} p^n Z_n(u)] \quad (26a)$$

$$\text{where } u = \frac{x}{(Bt)^{1/4}} \quad (26b)$$

$$p = \frac{A't^{1/4}}{B^{3/4}} = \left[ \frac{(A't)^{1/3}}{(Bt)^{1/4}} \right]^3 . \quad (26c)$$

B and A' are defined by Equations 17e and 13a, respectively.

The above form was suggested by the results of an iterative procedure which had been tried at first. In the iterative procedure, the change in

shape, due to volume diffusion, of a profile whose curvature is the same as that in a pure surface diffusion case, was determined. The curvature of this new profile was then determined and thus successive iterations carried out. The results obtained after a couple of iterations suggested the form of grain boundary groove profile as given in Equation 26a. It is noted that  $p$ , introduced above, is a dimensionless parameter which measures the relative strength of the two diffusion mechanisms. When only the surface diffusion mechanism is important, the value of  $p$  is zero. Under this condition  $Z_0(u) = Z(u)$ , where  $Z(u)$  is the function given by Mullins (25).

One can obtain the differential equation and initial and boundary conditions of the problems in terms of the functions  $Z_n(u)$  and their derivatives by substituting Equation 26a into Equations 25. Thus we have

$$\frac{Z_0(u)}{4} - \frac{u\dot{Z}_0(u)}{4} + \sum_{i=1}^{\infty} \frac{p^i}{4} [(n+1)Z_n(u) - u\dot{Z}_n(u)] = \quad (27)$$

$$-\ddot{Z}_0(u) + \sum_{i=1}^{\infty} -p^i \ddot{Z}_n(u) + \frac{2}{\pi} \int_0^{\infty} dk \cos ku \, k \int_0^{\infty} \ddot{Z}_{n-1}(u) \cos ku \, du$$

and the corresponding initial and boundary conditions are

$$\dot{Z}_n(0) = 1 \quad \text{for } n = 0 \quad (28a)$$

$$= 0 \quad \text{for } n \neq 0 \quad (28b)$$

$$\ddot{Z}_n(0) = 0 \quad \text{for all } n \quad (28c)$$

$$Z_n(u), \dot{Z}_n(u), \ddot{Z}_n(u), \dddot{Z}_n(u) \rightarrow \infty \quad \text{for all } n \quad (28d)$$

where the dot sign represents differentiation with respect to the

variable  $u$ . The coefficients of  $p^n$  on both sides of Equation 27 must be equal since  $p$  is a function of time and  $Z_n(u)$ s are independent of time. This gives the following set of differential equations for the functions  $Z(u)$

$$-\frac{(n+1)}{4} Z_n(u) - \frac{u}{4} \dot{Z}_n(u) = -\ddot{Z}_n(u), \quad n = 0 \quad (29a)$$

and

$$\begin{aligned} \frac{(n+1)}{4} Z_n(u) - \frac{u}{4} \dot{Z}_n(u) = -\ddot{Z}_n(u) + \frac{2}{\pi} \int_0^\infty dk \, k \cos ku \int_0^\infty \ddot{Z}_{n-1}(u) \\ \cos ku \, du, \quad n \neq 0. \end{aligned} \quad (29b)$$

#### Solution of differential equations

Equation 29a can be written as

$$\ddot{Z}_0(u) - \frac{u}{4} \dot{Z}_0(u) + \frac{1}{4} Z_0(u) = 0 \quad (30)$$

The boundary conditions are given by Equations 28a-28c. Let

$$\int_0^\infty \ddot{Z}_0(u) \cos ku \, du = f(k). \quad (31)$$

By using the boundary conditions, and upon integrating by parts, we get the following relationships:

$$\int_0^\infty \ddot{Z}_0(u) \cos ku \, du = -k^2 f(k) \quad (32)$$

$$\begin{aligned} \int_0^\infty u \dot{Z}_0(u) \cos ku \, du &= \int_0^\infty \frac{\partial}{\partial k} [Z_0(u) \sin ku \, du] \\ &= -\frac{1}{k^2} + \frac{f'(k)}{k} - \frac{f(k)}{k^2} \end{aligned} \quad (33)$$

and

$$\int_0^{\infty} Z_0(u) \cos ku \, du = -\frac{1}{k^2} - \frac{f(k)}{k^2} . \quad (34)$$

Upon substituting Equations 32, 33 and 34 into Equation 30, we obtain the following differential equation for the function  $f(k)$

$$-k^2 f(k) - \frac{1}{4} \frac{f'(k)}{k} = 0 . \quad (35)$$

The solution of this differential equation is

$$f(k) = -I e^{-k^4} \quad (36)$$

where the constant of integration is obtained as

$$-I = \lim_{k \rightarrow 0} f(k) = \int_0^{\infty} \ddot{Z}_0(u) du = -1. \quad (37)$$

The value of the function  $Z_0(u)$  can now be obtained from Equation 34 as

$$\int_0^{\infty} Z_0(u) \cos ku \, du = -\frac{1}{k^2} + \frac{e^{-k^4}}{k^2} . \quad (38)$$

The inverse transform of the above equation gives

$$Z_0(u) = \frac{2}{\pi} \int_0^{\infty} \frac{1}{k^2} (e^{-k^4} - 1) \cos ku \, dk. \quad (39)$$

This result is identical to that obtained by Mullins (25) (in a series form) for the case of surface diffusion only, as is shown in Appendix I.

Substituting the result for the function  $Z_0(u)$  in Equation 29b, one obtains a differential equation for the function  $Z_1(u)$  which can be solved

in very much the same way as Equation 30. Likewise, each of the functions  $Z_n(u)$  can be determined from the knowledge of the corresponding function  $Z_{n-1}(u)$ . By the technique of mathematical induction it can be shown that the functions  $Z_n(u)$  are

$$Z_n(u) = \frac{2}{\pi} \int_0^{\infty} \frac{(-1)^n}{n!} k^{3n-2} e^{-k^4} \cos ku \, dk, \quad n \neq 0. \quad (40)$$

In order to derive the above result, let us assume

$$Z_n(u) = \frac{2}{\pi} \int_0^{\infty} \frac{(-1)^n}{n!} k^{3n-2} \exp(-k^4) \cos(ku) \, dk. \quad (41)$$

It can easily be seen that the above result is true for the cases  $n = 1, 2$ .

For  $n=n+1$ , Equation 29b gives

$$\begin{aligned} \frac{n+2}{4} Z_{n+1}(u) - \frac{u}{4} \dot{Z}_{n+1}(u) &= -\ddot{Z}_{n+1}(u) + \frac{2}{\pi} \int_0^{\infty} dk \exp(-k^4) k^{3n+1} \\ &\quad \cos(ku) \frac{(-1)^n}{n!}. \end{aligned} \quad (42)$$

The initial and boundary conditions are

$$\dot{Z}_{n+1}(0) = \ddot{Z}_{n+1}(u) = 0 \quad (43a)$$

$$Z_{n+1}(u), \dot{Z}_{n+1}(u), \ddot{Z}_{n+1}(u), \dddot{Z}_{n+1}(u) \rightarrow 0 \text{ as } u \rightarrow \infty. \quad (43b)$$

As before we will use Fourier cosine transform to solve Equation 42. Let

$$g(k) = \int_0^{\infty} \ddot{X}(u) \cos ku \, du \quad (44a)$$

$$\text{where } X(u) = Z_{n+1}(u). \quad (44b)$$

By using the boundary conditions given in Equations 43a and 43b and upon integrating by parts, we get the following relationships:

$$\int_0^{\infty} \ddot{X}(u) \cos ku \, du = -k^2 g(k) \quad (45a)$$

$$\int_0^{\infty} u \dot{X}(u) \cos ku \, du = \frac{g'(k)}{k} - \frac{g(k)}{k^2} \quad (45b)$$

and

$$\int_0^{\infty} X(u) \cos ku \, du = -\frac{g(k)}{k^2} \quad (45c)$$

Upon substituting Equations 45a, 45b, and 45c into Equation 42, and rearranging terms, we obtain the following differential equation for the function  $g(k)$

$$g'(k) + g(k) \left( -\frac{n+1}{k} + rk^3 \right) = \frac{(-1)^n}{n!} r e^{-k^4} k^{3n+2} \quad (46)$$

Multiplying both sides of the equation by the integrating factor,  $\exp(k^4)k^{n+1}$ , we obtain the exact differential equation

$$\frac{d}{dk} [\exp(k^4) k^{n+1} g(k)] = 4 \frac{(-1)^n}{n!} k^{4n+3} \quad (47)$$

By integrating the above equation  $g(k)$  can be obtained as

$$g(k) = \frac{(-1)^n}{(n+1)!} \exp(-k^4) k^{3(n+1)} \quad (48)$$

Substituting the above expression for  $g(k)$  in Equation 45c and taking the Fourier inverse transform we have

$$Z_{n+1}(u) = \frac{2}{\pi} \int_0^{\infty} \frac{(-1)^{n+1}}{(n+1)!} k^{3(n+1)} \exp(-k^4) \cos ku \, dk. \quad (49)$$

Substituting the values of the functions  $Z_0(u)$  and  $Z_n(u)$  in Equation 26a, we obtain the profile of a grain boundary groove under the combined action of the surface and volume diffusion mechanisms. This result is

$$y = m(Bt)^{1/4} \frac{2}{\pi} \int_0^{\infty} \frac{1}{k^2} [\exp(-k^4 - pk^3) - 1] \cos ku \, dk. \quad (50)$$

Substituting the values of  $u$  and  $p$  we obtain for the grain boundary groove profile the expression

$$y = m \frac{2}{\pi} \int_0^{\infty} \frac{1}{\omega^2} [\exp(-B\omega^4 t - A'\omega^3 t) - 1] \cos \omega x \, d\omega. \quad (51)$$

### Numerical calculations

For the purpose of numerical computations we express the results as

$$y = m(Bt)^{1/4} Z^{sv} \quad (52a)$$

where

$$Z^{sv} = u + \frac{1}{2\pi} \sum_{\ell=0}^{\infty} \frac{(-1)^{\ell} u^{2\ell}}{(2\ell)!} \sum_{n=0}^{\infty} \frac{(-1)^n p^n}{(n)!} \Gamma\left(\frac{3n+2\ell-1}{4}\right). \quad (52b)$$

The above result is obtained from the evaluation of the integral in Equations 39 and 40. The double series in Equation 52b can be shown to be convergent for all finite values of  $p$  and  $u$ , as follows:

Let the above double series be rewritten as

$$Z^{sv} = u + \frac{1}{2\pi} \sum_{\ell=0}^{\infty} a_{\ell} \sum_{n=0,1}^{\infty} b_{n\ell} + \frac{1}{2\pi} \sum_{\ell=0}^{\infty} a_{\ell} \sum_{n=2}^{\infty} b_{n\ell} \quad (53a)$$

where

$$a_{\ell} = \frac{(-1)^{\ell} u^{2\ell}}{(2\ell)!} \quad (53b)$$

and

$$b_{n\ell} = \frac{(-1)^n p^n}{(n)!} \Gamma\left(\frac{3n+2\ell-1}{4}\right) \quad (53c)$$

It has been shown (49) that the double series

$$\sum a_n \sum b'_{n\ell} \quad (54a)$$

is convergent where

$$b'_{n\ell} = \frac{(-1)^n p^n}{n!} \Gamma\left(\frac{3n+2\ell+3}{4}\right). \quad (54b)$$

Since

$$\frac{b_{n\ell}}{b'_{n\ell}} = \frac{4}{3n+2\ell-1} < 1,$$

the double infinite series in Equation 53a must be convergent. Hence it can be used to obtain the profile of a grain boundary groove when volume diffusion is present, except when it is the sole mechanism. However, as  $p$  gets larger and larger one has to consider very large number of terms in numerically evaluating the series. In order to overcome this difficulty we may represent the result in an alternative manner as follows: One can assume an equation to the grain boundary groove profile of the form

$$y = m(A't)^{1/3} \sum_{n=0}^{\infty} q^n X_n(v) \quad (55a)$$

where



$$v = \frac{x}{(A't)^{1/3}} \quad (55b)$$

$$q = \left(\frac{1}{p}\right)^{4/3} \quad (55c)$$

and proceed as was done before from Equation 26a. The result is

$$y = m(A't)^{1/3} z^{vs} \quad (56a)$$

where

$$z^{vs} = v + \frac{1}{2\pi} \sum_{\ell=0}^{\infty} \frac{(-1)^{\ell} v^{2\ell}}{(2\ell)!} \sum_{n=0}^{\infty} \frac{(-1)^n q^n}{(n)!} \Gamma\left(\frac{4n+2\ell-1}{3}\right) \quad (56b)$$

The above result represents the case of a grain boundary groove where volume diffusion is the dominant mechanism.

#### Discussion

The results of the preceding analysis will not be discussed in three parts. First, we shall discuss the growth kinetics of the grain boundary groove as predicted by the present theory. Next, an extension of the theory will be given which incorporates the contribution of the evaporation-condensation mechanism to the development of the groove profile. Finally, a new procedure for analyzing experimental data on grain boundary grooving

will be presented which will yield simultaneously the surface diffusion as well as the volume diffusion coefficient values.

#### Predictions of the present theory

Grain boundary groove profiles, developed under the concomitant action of surface diffusion and volume diffusion mechanisms, are numerically calculated from Equation 28b. These calculations are carried out in two parts. First the value of the series with variable  $n$  is obtained for various values of  $\ell$  by using double precision in the computer calculations, and next, the summation over  $\ell$  is carried out, again using double precision for calculations. The results for the groove profile are given in Table 5 and are shown graphically in Figure 22 for different values of the parameter  $p$ . The curvatures of these profiles are also numerically calculated using Equation 52b, and the results are plotted in Figure 23. The height,  $h$ , and the depth,  $d$ , of the profiles are also calculated by knowing the profile shape at the origin and at half widths. The characteristic ratios of a grain boundary groove namely  $\frac{h}{d}$  and  $\frac{W}{d}$  are plotted as functions of  $p$  (Figures 24 and 25) and are tabulated in Table 5.

A variation of  $W/W_s$  as a function of  $p$  is shown in Figure 26. The parameter,  $p$ , is related to the parameter  $\alpha$ , given by Mullins and Shewmon (28) by the relationship

$$p = 0.5287896 \alpha W_s \approx 0.53 \alpha W_s.$$

Using this relationship, the result of the Mullins-Shewmon (M-S) theory is also shown on the same figure for comparison.

Table 5. Characteristic ratios of a grain boundary groove

p	$W/(Bt)^{1/4}$	$h/(Bt)^{1/4}$	$d/(Bt)^{1/4}$	W/d	h/d
0.0	4.600	0.1940	0.9741	23.71	0.1991
0.2	4.890	0.1953	1.0292	25.04	0.1898
0.4	5.161	0.1976	1.0805	26.12	0.1829
0.6	5.414	0.2005	1.1285	27.00	0.1777
0.8	5.650	0.2037	1.1736	27.74	0.1736
1.0	5.874	0.2072	1.2163	28.35	0.1704
1.2	6.085	0.2108	1.2566	28.87	0.1667
1.4	6.285	0.2145	1.2950	29.30	0.1656
1.6	6.475	0.2182	1.3492	29.68	0.1631

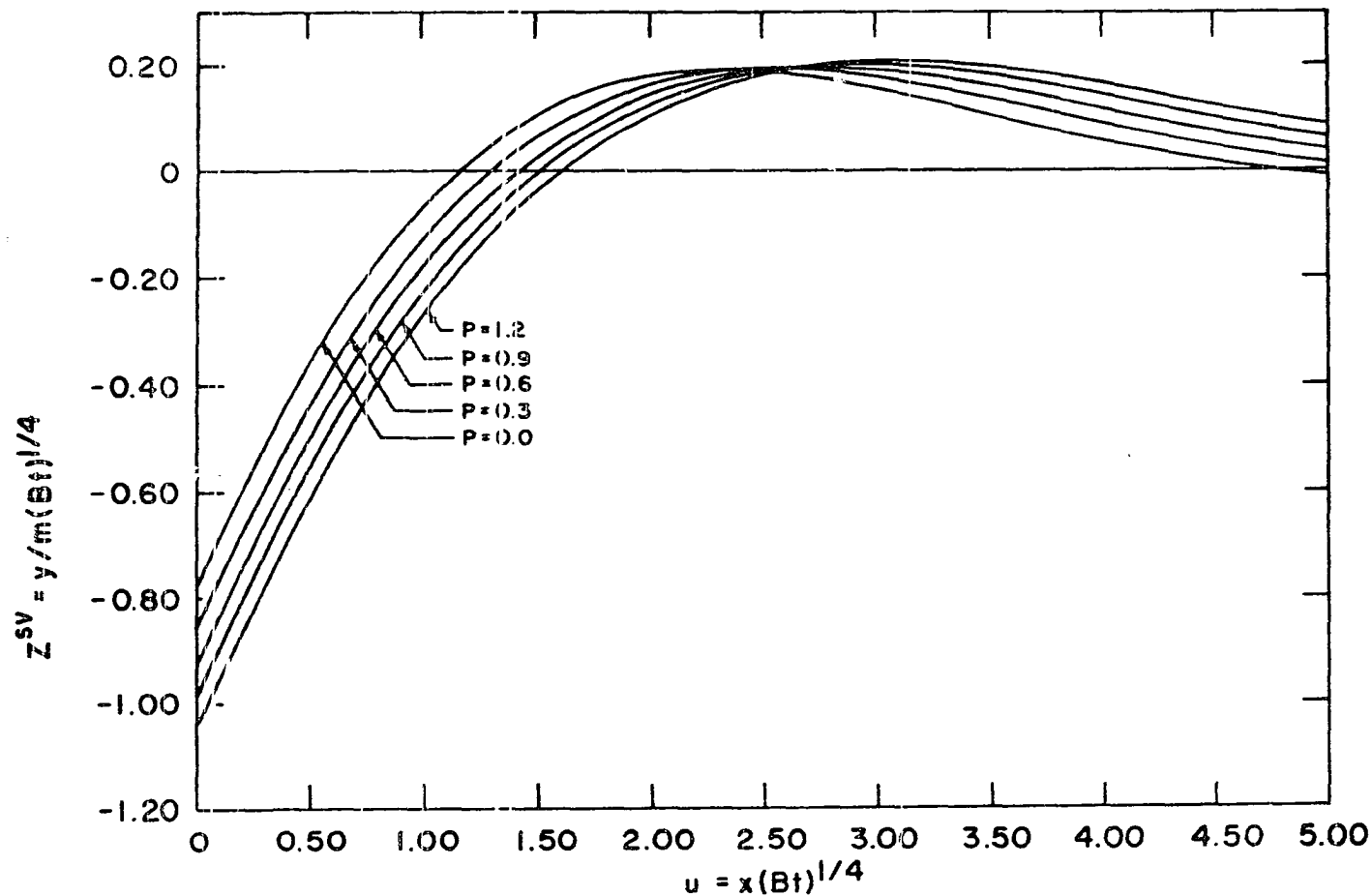


Figure 22. Normalized profile shape.  $p = 0.0$  corresponds to the case of pure surface diffusion. The remaining curves indicate the change in the profile shape due to the increasing presence of volume diffusion contribution

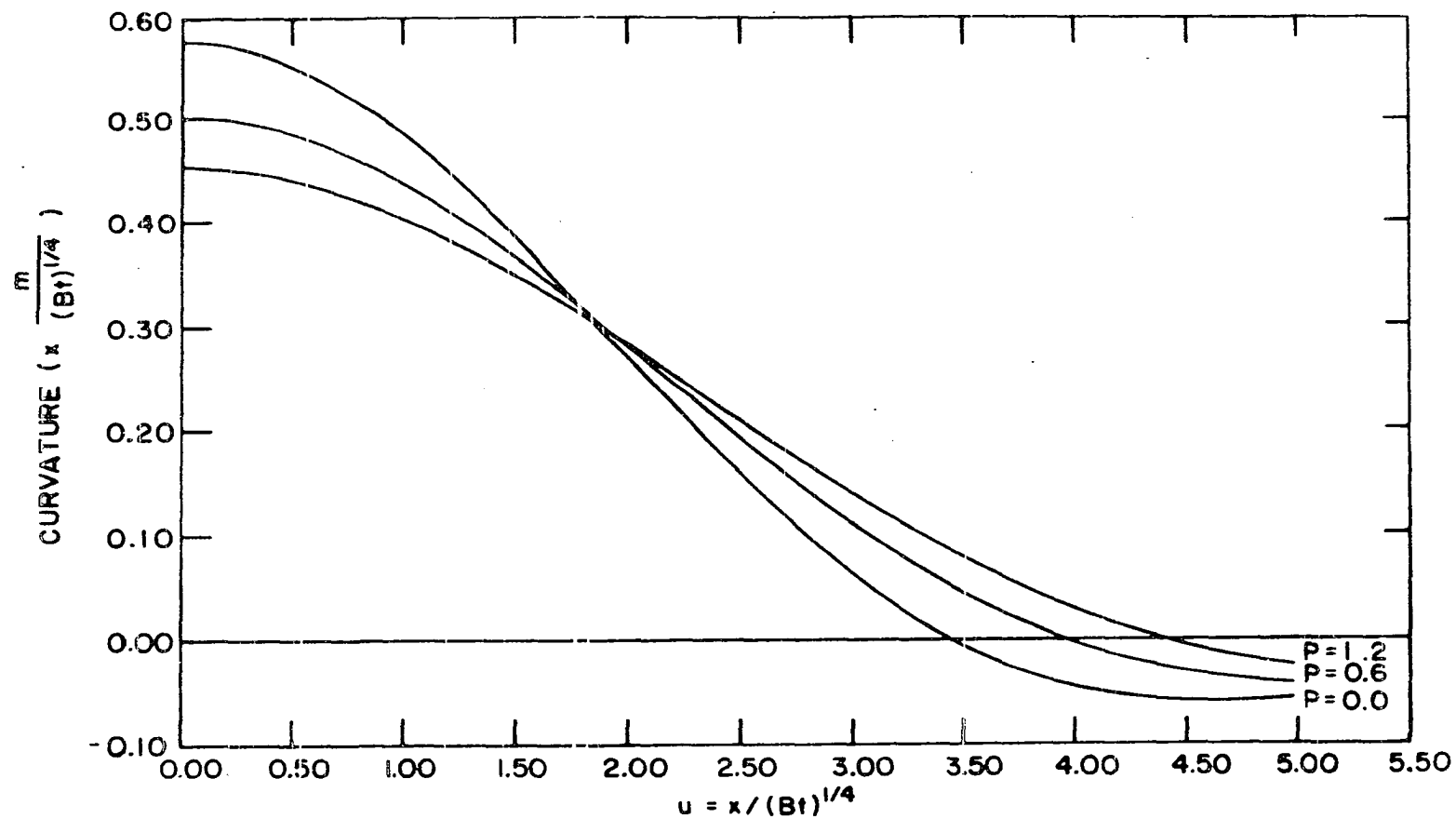


Figure 23. The curvature of the normalized profile for the case of pure surface self-diffusion ( $p = 0.0$ ) and for the case of the combined action of both the diffusion mechanisms

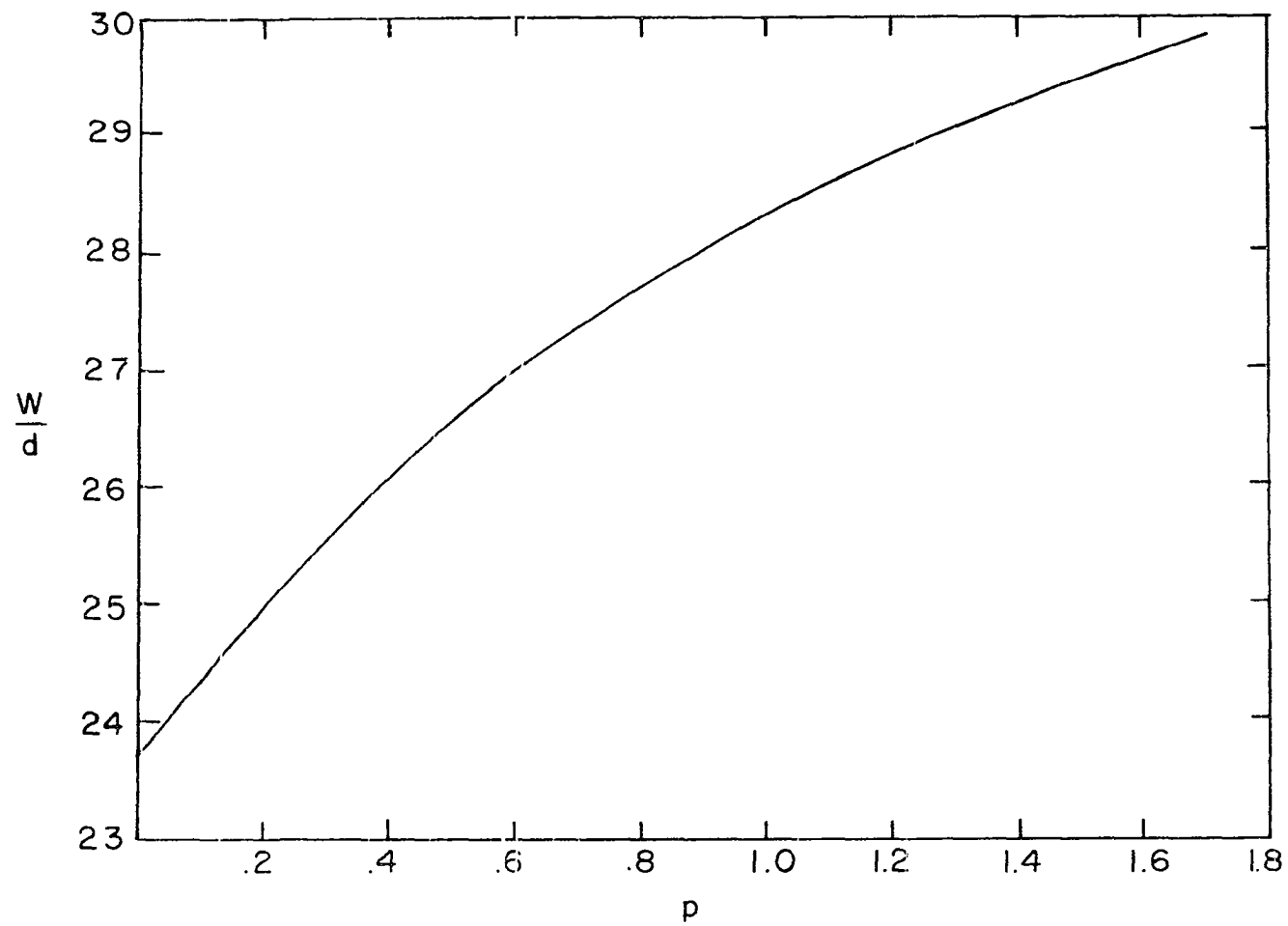


Figure 24. Variation of  $W/d$  as a function of  $p$

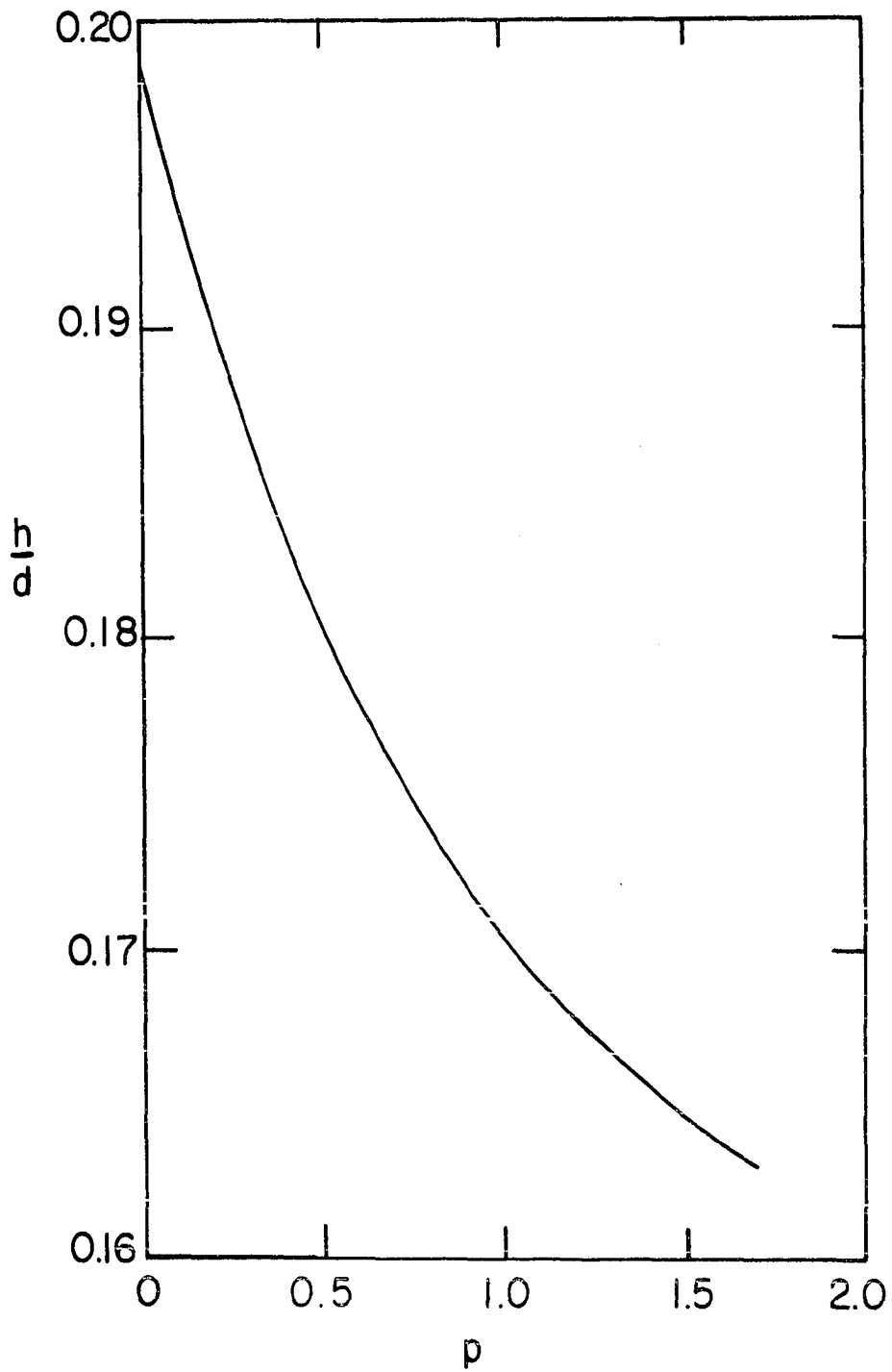


Figure 25. Variation of  $h/d$  with the parameter  $p$

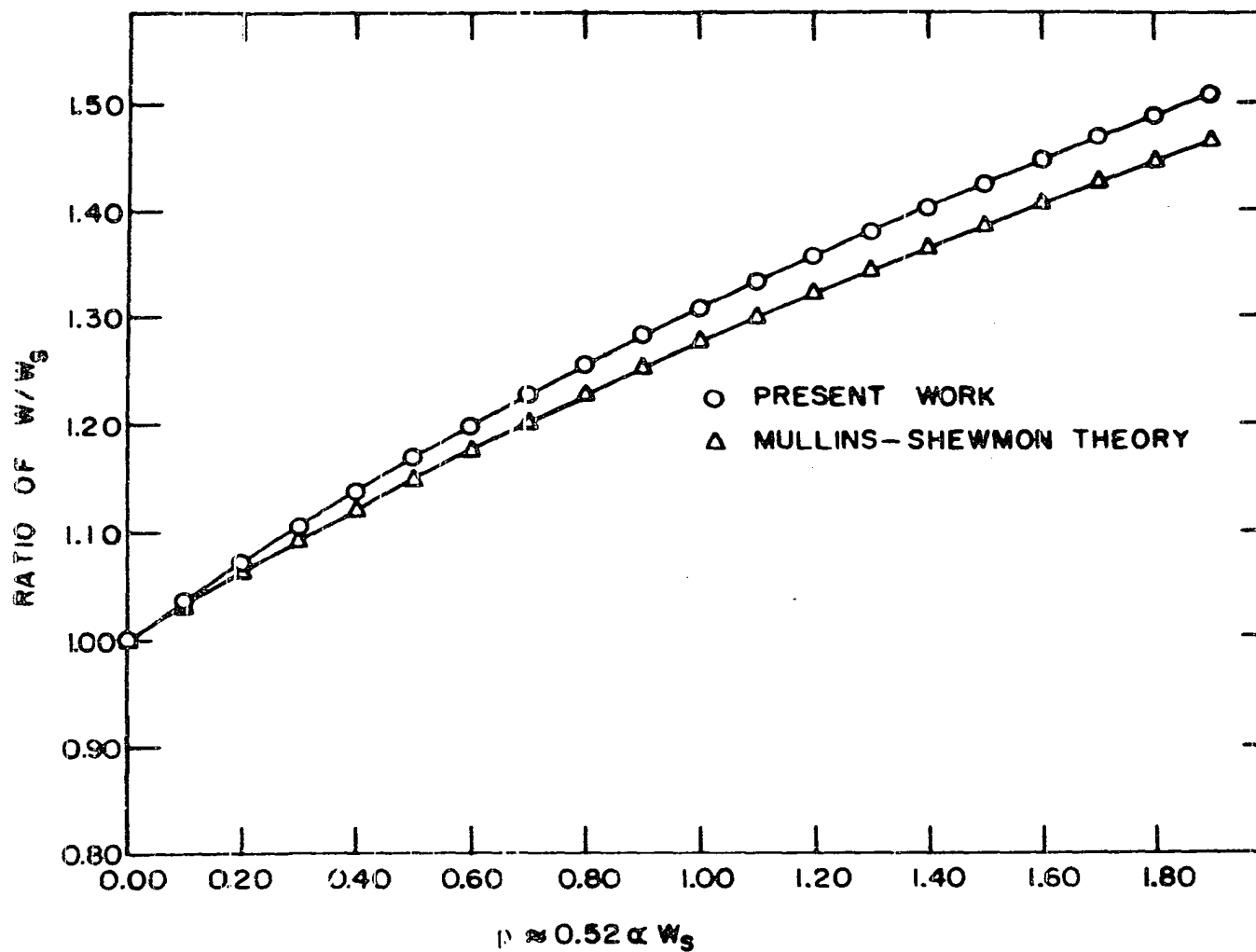


Figure 26. Variation of  $W/W_s$  with the parameter  $p$



We would now like to relate the magnitude of the parameter  $p$  with the relative importance of the two transport mechanisms. Following M-S, we can calculate the volume of material transported (per unit groove length) to form the groove, and divide it by  $W^2$  to obtain the geometrical factor  $g$ . This geometrical factor should vary from 3.582  $m$  for pure surface diffusion mechanism,  $p = 0$ , to 3.780  $m$  when only volume diffusion mechanism,  $p = \infty$ , is present. When both transport mechanisms are present, the value of  $g$  is obtained from the numerical solution of the equation

$$g = \frac{2m}{W^2} \int_0^{u_0} z^{sv} du. \quad (57)$$

The variation of the geometrical factor  $g/m$  with the parameter  $p$  is given in Table 4, and these results are also plotted in Figure 27. Note that the variation of  $g/m$  with  $p$  is appreciable near  $p = 0$ , which implies that the volume diffusion contribution to the transport of atoms is important even at low  $p$  values. On the other hand, the volume diffusion mechanism primarily determines the groove profile when  $p \geq 2$  or  $t \geq 16A'^4/B^3$ .

#### Extension of the present analysis

The growth of a grain boundary groove under the simultaneous actions of the surface diffusion and volume diffusion mechanisms has been theoretically analyzed. However, near the melting point, the evaporation-condensation mechanism may also contribute appreciably to the matter transport. This added contribution can be readily incorporated into the theory if we note that the grain boundary groove profile, given by

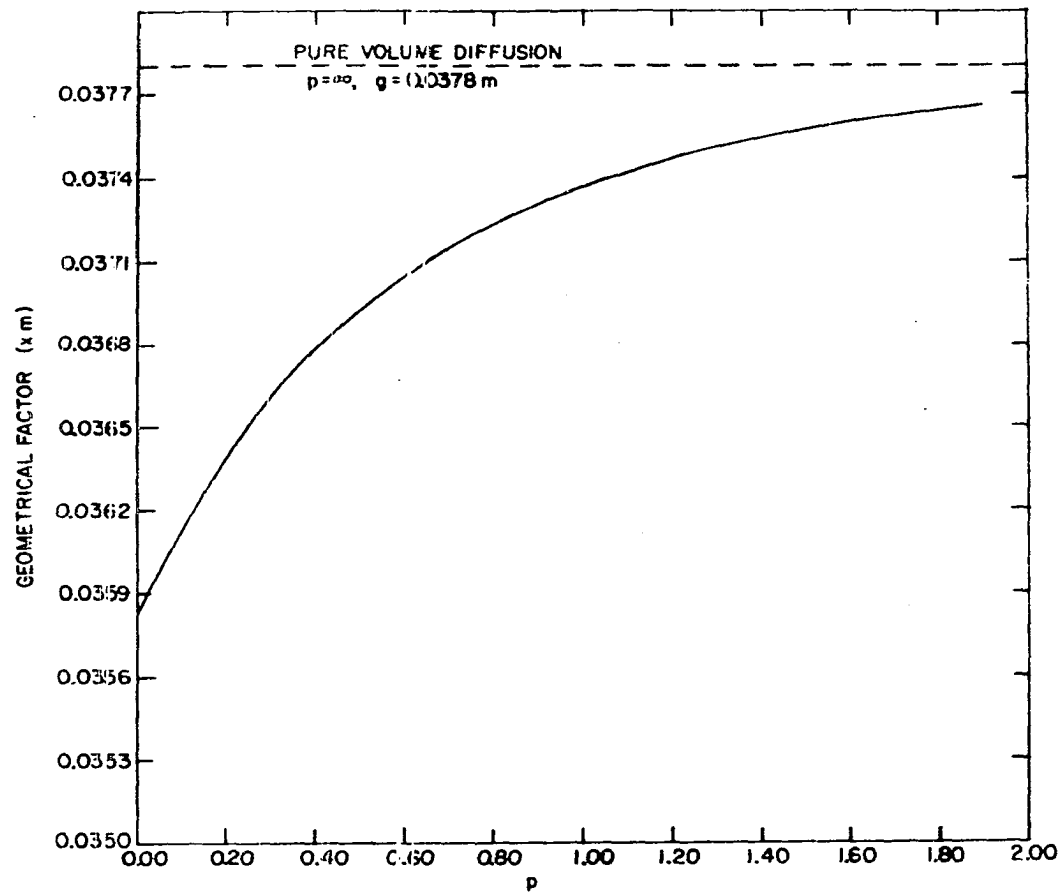


Figure 27. Relationship between the geometrical factor,  $g$ , and the parameter  $p$

Equation 51, is quite analogous to that for the decay of a scratch on a plane surface (50). Thus, when the evaporation-condensation mechanism is also operative along with the surface diffusion and volume diffusion mechanisms, the groove profile can be shown to take the shape

$$y = \frac{2}{\pi} \int_0^{\infty} \frac{1}{\omega^2} (\exp[-(B\omega^4 t + A'\omega^3 t + A\omega^2 t)] - 1) \cos \omega x \, d\omega \quad (58)$$

where the parameter A, which takes into account the matter transport by the evaporation-condensation mechanism, is defined by Equation 9.

#### Analysis of experimental data

In order to obtain the values of corrected widths from the experimental widths, M-S theory requires that the volume diffusion and surface diffusion coefficients be known. Gjostein (7) suggested an iterative procedure which was followed by the other investigators to determine the surface diffusion coefficient of atoms by using the grain boundary grooving technique. Such an analysis, however, requires a large number of iterations when an appreciable volume diffusion contribution is present (29,30). It also requires a prior knowledge of the volume diffusion coefficient near the surface which may be either unknown or significantly different from that in the bulk (46). We shall now show that the use of the present theoretical analysis requires neither the detailed iteration procedure nor the knowledge of the volume diffusion coefficient. In fact, from the experimental data on grain boundary grooving, one can simultaneously determine the surface diffusion coefficient and the volume diffusion coefficient values.

Experimental data on grain boundary grooving primarily measures the width of the groove as a function of time. We shall therefore obtain a theoretical expression for the width of the groove as a function of the parameter  $p$ . Detailed calculations of the width are carried out for values of  $p$  ranging from 0 to 2.0 at intervals of 0.1. The numerical results are then represented by the following sixth order polynomial

$$\frac{W}{(Bt)^{1/4}} = \sum_{n=0}^6 C_n p^n, \quad (59)$$

where the coefficients  $C_n$  are listed in Table 6. The polynomial representation of  $W$  matches with the numerical results up to five decimal places which is the accuracy of the tabulated results. Upon substituting the value of  $p$  in Equation 59, we obtain the following expression for the groove width

$$W = \sum_{n=0}^6 C_n [B^{1/4}] [A'B^{-3/4}]^n t^{(n+1)/4}. \quad (60)$$

The above result can be rewritten as

$$W(a,b,t) = \sum_{n=0}^6 C_n a b^n t^{(n+1)/4} \quad (61)$$

where

$$a = B^{1/4} \text{ and } b = A'B^{-3/4}.$$

Equation 61 relates the width of the groove with time by means of two unknown constants,  $a$  and  $b$ , whose values can be determined by matching the theory with experimental results. From a set of  $N$  experimental observations

Table 6. Values of coefficients

---

$c_0$	4.59983
$c_1$	1.50660
$c_2$	$-2.81287 \times 10^{-1}$
$c_3$	$5.57051 \times 10^{-2}$
$c_4$	$-6.66786 \times 10^{-3}$
$c_5$	$-1.63577 \times 10^{-4}$
$c_6$	$1.26520 \times 10^{-4}$

---

on the width versus time,  $(\bar{w}_1, t_1)$ , one can determine the values of the constants,  $a$  and  $b$ , by minimizing the mean square deviation (m.s.d.) (51) which is

$$\text{m.s.d.} = \frac{1}{N} \sum_1 [W_1 - W(a, b, t_1)]^2 . \quad (62)$$

A knowledge of the values of  $a$  and  $b$  now enables one to calculate  $A'$  and  $B$ , and thus,  $D_s$  and  $D_v$  if the value of surface energy ( $\gamma$ ) is known. If  $\gamma$  is unknown, one can still obtain the ratio of  $D_s/D_v$  and even calculate one of the diffusion coefficients if the value of the other is known.

For grain boundary grooves on copper (100) surfaces in a hydrogen atmosphere, Gjostein (7) and M-S (28) have measured the width of the groove as a function of annealing time. Analysis of these data is carried out using Equation 62, and the results are shown in Figure 28. From the values of  $A'$  and  $B$ , the surface diffusion and volume diffusion coefficients have been calculated as a function of temperature by assuming the surface energy value to be  $1670 \text{ ergs/cm}^2$  (7). These results are given in Table 7 and also plotted in Figures 29 and 30.

The volume diffusion coefficients, shown in Figure 29, show a linear relationship with  $1/T$  over the entire range of temperatures studied. This result can be represented by the expression

$$D_v = 2.1 \times 10^{-1} \exp\left[-\frac{46,500}{RT}\right] .$$

The volume diffusion results near the surface are found to be the same as in the bulk.

The surface diffusion coefficient results, shown in Figure 30, show

Table 7. Surface and volume diffusion coefficients of copper

Temperature °C	$D_s$ , cm <sup>2</sup> /sec		$D_v$ , cm <sup>2</sup> /sec	
	Present Analysis	Previous Analysis	Present Analysis	Bulk Diffusion data <sup>b</sup>
1070	$1.9 \times 10^{-4}$	$1.7 \times 10^{-4}$	$8.3 \times 10^{-9}$	$4.3 \times 10^{-9}$
1035 <sup>a</sup>	$8.0 \times 10^{-5}$	$6.1 \times 10^{-5}$	$2.2 \times 10^{-9}$	$2.6 \times 10^{-9}$
1020	$3.2 \times 10^{-5}$	$4.5 \times 10^{-5}$	$3.9 \times 10^{-9}$	$2.2 \times 10^{-8}$
950	$0.96 \times 10^{-5}$	$1.7 \times 10^{-5}$	$1.7 \times 10^{-9}$	$7.5 \times 10^{-10}$
930 <sup>a</sup>	$2.4 \times 10^{-5}$	$2.5 \times 10^{-5}$	$3.0 \times 10^{-10}$	$5.5 \times 10^{-10}$
875	$4.5 \times 10^{-6}$	$6.0 \times 10^{-6}$	$4.1 \times 10^{-10}$	$2.1 \times 10^{-10}$
825	$3.3 \times 10^{-6}$	$4.2 \times 10^{-6}$	$1.2 \times 10^{-10}$	$0.83 \times 10^{-10}$
780	$1.2 \times 10^{-6}$	$1.8 \times 10^{-6}$	$5.1 \times 10^{-11}$	$3.3 \times 10^{-11}$

<sup>a</sup>These data are by Mullins and Shewmon (28). The rest of the data are by Gjostein (7).

<sup>b</sup>From reference (47).

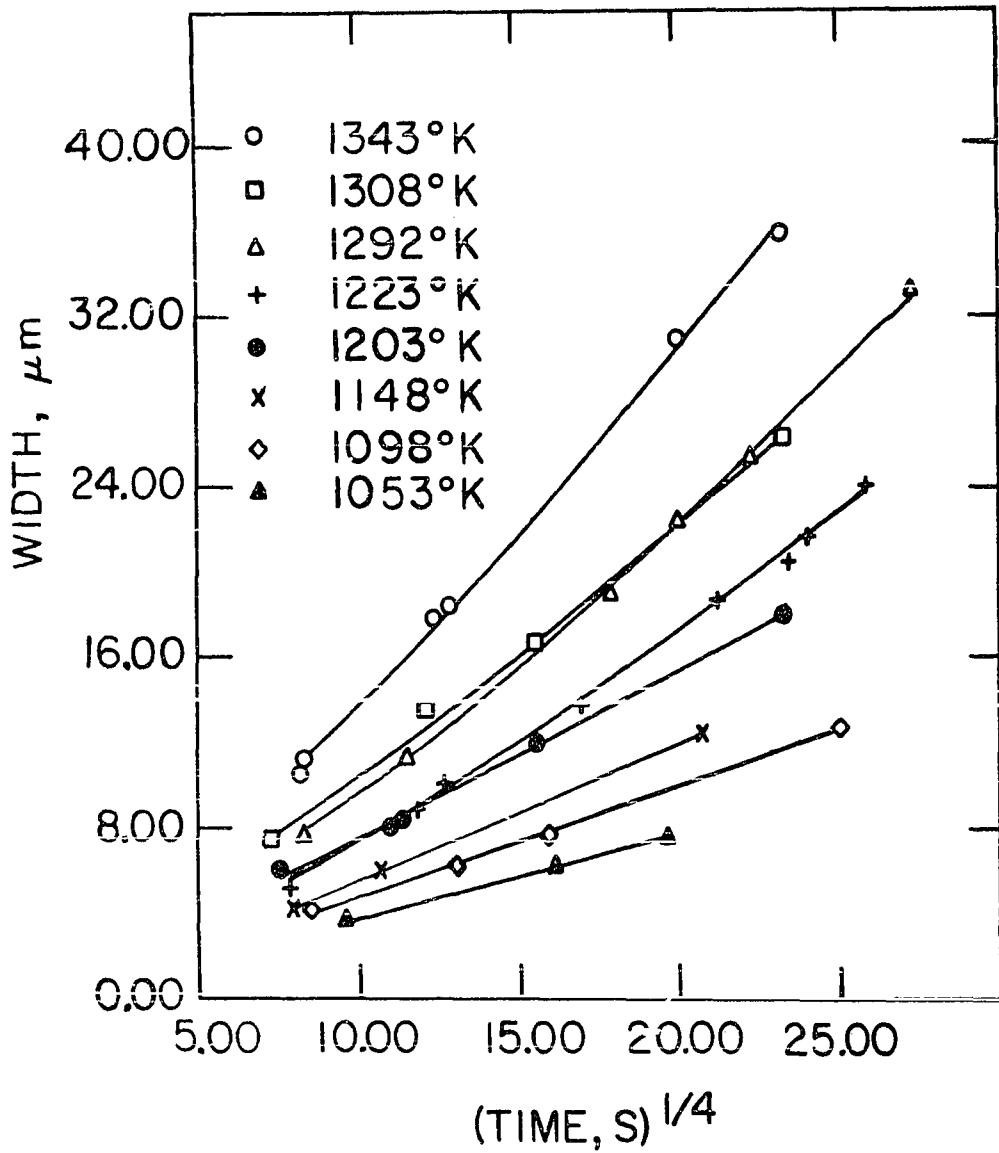


Figure 28. Comparison of the experimental data with the theoretically calculated (solid lines) widths for various temperatures. The data for 1308°K and 1203°K are by Mullins and Shewmon (28) and the rest of the data are by Gjostein (7)



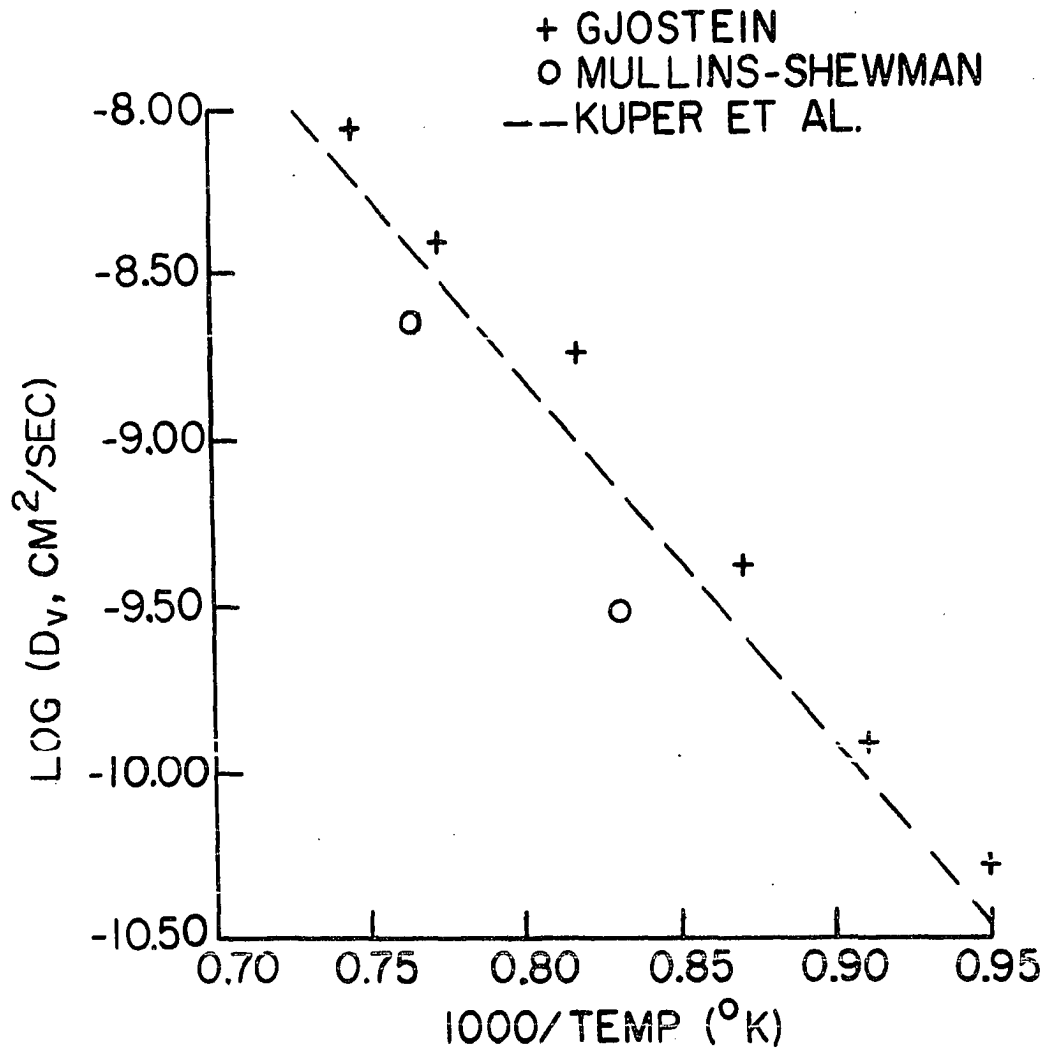


Figure 29. Plot of the temperature dependence of the volume self-diffusion coefficient of copper near the surface. Dotted line shows the bulk diffusion results of Kuper et al. (30)

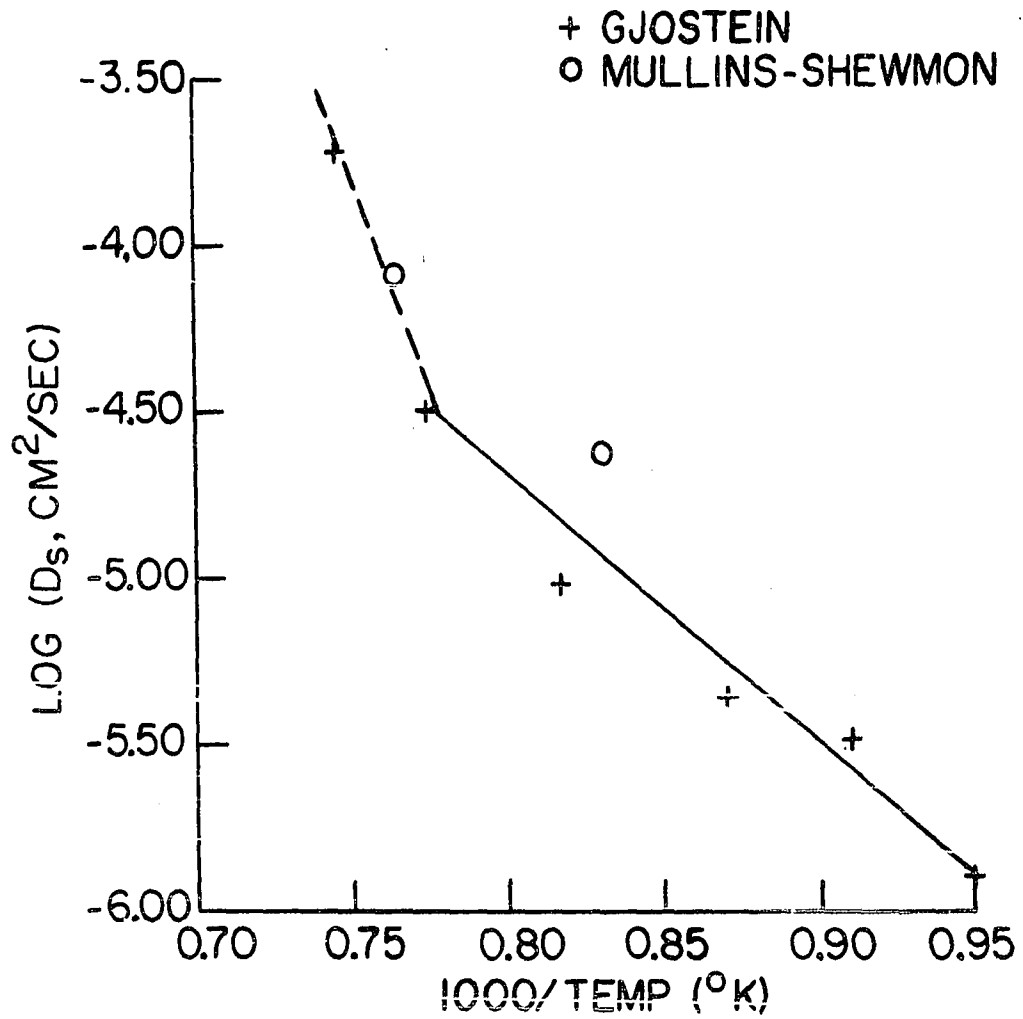


Figure 30. Temperature dependence of surface self-diffusion coefficient for copper (100) surface

a distinct departure from linearity at high temperatures. This observation is consistent with the recent work by Bonzel and Gjostein (48) on a copper (110) surface. In fact, the break in the linear relationship occurs at about 1000°C, which is nearly the same temperature at which Bonzel and Gjostein (48) observed the break. The high temperature data are very few to carry out any meaningful analysis. However, the low temperature data show

$$D_s = 0,43 \times 10^2 \exp\left[-\frac{35,100}{RT}\right] .$$

The  $D_0$  and  $Q$  values are quite close to the values obtained by Bonzel and Gjostein (48), as shown in Table 8.

In order to assess the importance of volume diffusion mechanism on the development of groove profiles, the value of  $p$  as a function of annealing time is plotted in Figure 31. At small times  $p$  is small, but it increases to a value of about 0.25. Figure 27 shows that as  $p$  goes from zero to 0.25, the amount of material transported by the volume diffusion mechanism varies from zero to about forty percent. The volume diffusion contribution to the development of groove profile is therefore quite significant for a copper (100) surface, although surface diffusion is still the major means of matter transport.

Table 8. Values of  $D$  and  $Q$  for the near (100) surface diffusion coefficient<sup>9</sup> of Cu<sup>a</sup>

Reference	$D_0$ (cm <sup>2</sup> /sec)	$Q$ (kcal/mole)
Present work	$0.43 \times 10^2$	36.1
Bonzel & Gjostein (48)	$1.6 \times 10^2$	38.2
Gjostein (7)	$6.50 \times 10^2$	41.0
Collins & Shewmon (30)	$4.2 \times 10^3$	46.0
Choi & Shewmon (29)	$1.4 \times 10^4$	52.2

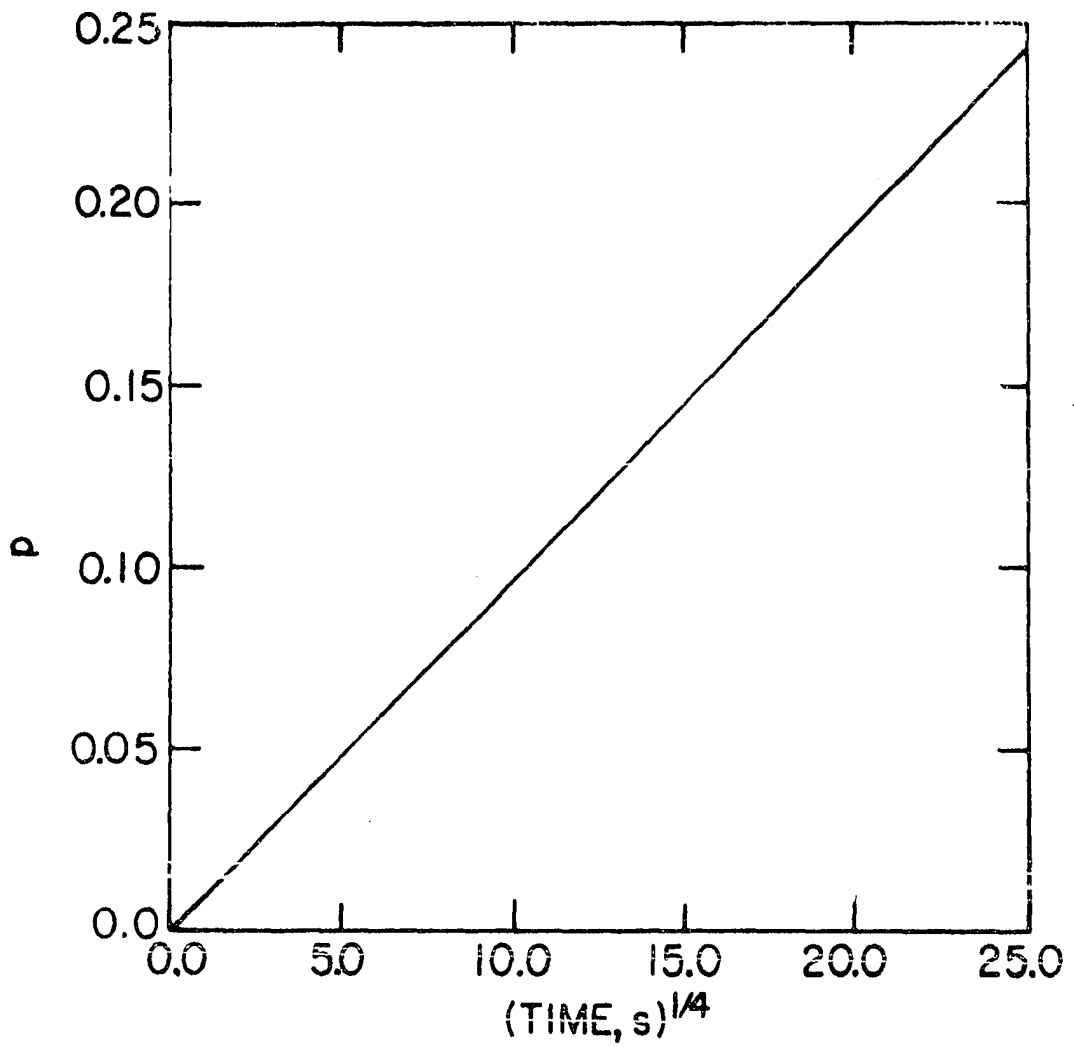


Figure 31. The change in parameter  $p$  with time to show how the relative importance of surface and volume diffusion mechanisms changes with time

## CONCLUSIONS

(1) LEED studies of oxygen adsorption on V have been carried out and similarities have been noted between oxygen adsorption on V(100) surface and surfaces of other B.C.C. metals.

(2) A rigorous theory has been developed for the growth of a grain boundary groove under the concomitant action of surface and volume diffusion mechanisms. The groove profiles, as well as the curvatures of these profiles, have been predicted in terms of a dimensionless parameter,  $p$ , which measures the relative importance of the two transport mechanisms. It is shown that the surface diffusion mechanism predominates at small times, although the volume diffusion contribution to the transport of matter is not insignificant. On the other hand, when  $t \geq 16A^4/B^3$  the groove profile is completely determined by the volume diffusion mechanism.

(3) An expression is obtained for the groove profile developed under the simultaneous presence of surface diffusion, volume diffusion and evaporation-condensation mechanisms.

(4) A method is outlined to match the present theory with the experimental data on the grain boundary groove widths. It is shown that, from such a comparison, one can independently calculate the surface diffusion as well as the volume diffusion coefficients.

(5) The above method of analyzing groove widths is demonstrated by using the experimental data of Gjostein (7) and Mullins and Shewmon (28) on the copper (100) surface.

## REFERENCES

1. G. A. Somarjai and H. H. Farrel, Adv. in Chem. Phys., 20, 215 (1971).
2. K. K. Vijai and P. F. Packman, J. of Chem. Phys., 50, 1343 (1969).
3. K. Hayek and H. E. Farnsworth, Surface Science, 10, (1968).
4. P. V. McAllister and I. B. Cutler, Metall. Trans., 1, 313 (1970).
5. P. V. McAllister and I. B. Cutler, Adv. in Chem. Phys., 21, 669 (1971).
6. N. A. Gjostein, Metall. Trans., 1, 315 (1970).
7. N. A. Gjostein, Trans. Am. Inst. Min. Engrs., 221, 1039 (1961).
8. E. A. Wood, J. Appl. Phys., 35, 1306 (1964).
9. L. H. Germer, R. M. Stern and A. U. MacRae in "Metal Surfaces," American Society for Metals, Metals Park, Ohio, 1962. Chapter 9.
10. D. G. Alexander and O. N. Carlson, Metallurgical Transactions, 2, 2805 (1971).
11. "Handbook of Lattice Spacings and Structures of Metals," Volume 2, W. B. Pearson, Ed., Pergamon Press, New York, 1967.
12. T. W. Haas, A. G. Jackson and M. P. Hooker, J. of Chem. Phys., 46, 3025 (1967).
13. L. Fiermanns and J. Vennik, Surface Science, 9, 187 (1968).
14. H. K. A. Kann and S. Feuerstein, J. of Chem. Phys., 50, 3618 (1969).
15. J. E. Boggio and H. E. Farnsworth, Surface Science, 3, 62 (1964).
16. J. W. May and L. H. Germer, Surface Science, 7, 430 (1967), and Surface Science, 11, 443 (1968).
17. J. C. Tracy and J. M. Blakely, Surface Science, 15, 257, (1969).
18. G. Ehrlich, J. Phys. Chem., 59, 473 (1955).
19. L. H. Germer and J. M. May, Surface Science, 4, 452 (1966).
20. Yu. G. Ptushinskiĭ and B. A. Chuikov, Soviet Phys.-Solid State, 10, 565 (1968).

21. W. P. Ellis and B. D. Campbell, Trans. Am. Cryst. Assoc., 4, 97 (1968).
22. R. L. Park and H. H. Madden, Jr., Surface Science, 11, 188 (1968).
23. R. W. Powers and M. V. Doyle, J. Appl. Phys. 30, 541 (1959).
24. P. G. Shewmon, J. Appl. Phys., 34, 755 (1963).
25. W. W. Mullins, J. Appl. Phys., 28, 333 (1957).
26. W. W. Mullins, Trans. Am. Inst. Min. Engrs., 218, 354 (1960).
27. W. W. Mullins in "Metal Surfaces - Structure, Energetics and Kinetics," Ed. ASM (1962).
28. W. W. Mullins and P. G. Shewmon, Acta Met., 7, 163 (1959).
29. J. Choi and P. G. Shewmon, Trans. Am. Inst. Min. Engrs., 224, 589 (1962).
30. H. E. Collins and P. G. Shewmon, Trans. Am. Inst. Min. Engrs. 236, 1354 (1966).
31. W. M. Robertson, Trans. Am. Inst. Min. Engrs., 233 1, 1232 (1965).
32. B. C. Allen, Met. Trans. 236, 915 (1966).
33. L. Ho-Yi, Jernkont. Ann., 151, 801 (1967).
34. B. C. Allen, Met. Trans., 245, 2089 (1969).
35. B. C. Allen, Met. Trans., 3, 2544 (1972).
36. J. Henrion, Thesis, Univ. of Paris (1972).
37. N. A. Gjostein, "Adsorption et Croissance Crystalline," Coll. Int. CNRS, Nancy, 1965.
38. J. Perdereau and G. E. Rhead, Surface Science, 7, 175 (1967).
39. R. R. Hough, Script Met., 4, 559 (1970).
40. R. Zahn, Thesis, Jernkontorets Laboratory for Power Metallurgy, Stockholm (1964).
41. C. Herring in "The Physics of Powder Metallurgy," W. E. Kingston, Ed. McGraw Hill (1951).



42. M. McLean and B. Gale, Phil. Mag., 10, 1033 (1969).
43. G. L. J. Bailey and H. C. Watkins, Proc. Phys. Soc., B63, 350 (1950).
44. W. M. Robertson, J. Appl. Phys., 42, 463 (1971).
45. W. P. Ellis and N. H. Nachtrieb, J. Appl. Phys., 40, 472 (1969).
46. D. L. Styris and C. T. Tomizuka, J. Appl. Phys., 34, 1001 (1963).
47. A. Kuper, H. Letaw, Jr., L. Slifkin, E. Sonder and C. T. Tomoznka, Phys. Rev., 96, 1224 (1954).
48. H. P. Bonzel and N. A. Gjostein in "Molecular Processes on Solid Surfaces," E. Dranglis et al., Eds., McGraw-Hill, New York, (1969).
49. E. Gruber, Ph.D. thesis, Carnegie-Mellon University, 1965.
50. W. W. Mullins, J. Appl. Phys., 30, 77 (1959).
51. Subroutine FMFP, System/360 Scientific Subroutine Package, IBM Corporation (1968). H. P. Bonzel and N. A. Gjostein in "Molecular Processes on Solid Surfaces," E. Drauglis et al., Ed., McGraw-Hill, New York, (1969).

## ACKNOWLEDGMENTS

The author wishes to thank Professor R. K. Trivedi for his assistance and guidance in conducting this research and the preparation of this manuscript. He also wishes to extend his gratitude to Professors R. S. Hansen, H. J. Weiss, F. X. Kayser and J. W. Patterson for many valuable discussions during the course of the thesis research.

## APPENDIX

Evaluation of the Integral  $\frac{2}{\pi} \int_0^{\infty} \frac{1}{k^2} [\exp(-k^4) - 1] \cos ku \, dk$

The integral

$$I = \frac{2}{\pi} \int_0^{\infty} \frac{1}{k^2} [\exp(-k^4) - 1] \cos ku \, dk \quad (\text{A.1})$$

can be written in three parts as follows.

$$I = I_1 + I_2 + I_3 \quad (\text{A.2a})$$

where

$$I_1 = \frac{2}{\pi} \int_0^{\infty} \frac{1}{k^2} e^{-k^4} (\cos ku - 1) \, dk \quad (\text{A.2b})$$

$$I_2 = -\frac{2}{\pi} \int_0^{\infty} \frac{1}{k^2} (\cos ku - 1) \, dk \quad (\text{A.2c})$$

$$I_3 = \frac{2}{\pi} \int_0^{\infty} \frac{1}{k^2} (e^{-k^4} - 1) \, dk \quad (\text{A.2d})$$

### Evaluation of integral $I_1$

Using the McLaurin's series expansion for the cosine function,  $I_1$  can be written as

$$I_1 = \frac{2}{\pi} \int_0^{\infty} \frac{1}{k^2} e^{-k^4} \sum_{n=1}^{\infty} \frac{(-1)^n k^{2n} u^{2n}}{(2n)!} \, dk \quad (\text{A.3})$$

Interchanging the order of integration and summation

$$I_1 = \frac{2}{\pi} \sum_{n=1}^{\infty} \frac{(-1)^n u^{2n}}{(2n)!} \int_0^{\infty} k^{2n-2} e^{-k^4} \, dk \quad (\text{A.4})$$

The remaining integral can be evaluated as shown in the evaluation of  $I_3$ .  
the result is

$$I_1 = \sum_{n=1}^{\infty} a_{2n} u^{2n} \quad (\text{A.5})$$

where  $a_n$ 's are the coefficients given by Mullins.

#### Evaluation of integral $A_2$

Using the method of integration by parts with  $dv = \frac{1}{k^2}$ , the integral can be written as

$$I_2 = \frac{2}{\pi} \frac{(\cos ku - 1)}{k} \Big|_0^{\infty} + \frac{2}{\pi} u \int_0^{\infty} \frac{\sin ku}{k} dk \quad (\text{A.6})$$

The first part of the above integral is zero and the second part is the well-known result equal to  $\pm \frac{\pi}{2}$  for  $u > 0$  or  $u < 0$ . Thus,

$$I_2 = \pm u \text{ for } u > 0 \quad (\text{A.7a})$$

$$= -u \text{ for } u < 0 \quad (\text{A.7b})$$

#### Evaluation of integral $A_3$

Once again integrating by parts as before

$$I_3 = -\frac{\pi}{2} (e^{-k^4} - 1) \frac{1}{k} \Big|_0^{\infty} - \frac{2}{\pi} \int_0^{\infty} \frac{rk^3 e^{-k^4}}{k} dk \quad (\text{A.8})$$

The first part is zero and the second part can be transformed to gamma function by substituting  $k^4 = x_0$ .  $I_3$  is therefore obtained as,

$$I_3 = \frac{2}{\pi} \Gamma\left(\frac{3}{4}\right).$$

Substituting the values of  $I_1$ ,  $I_2$ ,  $I_3$  in Equation A.2a, one can obtain

$$I = \sum_{n=0}^{\infty} a_n u^n$$

where  $a_n$  are the coefficients given by Mullins (25). This result proves the equivalence of the integral representation of  $Z_0(u)$  as obtained in the present work and the series form obtained by Mullins.